J. Mech. Phys. Solids 206 (2026) 106368

Contents lists available at ScienceDirect

Journal of the Mechanics and Physics of Solids

journal homepage: www.elsevier.com/locate/jmps

A fully coupled THMC-MPM framework for modeling phase transition and large deformation in methane hydrate-bearing sediment

Jidu Yu [a], Jidong Zhao [a,*], Kenichi Soga [b], Shiwei Zhao [a], Weijian Liang [c]

[a] Department of Civil and Environmental Engineering, Hong Kong University of Science and Technology, Kowloon, Hong Kong, China
[b] Department of Civil and Environmental Engineering, University of California, Berkeley, USA
[c] College of Civil and Transportation Engineering, Shenzhen University, Shen Zhen, China

ARTICLE INFO

Keywords:
Material point method
Methane hydrate-bearing sediment
THMC coupling
Large deformation
Hydrate dissociation
Submarine landslides

ABSTRACT

Methane hydrate-bearing sediment (MHBS) is a multiphase granular system characterized by complex thermo-hydro-mechanical–chemical (THMC) interactions involving phase transitions and large deformation behavior. Hydrate dissociation weakens sediment strength, potentially initiating geohazards such as submarine landslides. Simultaneously, large deformations in MHBS alter the sediment's state, influencing hydrate reaction kinetics. Despite recent progress, modeling the coupled processes of hydrate dissociation and large deformation in MHBS remains a significant challenge. This study develops a THMC-coupled material point method (MPM) framework to simulate the pre- to post-failure behavior of MHBS associated with hydrate dissociation. The framework incorporates three key advancements: (i) a six-field governing equation integrated with the Kim–Bishnoi hydrate reaction model to resolve dynamic phase transitions, multiphase interactions, and large deformations; (ii) a strain-softening Mohr–Coulomb model with hydrate saturation-dependent strength to capture sediment mechanical degradation; and (iii) a hybrid explicit–implicit time integration scheme designed to enhance computational efficiency for systems with low permeability and high reaction rates. The framework is validated against Masuda's hydrate dissociation experiment and an extended Terzaghi consolidation benchmark, before being applied to simulate biaxial compression tests and hydrate dissociation-triggered slope failures. We reveal that (1) shear dilation generates negative excess pore pressure in undrained conditions, triggering hydrate dissociation within the shear bands ; (2) shear heating resulting from rapid, large deformation promotes hydrate dissociation, exacerbating sediment softening; and (3) sediment strength degradation, hydrothermal variations, slope geometry, and other factors collectively shape the dynamic progression of retrogressive failures in MHBS. This work provides a powerful framework for modeling hydrate-related granular mechanics and geohazards.

1. Introduction

Methane hydrate, an ice-like crystalline compound abundant in marine continental margin sediments and permafrost regions (Archer, 2007; Reagan and Moridis, 2007; Demirbas, 2010; Ruppel and Kessler, 2017), has drawn significant scientific and

* Corresponding author.
E-mail addresses: jyubu@connect.ust.hk (J. Yu), jzhao@ust.hk (J. Zhao), soga@berkeley.edu (K. Soga), ceswzhao@ust.hk (S. Zhao), wliangab@connect.ust.hk (W. Liang).

https://doi.org/10.1016/j.jmps.2025.106368
Received 26 June 2025; Received in revised form 27 August 2025; Accepted 13 September 2025
Available online 19 September 2025

industrial interest due to its dual role as a potential energy resource and a driver of geohazards (Makogon, 2010; Boswell and Collett, 2011; Chong et al., 2016; Yin and Linga, 2019; Yu and Zhao, 2021). Its destabilization, triggered by shifts in temperature-pressure equilibrium from natural processes (*e.g.*, sea-level fluctuations, sedimentation, ocean warming) or human activities (*e.g.*, drilling, gas exploitation) (Gatter et al., 2021; Jyothsna and Satyavani, 2024), poses two interrelated risks. Firstly, hydrate dissociation releases methane, a potent greenhouse gas, into the atmosphere, exacerbating climate feedback loops (Cardoso and Cartwright, 2016; Mestdagh et al., 2017; Ketzer et al., 2020; Yu and Zhao, 2021; Davies et al., 2024). Secondly, the loss of hydrate cementation weakens sediment strength, creating zones of instability (Waite et al., 2009; Wu et al., 2020; Wang et al., 2021; Jiang et al., 2014). These weakened layers, coupled with excess pore pressures from impeded fluid flow in low-permeability sediments, can promote shear band formation parallel to the seafloor (Xu and Germanovich, 2006; Puzrin et al., 2004). Such mechanical degradation and pressure buildup act synergistically to trigger large-scale submarine landslides, jeopardizing offshore infrastructure and escalating environmental risks.

The behavior of methane hydrate-bearing sediments (MHBS) is governed by a complex interplay of coupled thermo-hydro-mechanical–chemical (THMC) processes. The rate at which hydrate dissociates is dictated by reservoir temperature and the sediment's capacity to supply the heat required for the endothermic dissociation of methane hydrate (Li et al., 2019). Absolute and relative permeabilities, governing the mobility of pore gas and water, directly influence methane transport efficiency (Xu and Germanovich, 2006; Zhao et al., 2016; Chen et al., 2018). Sediment properties further regulate dissociation-driven processes, including fine particle migration during rapid fluid flow, permeable pathway obstruction, and reservoir zone stability (Waite et al., 2009; Hyodo et al., 2013; Klar et al., 2010). Compared to natural hydrate dissociation, gas exploitation activities pose a heightened risk of submarine landslides due to amplified dissociation rates and frequent geological disturbances. However, gaps in understanding THMC coupling mechanisms hinder accurate predictions of MHBS behavior and associated risks under both natural and industrial conditions (Sultan et al., 2004; Zhang et al., 2021; Jyothsna and Satyavani, 2024). Consequently, developing advanced numerical models to simulate hydrate dissociation and THMC responses remains critical for risk assessment and mitigation.

Early numerical efforts pioneered the modeling of thermo-hydro-chemical (THC) processes during methane hydrate dissociation, represented by Eulerian approaches such as finite difference (FDM) and finite volume (FVM) methods. A foundational study by Masuda (1999) developed a two-phase FDM simulator that integrated the Kim–Bishnoi kinetic dissociation model (Kim et al., 1987) and Corey's permeability model (Corey, 1954). This framework was later extended by Nazridoust and Ahmadi (2007) into an axisymmetric three-phase FVM model and by Sun and Mohanty (2006) into a multi-component FVM approach. Subsequent work refined governing equations and numerical discretization schemes and examined key factors influencing THC dynamics in MHBS, including initial hydrate saturation, outlet pressure, ambient temperature, and permeability heterogeneity (Liang et al., 2010; Ju et al., 2020; Konno et al., 2010; Klar et al., 2013). Although Eulerian methods excel in fluid flow simulation, they struggle to capture history-dependent granular sediment behaviors, such as strain localization. In contrast, Lagrangian mesh-based finite element method (FEM) dominates geomechanical modeling due to its capacity to resolve stress–strain relationships effectively.

Current strategies for modeling fully coupled THMC processes in MHBS fall into two categories: (1) *sequential or iterative coupling* of Eulerian fluid solvers (FDM/FVM) with Lagrangian solid solvers (FEM), which, however, introduces inaccuracies during inter-solver data transfer (Kimoto et al., 2007; Lei et al., 2015; Sridhara et al., 2018; Queiruga et al., 2019); (2) *fully coupled THMC-FEM solvers*, which unify phase transition, fluid flow, heat transfer, and geomechanics within a single framework (Sun et al., 2018; Ye et al., 2022; Wu et al., 2025). Despite these advances, FEM remains susceptible to mesh distortion under large deformations, hindering its capacity to simulate post-failure dynamics. To date, few studies have achieved robust simulation of hydrate dissociation-related large deformation and failures. Thus, a critical need remains to develop advanced numerical frameworks capable of seamlessly bridging pre- and post-failure behavior during hydrate dissociation.

In recent decades, the computational mechanics community has witnessed substantial progress in particle-based methods inherently suited to large-deformation modeling. Among these, the material point method (MPM) (Sulsky et al., 1994, 1995) has emerged as a prominent hybrid Eulerian–Lagrangian technique. MPM tracks material states and motion via Lagrangian particles while solving governing equations on a fixed background mesh. This dual framework combines the advantages of Eulerian and Lagrangian methods while circumventing their limitations, enabling MPM to gain widespread adoption in fields such as computer graphics (Stomakhin et al., 2013, 2014; Hu et al., 2018), granualr mechanics (Soga et al., 2016; Chen et al., 2021; Dunatunga and Kamrin, 2017; Baumgarten et al., 2024), fluid dynamics (Mast et al., 2015; Chandra et al., 2024), and geohazard analysis (Li et al., 2021; Gaume et al., 2018; Siron et al., 2023). Recent extensions of MPM address coupled multiphysics problems, including hydro-mechanical (HM) (Yerro et al., 2015; Bandara and Soga, 2015; Zhao et al., 2020; Liang et al., 2023) and thermo-hydro-mechanical (THM) coupling (Pinyol et al., 2018; Lei et al., 2021; Yu et al., 2024c), with applications spanning rainfall-induced landslides (Lei et al., 2020, 2021), permafrost thaw (Sun et al., 2022; Yu et al., 2024e), pile installation (Ceccato et al., 2016; Galavi et al., 2017), thermally driven slope instability (Pinyol et al., 2018; Lei et al., 2024), and seismic liquefaction (Feng et al., 2021).

Existing MPM implementations exhibit considerable diversity in formulations, time integration schemes, material point discretization, and stabilization techniques. For saturated porous media under HM coupling, the three-field $\boldsymbol{v}_s - \boldsymbol{v}_w - p$ formulation ($\boldsymbol{v}_s$: solid velocity; $\boldsymbol{v}_w$: water velocity; p: pore pressure) is widely favored for its ability to resolve dynamic, high-frequency responses in large deformations. Yerro et al. (2015) generalized this framework to unsaturated soils by introducing a five-field $\boldsymbol{v}_s - \boldsymbol{v}_w - \boldsymbol{v}_g - p_w - p_g$ formulation ($\boldsymbol{v}_g$: gas velocity; p_w: pore water pressure; p_g: pore gas pressure), although thermal effects and phase transitions were excluded. Current THM-coupled MPM studies predominantly focus on saturated systems (Pinyol et al., 2018; Yu et al., 2024c) or

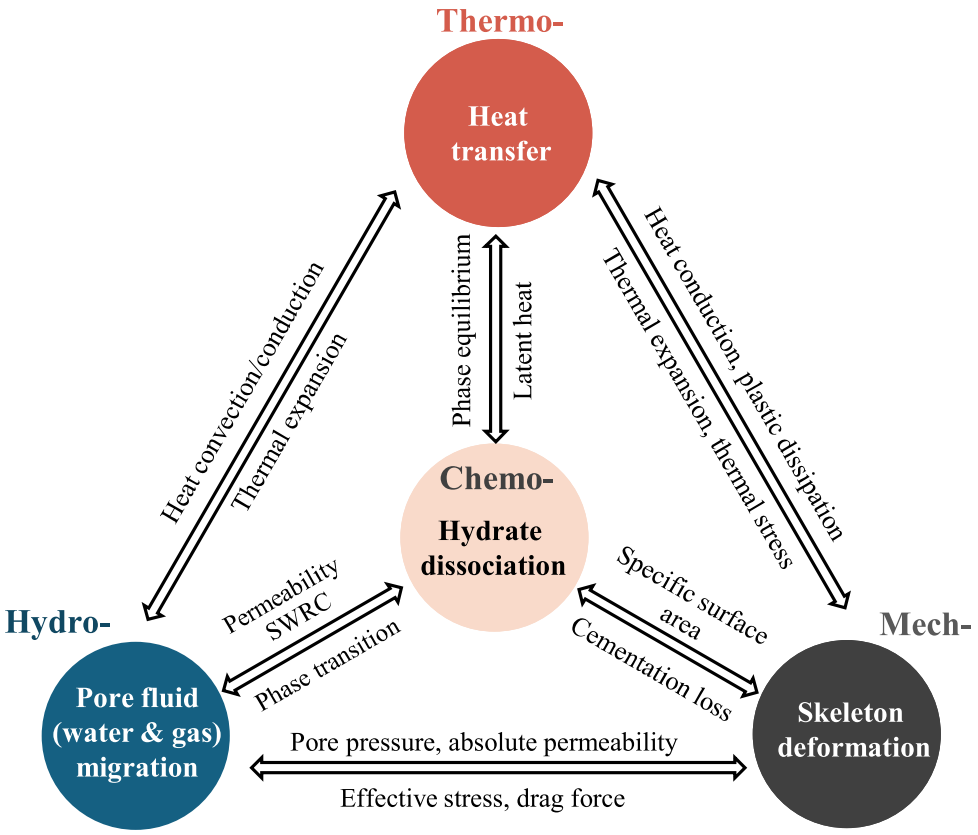

Fig. 1. Illustration of coupled THMC processes in MHBS.

employ simplified unsaturated formulations that neglect gas velocity ($\boldsymbol{v}_g$) and gas pressure (p_g) (Lei et al., 2021; Zhan et al., 2024). Recent advances incorporate ice–water phase transitions in porous media, demonstrating progress in modeling complex granular materials (Sun et al., 2022; Zheng et al., 2023; Yu et al., 2024b,d). Nevertheless, a comprehensive MPM framework capable of simulating the full THMC coupling processes in MHBS remains absent.

In this study, we aim to develop a coupled THMC-MPM framework for MHBS, with a specific focus on modeling hydrate dissociation-related large deformations. The objectives are fourfold: (1) to formulate a rigorous mathematical model that captures the coupled THMC processes in MHBS, as illustrated in Fig. 1; (2) to develop a computationally efficient and accurate MPM algorithm for solving the formulations; (3) to validate the framework rigorously against classical geotechnical benchmarks; and (4) to investigate the bidirectional coupling effects of hydrate dissociation and large sediment deformation in practical applications using the developed framework.

The mathematical model will incorporate the following key components: (a) a six-field governing equation ($\boldsymbol{v}_s$–$\boldsymbol{v}_w$–$\boldsymbol{v}_g$–p_w–p_g–T) to comprehensively describe THMC processes in MHBS, enabling simulations of dynamic, large-deformation behaviors that extend beyond the quasi-static assumptions typically used in existing FEM studies; (b) a hydrate kinetic reaction model to accurately represent hydrate dissociation and formation processes; and (c) a detailed consideration of variations in hydraulic, thermal, and mechanical properties arising from phase transitions and skeleton deformation. To address the numerical challenges inherent to coupled MPM modeling, a hybrid explicit–implicit time integration scheme is developed to achieve a balance between computational efficiency, simplicity, and accuracy. This work will not only advance the state-of-the-art in the modeling of hydrate-related granular mechanics but also provide a new framework for assessing geohazards in hydrate-rich environments.

The structure of this paper is organized as follows. Section 2 presents the mathematical model for MHBS, including the governing conservation laws and the constitutive models employed to describe the coupled THMC processes. Section 3 details the numerical implementation of the proposed formulations within the MPM framework. In Section 4, the framework is rigorously validated against two classical benchmarks. Section 5 applies the framework to two large-deformation problems: biaxial compression tests and hydrate dissociation-triggered submarine landslides. Finally, Section 6 gives some concluding remarks and outlooks.

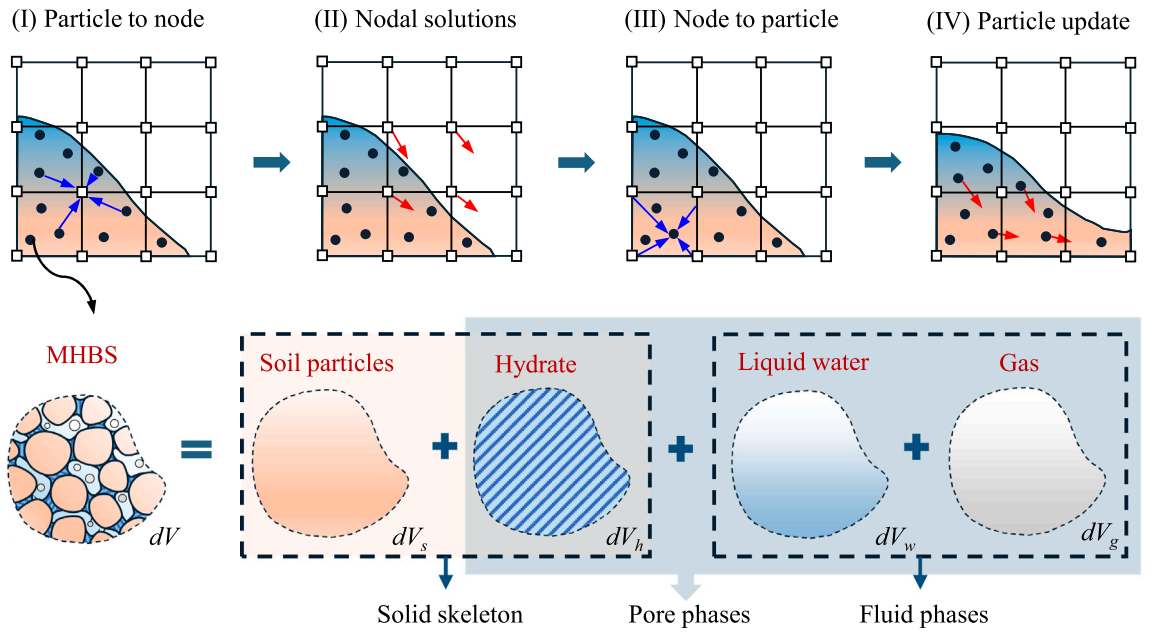

Fig. 2. Schematic illustration of single-point multiphase MPM for MHBS.

2. Governing equations for MHBS

2.1. Preliminaries and prerequisites

2.1.1. Basic assumptions

MHBS are typically multiphase, multicomponent porous media consisting of solid grains, methane hydrate, liquid water, methane gas, vapor, and chemical solutes. For simplicity, while maintaining generality, we consider MHBS as porous media composed of four primary phases or components: solid grain (s), hydrate (h), water (w), and gas (g). The current model does not account for fluidized sand, dissolved gas, vapor, and chemical inhibitors. The dissociation of methane hydrate is governed by reaction kinetics that depend on the thermodynamic state of the MHBS system, described by the following reaction,

$$CH_4 \cdot N_h H_2O \xrightarrow{T>T_e,\ p<p_e} CH_4 + N_h H_2O, \tag{1}$$

where N_h represents the hydration number. Although natural gas hydrates may include multiple guest gases, methane hydrate is the predominant component in most geological settings. Therefore, this study focuses exclusively on the methane hydrate reaction. It is worth noting that the hydration number N_h plays a critical role in representing the chemical composition and phase behavior of methane hydrate, which directly impacts the accuracy of the mass exchange and phase transition modeling. In our study, we assumed a hydration number $N_h = 6$, which is a commonly used value in methane hydrate research (Liang et al., 2010; Ruan et al., 2012; Sun et al., 2018; Hardwick and Mathias, 2018; White et al., 2020; Ye et al., 2022). This assumption is based on the structure I-type methane hydrate, where typically 6 water molecules per methane molecule are required to form the clathrate structure (Sloan and Koh, 2007; Ke et al., 2019).

2.1.2. Degree of saturation and effective saturation

The mathematical model is developed based on mixture theory within the single-point multi-phase MPM framework, where all phases in the MHBS medium are represented at a single Lagrangian material point, as illustrated in Fig. 2. For an MHBS system assumed to be isotropic, homogeneous, and uniformly distributed, the pore space is shared among the hydrate, liquid water, and gas phases. The porosity ϕ is defined as (Lewis and Schrefler, 1998),

$$\phi := \frac{V_h + V_w + V_g}{V}, \tag{2}$$

where V_h, V_w, and V_g are the volumes of the hydrate, water, and gas phases, respectively, in a representative volume element (RVE), and V is the total volume of the RVE.

The degree of saturation for each pore phase in MHBS is defined as (Sun et al., 2018; Ye et al., 2022),

$$S_\pi := \frac{V_\pi}{V_h + V_w + V_g}, \quad \pi = h, w, g. \tag{3}$$

The summation of S_π for all phases must satisfy the following constraint: $S_h + S_w + S_g = 1$.

In hydrate-bearing sediments, gas and water can become trapped within the pore space as "residual gas" and "residual water", with their magnitudes influenced by hydrate saturation. To account for these phenomena, an effective water saturation S_e is defined as (Lewis and Schrefler, 1998; Sun et al., 2018),

$$S_e := \frac{V_w - V_{wr}}{V_w + V_g - V_{wr} - V_{gr}} = \frac{S_w/\left(1 - S_h\right) - S_{wr}}{1 - S_{wr} - S_{gr}}, \tag{4}$$

where S_{wr} and S_{gr} are the residual water saturation and residual gas saturation, respectively, and are defined as,

$$S_{wr} := \frac{V_{wr}}{V_w + V_g}, \quad S_{gr} := \frac{V_{gr}}{V_w + V_g}. \tag{5}$$

Here, V_{wr} and V_{gr} denote the volumes of residual water and residual gas, respectively.

The effective saturation can be determined using the soil–water retention curve (SWRC). In this study, we assume a uniform wettability for the hydrate-bearing sediment, which means that the sediment grains and hydrates share the same wettability characteristics. Several analytical or empirical models have been proposed to describe the SWRC (Brooks, 1965; Van Genuchten, 1980; Fredlund and Xing, 1994). Among them, the Van Genuchten (1980) model is widely used for various methane hydrate simulations (*e.g.*, Waite et al., 2009; Sun et al., 2018; White et al., 2020; Zhang et al., 2024). Following these studies, the VG model is employed in this work, expressed as,

$$S_e = \left[1 + \left(\frac{p_g - p_w}{p_0}\right)^{1/(1-m)}\right]^{-m}, \tag{6}$$

where $p_g - p_w = p_c$ represents the capillary force, p_g and p_w are the pore gas pressure and pore water pressure, respectively, p_0 is the reference pressure, and m is a constant model parameter. In this study, the VG model parameters are assumed to be constant for the sake of simplicity. However, experimental studies have shown that these parameters are influenced by factors such as hydrate saturation and the properties of hydrates (*e.g.*, hydrophilicity or hydrophobicity) (Mahabadi et al., 2016). In future work, more advanced SWRC models will be considered to better capture these dependencies.

Using Eqs. (4) and (6), the partial derivatives of water saturation with respect to pore water or gas pressure can be derived as,

$$\frac{\partial S_w}{\partial p_w} = -\frac{\partial S_w}{\partial p_g} = \frac{\partial S_w}{\partial S_e}\frac{\partial S_e}{\partial p_w}, \tag{7}$$

where $\frac{\partial S_w}{\partial p_w}$ and $\frac{\partial S_w}{\partial p_g}$ are important for deriving the mass balance equations.

2.1.3. Partial densities and equation of state

Based on mixture theory (Lewis and Schrefler, 1998), the partial densities of the solid and pore phases are defined as follows,

$$\rho^s := (1 - \phi)\rho_s, \tag{8a}$$

$$\rho^\pi := \phi S_\pi \rho_\pi, \quad \pi = h, w, g, \tag{8b}$$

where ρ_π is the intrinsic density of phase π. The overall density of the MHBS mixture, ρ_m, is then expressed as,

$$\rho_m = (1 - \phi)\rho_s + \phi S_h \rho_h + \phi S_w \rho_w + \phi S_g \rho_g. \tag{9}$$

To relate the intrinsic density of each phase to its thermodynamic properties, the equation of state (EOS) is employed. The EOS for the solid, hydrate, and water phases is derived using a first-order Taylor expansion, expressed as,

$$\frac{1}{\rho_\pi}\frac{D_\pi \rho_\pi}{Dt} = \alpha_\pi \frac{D_\pi p_\pi}{Dt} - \beta_\pi \frac{D_\pi T}{Dt}, \quad \pi = s, h, w, \tag{10}$$

where α_π is the compressibility, β_π is the thermal expansivity, p_π is the pressure, and T is the temperature. The parameters α_π and β_π may be assumed to be constants or functions of temperature and pressure. In this study, the compressibility of soil grains and methane hydrates is neglected, assuming $\alpha_s = \alpha_h = 0$.

The intrinsic density of the gas phase exhibits a highly nonlinear dependence on temperature and pressure. To describe this behavior, the equation of state (EOS) for an ideal gas is adopted, given by,

$$\rho_g = \frac{M_g p_g}{RT}, \tag{11}$$

where M_g is the molar mass of the gas phase, and R is the universal gas constant.

2.2. Conservation equations

2.2.1. Conservation of momentum

In dynamic analyses of multiphase systems, resolving the momentum equations for individual phases while incorporating inertia effects offers significant advantages over quasi-static assumptions for the entire mixture. In this model, the hydrate phase is assumed

to be rigidly bonded to the solid phase, resulting in identical velocities for the hydrate and solid phases, *i.e.*, $\boldsymbol{v}_h = \boldsymbol{v}_s$. This assumption reduces the system to three independent kinematic variables: solid velocity ($\boldsymbol{v}_s$), water velocity ($\boldsymbol{v}_w$), and gas velocity ($\boldsymbol{v}_g$), governed by three momentum balance equations. Specifically, the system's motion is described by momentum equations for (1) the MHBS mixture, (2) the water phase, and (3) the gas phase.

The momentum balance equation for the MHBS mixture is given by,

$$\left[(1-\phi)\rho_s + \phi S_h \rho_h\right] \frac{D^s \boldsymbol{v}_s}{Dt} + \phi S_w \rho_w \frac{D^s \boldsymbol{v}_w}{Dt} + \phi S_g \rho_g \frac{D^s \boldsymbol{v}_g}{Dt} = \nabla \cdot \boldsymbol{\sigma} + \rho_m \boldsymbol{b}, \tag{12}$$

where $\boldsymbol{\sigma}$ is the total Cauchy stress tensor, $\boldsymbol{b}$ is the body force vector, and ρ_m is the mixture density. Here, the inertia contributions from the solid grains and hydrate are combined into a single term due to their shared velocity.

The flow of the water and gas phases is assumed to be governed by Darcy's law (Ruan et al., 2012; Chen et al., 2016; Ye et al., 2022), with the Darcy fluid flux expressed as,

$$\boldsymbol{J}_\pi = \phi S_\pi \left(\boldsymbol{v}_\pi - \boldsymbol{v}_s\right), \quad \pi = w, g. \tag{13}$$

Accordingly, the momentum balance equations for the water and gas phases are formulated as,

$$\phi S_\pi \rho_\pi \frac{D^s \boldsymbol{v}_\pi}{Dt} = -\phi S_\pi \nabla p_\pi + \phi S_\pi \rho_\pi \boldsymbol{b} - \phi S_\pi \frac{\mu_\pi}{k_a k_{r\pi}} \boldsymbol{J}_\pi, \quad \pi = w, g, \tag{14}$$

where p_w and p_g are the pore water and pore gas pressures, respectively; k_a is the absolute permeability, which depends on porosity and hydrate saturation; $k_{r\pi}$ is the relative permeability, which depends on the saturation of phase π; and μ_π is the viscosity, which is assumed to be constant in this study.

The relationship between the total stress, the effective stress on the solid skeleton, and the pore fluid pressures follows an extended form of Bishop's effective stress theory (Gallipoli et al., 2003; Jommi, 2000; Oka et al., 2006),

$$\boldsymbol{\sigma} = \boldsymbol{\sigma}' - p\boldsymbol{I}, \quad \text{with } p = \chi_w p_w + \chi_g p_g. \tag{15}$$

Here, $\boldsymbol{\sigma}'$ is the effective stress tensor, p is the pore fluid pressure, and χ_w and χ_g are the Bishop coefficients, which are approximated as,

$$\chi_w = \frac{S_w}{S_w + S_g}, \quad \chi_g = \frac{S_g}{S_w + S_g}. \tag{16}$$

It is important to note that the effective stress must account for the influence of the hydrate phase on the solid skeleton, which will be discussed in detail in Section 2.3.3.

2.2.2. Conservation of mass

Considering phase transitions between hydrate, water, and gas, and assuming no additional mass exchange, the mass balance equation for solid grains in a Lagrangian reference frame is expressed as,

$$\frac{D^s\left[(1-\phi)\rho_s\right]}{Dt} + (1-\phi)\rho_s \nabla \cdot \boldsymbol{v}_s = 0. \tag{17}$$

For the remaining phases (hydrate, water, and gas), the mass balance equation is given as,

$$\frac{D^s\left(\phi S_\pi \rho_\pi\right)}{Dt} + \phi S_\pi \rho_\pi \nabla \cdot \boldsymbol{v}_s + \nabla \cdot \phi S_\pi \rho_\pi \left(\boldsymbol{v}_\pi - \boldsymbol{v}_s\right) = \dot{m}_\pi, \ \pi = h, w, g, \tag{18}$$

where $\dot{m}_\pi$ is the rate of mass change per unit volume due to hydrate dissociation. The total mass exchange among the phases is conserved, satisfying the condition: $\dot{m}_h + \dot{m}_w + \dot{m}_g = 0$. The value of $\dot{m}_\pi$ is determined by the kinetic hydrate dissociation rate, which will be detailed in Section 2.3.1.

Using the chain rule and incorporating the equation of state (EOS) for the solid phase, the mass balance for solid grains can be reformulated as,

$$\frac{D^s \phi}{Dt} = -(1-\phi)\beta_s \frac{D^s T}{Dt} + (1-\phi)\nabla \cdot \boldsymbol{v}_s. \tag{19}$$

This equation describes the material derivative of the porosity ϕ.

Considering $\boldsymbol{v}_s = \boldsymbol{v}_h$ and applying the EOS for the hydrate phase, the mass balance for the hydrate phase can be reformulated as,

$$\phi \frac{D^s S_h}{Dt} = \frac{\dot{m}_h}{\rho_h} + \beta_{sh} \frac{D^s T}{Dt} - S_h \nabla \cdot \boldsymbol{v}_s, \tag{20}$$

where $\beta_{sh} = (1-\phi)S_h\beta_s + \phi S_h \beta_h$. This equation describes the material derivative of the hydrate saturation S_h. It is evident that the evolution of S_h is influenced not only by the hydrate reaction dynamics but also by changes in the solid skeleton's volumetric deformation and variations in porosity.

Similarly, the mass balance equations for the water and gas phases can be reformulated in terms of the primary variables, p_w, p_g, and T, as follows:

Water phase:

$$\left(\phi\frac{\partial S_w}{\partial p_w}+\frac{\phi S_w}{K_w}\right)\frac{D^s p_w}{Dt}-\phi\frac{\partial S_w}{\partial p_w}\frac{D^s p_g}{Dt}-\beta_{ws}\frac{D^s T}{Dt}+S_w\nabla\cdot\boldsymbol{v}_s+\nabla\cdot\boldsymbol{J}_w=\frac{\dot{m}_w}{\rho_w}, \tag{21}$$

Gas phase:

$$\left(\frac{\phi S_g}{\rho_g}\frac{M_g}{RT}+\phi\frac{\partial S_w}{\partial p_w}\right)\frac{D^s p_g}{Dt}-\phi\frac{\partial S_w}{\partial p_w}\frac{D^s p_w}{Dt}-\beta_{ghs}\frac{D^s T}{Dt}+\left(S_g+S_h\right)\nabla\cdot\boldsymbol{v}_s+\nabla\cdot\boldsymbol{J}_g=\frac{\dot{m}_g}{\rho_g}+\frac{\dot{m}_h}{\rho_h}, \tag{22}$$

with

$$\beta_{ws}=(1-\phi)S_w\beta_s+\phi S_w\beta_w, \tag{23a}$$

$$\beta_{ghs}=(1-\phi)\left(S_g+S_h\right)\beta_s+\phi S_h\beta_h+\frac{\phi S_g}{\rho_g}\frac{M_g p_g}{RT^2}, \tag{23b}$$

where $K_w=1/\alpha_w$ is the liquid bulk modulus.

Eqs. (21) and (22) can be combined into a single equation representing the mass balance for the multiphase mixture,

$$\frac{\phi S_w}{K_w}\frac{D^s p_w}{Dt}+\frac{\phi S_g}{\rho_g}\frac{M_g}{RT}\frac{D^s p_g}{Dt}-\beta_m\frac{D^s T}{Dt}+\nabla\cdot\boldsymbol{v}_s+\nabla\cdot\boldsymbol{J}_w+\nabla\cdot\boldsymbol{J}_g=\frac{\dot{m}_w}{\rho_w}+\frac{\dot{m}_g}{\rho_g}+\frac{\dot{m}_h}{\rho_h}, \tag{24}$$

with

$$\beta_m=(1-\phi)\beta_s+\phi S_h\beta_h+\phi S_w\beta_w+\frac{\phi S_g}{\rho_g}\frac{M_g p_g}{RT^2}. \tag{25}$$

In this study, capillary pressure, the pressure difference between the water and gas phases, is explicitly considered. However, many existing studies neglect this effect, simplifying the multiphase mass balance equations into a single unified equation where the pore fluid pressure p serves as the only pressure variable, expressed as,

$$\left(\frac{\phi S_w}{K_w}+\frac{\phi S_g}{\rho_g}\frac{M_g}{RT}\right)\frac{D^s p}{Dt}-\beta_m\frac{D^s T}{Dt}+\nabla\cdot\boldsymbol{v}_s+\nabla\cdot\boldsymbol{J}_w+\nabla\cdot\boldsymbol{J}_g=\frac{\dot{m}_w}{\rho_w}+\frac{\dot{m}_g}{\rho_g}+\frac{\dot{m}_h}{\rho_h}. \tag{26}$$

2.2.3. Conservation of energy

For homogeneous mixtures, thermal equilibrium among all phases is assumed at a given spatial location. Under this assumption, the transient energy balance equation for the MHBS mixture is consolidated into a single governing equation as:,

$$C_m\frac{D^s T}{Dt}+(\rho_w c_w\boldsymbol{J}_w+\rho_g c_g\boldsymbol{J}_g)\cdot\nabla T+\nabla\cdot\boldsymbol{J}_e-\theta\boldsymbol{\sigma}':\dot{\boldsymbol{\varepsilon}}^p=q_e, \tag{27}$$

where C_m is the mixture heat capacity, c_π is the specific heat capacity of phase π, and q_e represents the heat source resulting from hydrate reactions.

The term $\theta\boldsymbol{\sigma}':\dot{\boldsymbol{\varepsilon}}^p$ quantifies energy dissipation due to irreversible deformation, where $\dot{\boldsymbol{\varepsilon}}^p$ is the plastic strain rate, $\boldsymbol{\sigma}'$ is the effective stress tensor, and θ is the plastic work-to-heat conversion coefficient. Plastic heat generation serves as a significant heat source in large deformation problems and will be further explored in the numerical examples.

Remark 1. Note that the plastic work-to-heat conversion coefficient θ is not a constant and varies depending on the material type and loading history (Rosakis et al., 2000). Experimental studies indicate that θ ranges from 0.2 to 1.0 for metals (Taylor and Quinney, 1931; Yang et al., 2018). However, for granular media, including MHBS, such experimental data remain lacking. In most existing studies on granular media and MPM simulations that incorporate thermal effects, θ is typically assumed to be 1.0 for simplicity (Pinyol et al., 2018; Alvarado et al., 2019; Veveakis et al., 2007). Nevertheless, in MHBS, not all plastic work may be converted into heat due to significant energy storage associated with particle rearrangement and hydrate bond breakage, suggesting that θ can be considerably lower. In this study, a default value of $\theta=1$ is adopted. However, in the final landslide example (Sections 5.2.2 and 5.2.3), a lower value of $\theta=0.5$ is adopted to demonstrate the pronounced impact of shear heating, even when only a small fraction of plastic work is converted into heat. Future research should focus on developing a more physics-based approach to determine θ.

The heat conduction within the mixture follows Fourier's law, expressed as,

$$\boldsymbol{J}_e=-\kappa_m\nabla T, \tag{28}$$

where κ_m is the effective thermal conductivity of the mixture. The effective thermal properties, C_m and κ_m, computed as weighted averages of the contributions from individual phases,

$$C_m=(1-\phi)\rho_s c_s+\phi S_h\rho_h c_h+\phi S_w\rho_w c_w+\phi S_g\rho_g c_g, \tag{29a}$$

$$\kappa_m=(1-\phi)\kappa_s+\phi S_h\kappa_h+\phi S_w\kappa_w+\phi S_g\kappa_g, \tag{29b}$$

where κ_π is the thermal conductivity of phase π.

The heat source from hydrate reactions is calculated by (Ye et al., 2022),

$$q_e=\Delta H\dot{m}_h=(C_0+C_1T)\dot{m}_h, \tag{30}$$

where ΔH is the enthalpy change, and C_0 and C_1 are empirical coefficients characterizing the latent heat of hydrate dissociation.

2.2.4. Boundary conditions

The problem domain is represented by Ω, with its boundary denoted by $\partial\Omega$. The time domain is defined as $\mathcal{T} = [0, t]$. The Dirichlet and Neumann boundary conditions for the THMC-coupled problem under consideration are specified as follows.

Dirichlet boundary conditions:

$$\boldsymbol{v}_\pi = \hat{\boldsymbol{v}}_\pi \text{ on } \partial\Omega^D_{v\pi} \times \mathcal{T}, \quad \pi = s, w, g, \tag{31a}$$

$$p_\pi = \hat{p}_\pi \text{ on } \partial\Omega^D_{p\pi} \times \mathcal{T}, \quad \pi = w, g, \tag{31b}$$

$$T = \hat{T} \text{ on } \partial\Omega^D_T \times \mathcal{T}. \tag{31c}$$

Neumann boundary conditions:

$$\boldsymbol{\sigma}_\pi \cdot \boldsymbol{n} = \hat{\boldsymbol{t}}_\pi \text{ on } \partial\Omega^N_{t\pi} \times \mathcal{T}, \quad \pi = s, w, g, \tag{32a}$$

$$-\boldsymbol{J}_\pi \cdot \boldsymbol{n} = \hat{q}_\pi \text{ on } \partial\Omega^N_{q\pi} \times \mathcal{T}, \quad \pi = w, g, \tag{32b}$$

$$-\boldsymbol{J}_e \cdot \boldsymbol{n} = \hat{q}_e + \alpha(T_a - T) \text{ on } \partial\Omega^N_T \times \mathcal{T}. \tag{32c}$$

Here, $\boldsymbol{\sigma}_\pi$ represents the partial stress for each phase, $\hat{\boldsymbol{t}}_\pi$, $\hat{q}_\pi$, and $\hat{q}_e$ denote the prescribed traction, fluid flux, and conductive heat flux, respectively. The term $\alpha\left(T_a - T\right)$ represents the convective heat flux, where α is the convective heat transfer coefficient and T_a is the ambient temperature. For the traction boundary, it is often convenient to prescribe the total traction for the mixture, expressed as $\boldsymbol{\sigma} \cdot \boldsymbol{n} = \hat{\boldsymbol{t}}$ on $\partial\Omega^N_t \times \mathcal{T}$.

2.3. Constitutive models

2.3.1. Kinetic hydrate reaction model

The source term can be determined based on the kinetic reaction rate of hydrate R_r in a given thermodynamic condition, expressed as follows,

$$\dot{m}_h = -M_h R_r, \tag{33a}$$

$$\dot{m}_g = M_g R_r, \tag{33b}$$

$$\dot{m}_w = N_h M_w R_r, \tag{33c}$$

where M_h, M_g, and M_w are the molar masses for hydrate, gas, and water, respectively, and N_h is the hydration number.

Accurate prediction of the hydrate dissociation rate is crucial for modeling MHBS. This study employs the Kim–Bishnoi kinetic reaction model (Kim et al., 1987), one of the most widely accepted hydrate reaction models, to describe the rate of hydrate reaction,

$$R_r = K_d A_s (p_e - p), \tag{34}$$

where K_d is the kinetic dissociation rate, A_s is the specific surface area of methane hydrate, p is the pore pressure, and p_e is the equilibrium pressure (hydrate stability pressure). Note that the pore pressure p, rather than the gas pressure p_g, is used to determine the reaction rate, as the hydrate phase balance is influenced by both gas and water pressures.

According to the experiments of Clarke and Bishnoi (2000, 2001b,a), K_d can be defined with an Arrhenius description,

$$K_d = K_0 \exp\left(-\frac{\Delta E}{RT}\right), \tag{35}$$

where K_0 is the kinetic dissociation constant, ΔE is the activation energy, and R is the gas constant.

The specific surface area A_s is defined as (White et al., 2020),

$$A_s = A_{geo} \begin{cases} \phi S_h, & p \le p_e \\ S_w S_g (1 - S_h), & p > p_e \end{cases}, \tag{36}$$

where ϕ is the porosity, S_h is the hydrate saturation, and A_{geo} is the surface area to volume ratio of hydrate particles. During the hydrate dissociation process, A_s primarily depends on the hydrate saturation, whereas for the hydrate formation process, it also relies on the saturations of water and gas.

The equilibrium pressure p_e is calculated using the empirical equation (Sloan, 1987; Liang et al., 2010; Ruan et al., 2012),

$$p_e = A_1 \exp\left(A_2 - \frac{A_3}{T + 273.15}\right), \tag{37}$$

where A_1, A_2, and A_3 are regression coefficients.

As this is a purely empirical equation, alternative models may also be employed (Makogon, 1997; Moridis, 2003; Chen et al., 2016; Hardwick and Mathias, 2018). Fig. 3 illustrates the phase equilibrium curve for three models, which provide similar predictions within the temperature range of −10 °C to 30 °C.

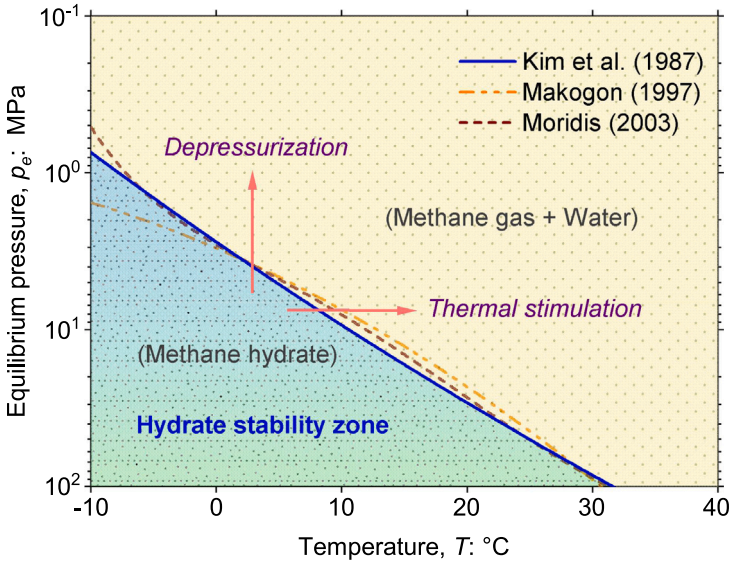

Fig. 3. Hydrate phase equilibrium curve.

2.3.2. Absolute and relative permeability model

The absolute permeability k_a is influenced by both porosity and hydrate saturation. The following equation is adopted to evaluate k_a,

$$k_a = k_0 f_\phi(\phi) f_{S_h}(S_h), \tag{38}$$

where k_0 is the hydrate–free permeability at the porosity of ϕ_0, and $f_\phi(\phi)$ and $f_{S_h}(S_h)$ are the functions that define the effects of porosity ϕ and hydrate saturation S_h, respectively. The function $f_\phi(\phi)$ is given by (Ye et al., 2022),

$$f_\phi = \left(\frac{\phi}{\phi_0}\right)^{1.5} \left(\frac{1-\phi}{1-\phi_0}\right)^{3}, \tag{39}$$

Among various options for f_{S_h}, the following expression is adopted (Masuda, 1999; Liang et al., 2010; Ruan et al., 2012),

$$f_{S_h}(S_h) = \begin{cases} k_h, & S_h > S_{hc} \\ k_h + (1-k_h)(S_{hc} - S_h)/S_h, & S_h < S_{hc} \end{cases}, \tag{40}$$

where S_{hc} is a threshold hydrate saturation beyond which the permeability is reduced to k_h. The value of k_h is dependent on the initial hydrate saturation S_{h0} and is typically estimated using the Masuda's model (Masuda, 1999),

$$k_h = (1 - S_h)^{m_h}, \tag{41}$$

where m_h is a permeability reduction parameter that depends on the pore structure.

The relative permeabilities k_{rw} and k_{rg} for the water and gas phases are calculated using a modified Corey's model (Corey, 1954; Liang et al., 2010; Ruan et al., 2012),

$$k_{r\pi} = \left[\frac{S_\pi/(1-S_h) - S_{r\pi}}{1 - S_{rw} - S_{rg}}\right]^{n_\pi}, \quad \pi = w, g, \tag{42}$$

where n_w and n_g are material constants.

2.3.3. Skeleton deformation model

It is assumed that the hydrate is formed after soil deposition, and initially soil skeleton carries the in situ effective stress $\boldsymbol{\sigma}'_0$. As the hydrate soil deforms, both the soil skeleton and the hydrate carry the additional stress increment. The rate of effective stress of the hydrate soil skeleton, $\dot{\boldsymbol{\sigma}}'$, can be calculated based on the following constitutive relation (Klar et al., 2010, 2013),

$$\dot{\boldsymbol{\sigma}} = \mathbb{D}^e_{sh} : (\dot{\boldsymbol{\varepsilon}} - \dot{\boldsymbol{\varepsilon}}^p) + \dot{\mathbb{D}}^e_{sh}(\mathbb{D}^e_{sh})^{-1}(\boldsymbol{\sigma}' - \boldsymbol{\sigma}'_0), \tag{43}$$

where $\mathbb{D}^e_{sh}$ is the elastic stiffness matrix including both the contribution of sediment grains and hydrate, $\dot{\boldsymbol{\varepsilon}}$ is the strain rate, $\dot{\boldsymbol{\varepsilon}}_p$ is the plastic strain rate, and $\boldsymbol{\sigma}'_0$ is the initial effective stress. The second term represents the stress relaxation part due to hydrate dissociation. As discussed in Klar et al. (2013), this term is very important in modeling the softening behavior of hydrate-bearing soil as the hydrate dissociates.

Under non-isothermal conditions, the strain rate can be decomposed into two parts: $\dot{\boldsymbol{\epsilon}} = \dot{\boldsymbol{\epsilon}}_s + \dot{\boldsymbol{\epsilon}}_T$, which represent the rates of mechanical deformation and thermal expansion, respectively. They are calculated as follows,

$$\dot{\boldsymbol{\epsilon}}_s = \frac{1}{2}\left[\nabla \boldsymbol{v}_s + (\nabla \boldsymbol{v}_s)^T\right], \text{ and } \dot{\boldsymbol{\epsilon}}_T = -\frac{1}{3}\beta_{sh}\dot{T}\boldsymbol{I}, \tag{44}$$

where β_{sh} is the average thermal expansivity of the hydrate-cemented sediment skeleton, evaluated by,

$$\beta_{sh} = \frac{(1-\phi)\beta_s + \phi S_h \beta_h}{1-\phi+\phi S_h}. \tag{45}$$

The elastic stiffness matrix $\mathbb{D}^e_{sh}$ is dependent on hydrate saturation, expressed as $\mathbb{D}^e_{sh} = \mathbb{D}^e_{sh}(S_h)$. Triaxial tests reveal that S_h influences Young's modulus, while having minimal effect on Poisson's ratio (Santamarina and Ruppel, 2010). The modified Young's modulus E is calculated using the following equation,

$$E = E_0 + a_h E_h (S_h)^{b_h}, \tag{46}$$

where E_0 and E_h are the Young's moduli of the hydrate–free skeleton and pure hydrate, respectively, and a_h and b_h are two material constants.

The incremental plastic strain is computed using a plastic potential function, P, as follows,

$$d\boldsymbol{\epsilon}_p = d\lambda \frac{\partial P}{\partial \boldsymbol{\sigma}'}, \tag{47}$$

where λ is the plastic multiplier. A modified non-associated Mohr–Coulomb strain-softening model is employed to describe the hydrate-dependent elasto-plastic behavior of MHBS (Menetrey and Willam, 1995; Klar et al., 2010). The yield function F and flow potential function P, defined in terms of friction angle φ, cohesion c, and dilation angle ψ, are given by,

$$F = R_{mc} q + p\tan\varphi - c, \tag{48}$$

$$P = \sqrt{(\epsilon c \tan\psi)^2 + \left(R_{mw} q\right)^2} + p\tan\psi, \tag{49}$$

where

$$R_{mc}(\theta,\varphi) = \frac{1}{\sqrt{3}\cos\varphi}\sin\left(\theta+\frac{\pi}{3}\right) + \frac{1}{3}\cos\left(\theta+\frac{\pi}{3}\right)\tan\varphi, \tag{50a}$$

$$R_{mw}(\theta,e) = \frac{4\left(1-e^2\right)\cos^2\theta + (2e-1)^2}{2\left(1-e^2\right)\cos\theta + (2e-1)\sqrt{4\left(1-e^2\right)\cos^2\theta + 5e^2 - 4e}} R_{mc}\left(\frac{\pi}{3},\varphi\right). \tag{50b}$$

Here, p and q are the effective mean stress and the deviatoric stress, respectively. θ is the Lode's angle, ϵ is the meridional eccentricity, and e is the deviatoric eccentricity.

Laboratory tests demonstrate that the peak cohesion and dilation of MHBS exhibit a positive correlation with hydrate saturation, whereas the friction angle remains largely unaffected (Soga et al., 2006; Waite et al., 2009). In this study, we establish a relation between peak cohesion and dilation with hydrate saturation through the following exponential expressions,

$$c_{peak,h} = c_{min} + \left(c_{max} - c_{min}\right)\exp[\eta_h(S_h - S_{hmax})], \tag{51a}$$

$$\psi_{peak,h} = \psi_{min} + \left(\psi_{max} - \psi_{min}\right)\exp[\eta_h(S_h - S_{hmax})], \tag{51b}$$

where $c_{peak,h}$ and $\psi_{peak,h}$ represent the peak cohesion and dilation at a given hydrate saturation S_h, c_{max} and ψ_{max} denote the peak cohesion and dilation at maximum hydrate saturation S_{hmax}, while c_{min} and ψ_{min} indicate the lower limits of cohesion and dilation as S_h approaches zero. η_h is a shape factor that governs the rate of decrease in strength as hydrate saturation diminishes. For simplicity, the peak friction angle is assumed to be constant, independent of hydrate saturation, *i.e.*, $\varphi_{peak,h} = \varphi_{max}$, as discussed earlier.

In addition, granular media subjected to large deformations may exhibit strain softening behavior. It has been observed that, while the peak strength of MHBS may vary with hydrate saturation, the residual strength at large shear strains remains relatively constant, regardless of hydrate saturation. This phenomenon arises because the hydrate's contribution to shear behavior is primarily due to its cohesive nature rather than frictional (Uchida et al., 2012). Therefore, it is reasonable to assume that the residual strength is independent of hydrate saturation. Although Uchida et al. (2012) used the critical state soil mechanics concept to model this behavior, this study introduces an exponential softening law (Pinyol et al., 2018; Lian et al., 2023), which describes the reduction in effective strength with increasing plastic deviatoric strain, ϵ^d_p, given as follows,

$$c = c_{res} + \left(c_{peak,h} - c_{res}\right)\exp\left(-\eta_s \epsilon^p_d\right), \tag{52a}$$

$$\varphi = \varphi_{res} + \left(\varphi_{peak,h} - \varphi_{res}\right)\exp\left(-\eta_s \epsilon^p_d\right), \tag{52b}$$

$$\psi = \psi_{peak,h}\exp\left(-\eta_s \epsilon^p_d\right), \tag{52c}$$

where c_{res} and ϕ_{res} denote the residual cohesion and friction angle, respectively, η_s is a shape factor that determines the sensitivity of shear strength to strain softening. For simplicity, we adopt the same shape factor for all strength variables. For the detailed effective stress update algorithm, please refer to Appendix A.

Remark 2. The mechanical model employed for MHBS in this study is relatively simplified, yet it can effectively capture the key hydrate-dependent characteristics. Although more sophisticated models, such as critical state models, can yield more realistic predictions (Uchida et al., 2012; Sun et al., 2018), they typically necessitate additional model parameters and remain fundamentally phenomenological in nature. An alternative approach involves multiscale modeling, wherein stress–strain relationships are derived from discrete element method (DEM)-based RVE simulations. This method offers more physics-based, state-dependent responses for granular materials and has been explored in the authors' previous work (Liang et al., 2023; Yu et al., 2024b). However, given the scope and focus of this study, the multiscale modeling will be deferred to future research.

3. Solution scheme based on material point method

The THMC-coupled system is governed by Eqs. (12), (14), (21), (22), and (27), with six primary unknowns to be solved: $\boldsymbol{v}_s$, $\boldsymbol{v}_w$, $\boldsymbol{v}_g$, p_w, p_g, and T. For dynamic large-deformation problems, explicit time integration in MPM offers simplicity by sequentially solving kinematic and thermal fields on the background mesh and updating pressure fields on material points using interpolated nodal velocities and temperatures. However, conventional explicit two-phase MPM encounters computational inefficiencies in low-permeability regimes due to numerical stability constraints, often necessitating excessively small time steps. Implicit schemes, while less sensitive to permeability variations, introduce convergence challenges and implementation complexity in multiphysics coupling.

To address these limitations, we propose a hybrid explicit–implicit scheme. In this approach, diffusion terms, such as drag forces and reaction source terms, are treated implicitly to alleviate stability restrictions, while other terms continue to be updated explicitly. This strategy balances computational efficiency, accuracy, and implementation simplicity, particularly in the context of low-permeability hydrate-bearing sediments where traditional explicit methods perform poorly.

3.1. Weak form

The weak form of momentum balance equations is obtained by multiplying arbitrary test functions $\delta\boldsymbol{v}_\pi$ with zeros on the boundaries, given by:

MHBS mixture,

$$\int_\Omega \delta\boldsymbol{v}_s\cdot\rho_{sh}\boldsymbol{a}_s dV+\int_\Omega \delta\boldsymbol{v}_s\cdot\phi S_w\rho_w\boldsymbol{a}_w dV+\int_\Omega \delta\boldsymbol{v}_s\cdot\phi S_g\rho_g\boldsymbol{a}_g dV=-\int_\Omega \boldsymbol{\sigma}:\nabla\delta\boldsymbol{v}_s dV+\int_{\partial\Omega}\delta\boldsymbol{v}_s\cdot\hat{\boldsymbol{t}}dS+\int_\Omega\delta\boldsymbol{v}_s\cdot\rho_m\boldsymbol{b}dV, \tag{53}$$

Water and gas phases:

$$\int_\Omega \delta\boldsymbol{v}_\pi\cdot\phi S_\pi\rho_\pi\boldsymbol{a}_\pi dV=\int_\Omega\nabla\delta\boldsymbol{v}_\pi\cdot(\phi S_\pi p_\pi\boldsymbol{I})dV+\int_{\partial\Omega}\delta\boldsymbol{v}_\pi\cdot\hat{\boldsymbol{i}}_\pi dS+\int_\Omega\delta\boldsymbol{v}_\pi\cdot\phi S_\pi\rho_\pi\boldsymbol{b}dV-\int_\Omega\delta\boldsymbol{v}_\pi\cdot\phi S_\pi\frac{\mu_\pi}{k_a k_{r\pi}}[\phi S_\pi(\boldsymbol{v}_\pi-\boldsymbol{v}_s)]dV,\quad \pi=w,g, \tag{54}$$

where $\rho_{sh}=(1-\phi)\rho_s+\phi S_h\rho_h$, $\hat{\boldsymbol{t}}$ is the mixture traction, and $\hat{\boldsymbol{t}}_\pi=\left(-\phi S_\pi p_\pi\boldsymbol{I}\right)\cdot\boldsymbol{n}$ is the phase traction.

Similarly, the weak form of the energy balance equation is obtained by introducing a test function δT, given by,

$$\int_\Omega\delta T\cdot C_m\dot{T}dV=-\int_\Omega\delta T\cdot\left[\phi S_w\rho_w c_w(\boldsymbol{v}_w-\boldsymbol{v}_s)+\phi S_g\rho_g c_g(\boldsymbol{v}_g-\boldsymbol{v}_s)\right]\cdot\nabla T dV+\int_\Omega(-\kappa_m\nabla T)\cdot\nabla\delta T dV-\int_{\partial\Omega}\delta T\cdot\hat{q}_e dS+\int_\Omega\delta T\cdot\theta\boldsymbol{\sigma}':\dot{\boldsymbol{\varepsilon}}^p dV+\int_\Omega\delta T\cdot q_e dV, \tag{55}$$

where $\hat{q}_e$ is the prescribed heat flux. The pore water and gas pressures are solved based on mass balance equations on particles, eliminating the need to derive their weak forms.

3.2. MPM spatial discretization

The generalized interpolation material point (uGIMP) method is employed to discretize the weak formulations (Bardenhagen and Kober, 2004). The method effectively mitigates the numerical noise when material points (interchangeable with "particles") cross the cell boundary in large deformation modeling. With the GIMP shape function $S_{Ip}=S_I\left(\boldsymbol{x}_p\right)$ and its gradient ∇S_{Ip} (I and p denote the indices of active nodes and particles, respectively), the weak forms are further discretized spatially. To facilitate explicit time integration, lumped matrices are utilized.

The energy balance equation can be reformulated into the following compact form,

$$C_m\dot{T}=\mathcal{E}_T^{source}+\mathcal{E}_T^{ext}+\mathcal{E}_T^{int}+\boldsymbol{Q}_w^{conv}\cdot(\boldsymbol{v}_w-\boldsymbol{v}_s)+\boldsymbol{Q}_g^{conv}\cdot(\boldsymbol{v}_g-\boldsymbol{v}_s), \tag{56}$$

where C_m represents the nodal heat capacity of the mixture, $\mathcal{E}_T^{source}$ is the nodal heat source, and $\mathcal{E}_T^{ext}$ and $\mathcal{E}_T^{int}$ denote the nodal external and internal heat, respectively. The terms $\boldsymbol{Q}_w^{conv}$ and $\boldsymbol{Q}_g^{conv}$ are the nodal coefficients of heat convection due to water and gas flow, respectively. These node-wise coefficients can be projected from particles according to,

$$(C_m)_I=\sum_p V_p C_{mp}S_{Ip}, \tag{57a}$$

$$(\boldsymbol{Q}_w^{conv})_I = -\sum_p V_p \phi_p S_{wp} \rho_{wp} c_{wp} \nabla T_p S_{Ip}, \tag{57b}$$

$$(\boldsymbol{Q}_g^{conv})_I = -\sum_p V_p \phi_p S_{gp} \rho_{gp} c_{gp} \nabla T_p S_{Ip}, \tag{57c}$$

$$(\mathcal{E}_T^{source})_I = \sum_p V_p q_{ep} S_{Ip}, \tag{57d}$$

$$(\mathcal{E}_T^{ext})_I = -\sum_p V_p h^{-1} \hat{q}_{ep} S_{Ip} + \sum_p V_p (\theta \boldsymbol{\sigma}' : \dot{\boldsymbol{\varepsilon}}^p) S_{Ip}, \tag{57e}$$

$$(\mathcal{E}_T^{int})_I = \sum_p V_p \left(-\kappa_m \nabla T_p\right) \cdot \nabla S_{Ip}. \tag{57f}$$

The momentum balance equations can be written into the following compact forms,

$$\boldsymbol{M}_{sh} \boldsymbol{a}_s + \boldsymbol{M}_w \boldsymbol{a}_w + \boldsymbol{M}_g \boldsymbol{a}_g = \boldsymbol{f}_m^{ext} + \boldsymbol{f}_m^{int}, \tag{58}$$

$$\boldsymbol{M}_\pi \boldsymbol{a}_\pi = \boldsymbol{f}_\pi^{ext} + \boldsymbol{f}_\pi^{int} + \boldsymbol{Q}_\pi^d \cdot (\boldsymbol{v}_\pi - \boldsymbol{v}_s), \quad \pi = w, g, \tag{59}$$

where $\boldsymbol{M}_{sh}$, $\boldsymbol{M}_w$, and $\boldsymbol{M}_g$ represent lumped nodal masses for the hydrate-solid skeleton, water phase, and gas phase, respectively. The terms $\boldsymbol{f}_{(*)}^{ext}$ and $\boldsymbol{f}_{(*)}^{int}$ denote the nodal external and internal forces for the mixture (m), water (w), and gas (g) phases, respectively. Additionally, $\boldsymbol{Q}_w^d$ and $\boldsymbol{Q}_g^d$ are the nodal coefficients of drag force for the water and gas phases, respectively. These coefficients at each node can be interpolated from particles according to,

$$(M_\pi)_I = \sum_p V_p \phi_p S_{\pi p} \rho_{\pi p} S_{Ip}, \quad \pi = w, g, \tag{60a}$$

$$(M_{sh})_I = \sum_p V_p \rho_{shp} S_{Ip}, \tag{60b}$$

$$(Q_\pi^d)_I = -\sum_p V_p (\phi_p S_{\pi p})^2 \frac{\mu_{\pi p}}{k_{ap} k_{r\pi p}} S_{Ip}, \quad \pi = w, g, \tag{60c}$$

$$(\boldsymbol{f}_\pi^{ext})_I = \sum_p V_p h_p^{-1} \hat{\boldsymbol{t}}_{\pi p} S_{Ip} + \sum_p V_p \phi_p S_{\pi p} \rho_{\pi p} \boldsymbol{b} S_{Ip}, \quad \pi = w, g, \tag{60d}$$

$$(\boldsymbol{f}_\pi^{int})_I = \sum_p V_p \phi_p S_{\pi p} p_{\pi p} \nabla S_{Ip}, \quad \pi = w, g, \tag{60e}$$

$$(\boldsymbol{f}_m^{ext})_I = \sum_p V_p h_p^{-1} \hat{\boldsymbol{t}} S_{Ip} + \sum_p V_p \rho_m \boldsymbol{b} S_{Ip}, \tag{60f}$$

$$(\boldsymbol{f}_m^{int})_I = -\sum_p V_p \boldsymbol{\sigma}_p : \nabla S_{Ip}. \tag{60g}$$

3.3. Solution of primary variables

3.3.1. Solution of velocity fields

In explicit time integration, the acceleration of each phase is computed from Eqs. (58) and (59) as follows,

$$\boldsymbol{a}_\pi^{k+1} = \left(\boldsymbol{f}_\pi^{ext} + \boldsymbol{f}_\pi^{int} + \boldsymbol{Q}_\pi^d \cdot (\boldsymbol{v}_\pi^k - \boldsymbol{v}_s^k)\right) / M_\pi, \quad \pi = w, g, \tag{61}$$

$$\boldsymbol{a}_s^{k+1} = \left(\boldsymbol{f}_m^{ext} + \boldsymbol{f}_m^{int} - \boldsymbol{M}_w \boldsymbol{a}_w^{k+1} - \boldsymbol{M}_g \boldsymbol{a}_g^{k+1}\right) / M_{sh}, \tag{62}$$

where the superscripts 'k' and '$k+1$' denote the current and the next time steps, respectively.

Remark 3. Critically, the explicit evaluation of drag forces in Eqs. (61) and (62) using the current-step velocity ($\boldsymbol{v}_\pi^k$) ties the critical time step size Δt to the magnitude of permeability. In low-permeability MHBS, this requires prohibitively small Δt to maintain numerical stability. To decouple the timestep constraints from permeability, we implicitly evaluate drag forces using velocity updates from the next timestep: $\boldsymbol{v}_\pi^{k+1} (= \boldsymbol{v}_\pi^k + \Delta t \boldsymbol{a}_\pi^{k+1}, \ \pi = s, w, g)$ instead of $\boldsymbol{v}_\pi^k$. This explicit–implicit treatment, combined with lumped matrices, reduces the problem to solving the following node-based 3×3 linear equation system,

$$\begin{bmatrix} \boldsymbol{M}_{sh} & \boldsymbol{M}_w & \boldsymbol{M}_g \\ \Delta t \boldsymbol{Q}_w^d & \boldsymbol{M}_w - \Delta t \boldsymbol{Q}_w^d & 0 \\ \Delta t \boldsymbol{Q}_g^d & 0 & \boldsymbol{M}_g - \Delta t \boldsymbol{Q}_g^d \end{bmatrix} \begin{bmatrix} \boldsymbol{a}_s^{k+1} \\ \boldsymbol{a}_w^{k+1} \\ \boldsymbol{a}_g^{k+1} \end{bmatrix} = \begin{bmatrix} \boldsymbol{f}_m^{ext} + \boldsymbol{f}_m^{int} \\ \boldsymbol{f}_w^{ext} + \boldsymbol{f}_w^{int} + \boldsymbol{Q}_w^d \cdot (\boldsymbol{v}_w^k - \boldsymbol{v}_s^k) \\ \boldsymbol{f}_g^{ext} + \boldsymbol{f}_g^{int} + \boldsymbol{Q}_g^d \cdot (\boldsymbol{v}_g^k - \boldsymbol{v}_s^k) \end{bmatrix}. \tag{63}$$

Such implicit treatment of drag force terms allows for the use of larger time steps in low-permeability problems without incurring additional computational costs associated with large-scale matrix handling and solving.

3.3.2. Solution of temperature field

Again, in explicit time integration, the rate of temperature change is computed from Eq. (56) as follows,

$$\dot{T}^{k+1} = \left(\mathcal{E}_T^{source} + \mathcal{E}_T^{ext} + \mathcal{E}_T^{int} + \boldsymbol{Q}_w^{conv} \cdot (\boldsymbol{v}_w^k - \boldsymbol{v}_s^k) + \boldsymbol{Q}_g^{conv} \cdot \left(\boldsymbol{v}_g^k - \boldsymbol{v}_s^k\right)\right) / C_m, \tag{64}$$

Remark 4. The source term q_e is sensitive to temperature T, and small variations in the primary variables can lead to considerable changes in them, causing inaccuracy and instability issues at certain time steps. To address this, we linearize the source term using a first-order Taylor expansion,

$$q_e(T^{k+1}) = q_e(T^k) + \Delta t \frac{\partial q_e}{\partial T} \dot{T}^{k+1}, \tag{65}$$

Consequently, the rate of temperature can be calculated by,

$$\dot{T}^{k+1} = \left(\mathcal{E}_T^{source} + \mathcal{E}_T^{ext} + \mathcal{E}_T^{int} + \boldsymbol{Q}_w^{conv} \cdot (\boldsymbol{v}_w^k - \boldsymbol{v}_s^k) + \boldsymbol{Q}_g^{conv} \cdot (\boldsymbol{v}_g^k - \boldsymbol{v}_s^k) \right) / \widetilde{C}_m, \tag{66}$$

where

$$(\tilde{C}_m)_I = \sum_p V_p \left(C_{mp} + \Delta t \frac{\partial q_e}{\partial T} \right) S_{Ip}. \tag{67}$$

Note that although q_e also depends on pressure, p^k is used in the calculation of $\dot{T}^{k+1}$, as a one-step sequential scheme is employed in this work, with temperature being solved prior to pressure.

3.3.3. Solution of pressure fields

After updating the velocities and temperature, the pore water and gas pressures can be directly computed at the particle level by solving the following set of equations,

Water phase:

$$K_{ww}\dot{p}_{wp}^{k+1} + K_{wg}\dot{p}_{gp}^{k+1} - \beta_{ws}\dot{T}_p^{k+1} + S_w\dot{\varepsilon}_{sp}^{k+1} + \phi S_w \left(\dot{\varepsilon}_{wp}^{k+1} - \dot{\varepsilon}_{sp}^{k+1} \right) = \frac{\dot{m}_w}{\rho_w}, \tag{68}$$

Gas phase:

$$K_{gg}\dot{p}_{gp}^{k+1} + K_{gw}\dot{p}_{wp}^{k+1} - \beta_{ghs}\dot{T}_p^{k+1} + \left(S_g + S_h \right) \dot{\varepsilon}_{sp}^{k+1} + \phi S_g \left(\dot{\varepsilon}_{gp}^{k+1} - \dot{\varepsilon}_{sp}^{k+1} \right) = \frac{\dot{m}_g}{\rho_g} + \frac{\dot{m}_h}{\rho_h}, \tag{69}$$

where $\dot{\varepsilon}_{sp}^{k+1}$, $\dot{\varepsilon}_{wp}^{k+1}$, and $\dot{\varepsilon}_{gp}^{k+1}$ are the volumetric strain rate of the solid, water, and gas phases, with the coefficients K_{ww}, K_{gg}, K_{wg}, and K_{gw} given by,

$$K_{ww} = \frac{\phi S_w}{K_w} + \phi \frac{\partial S_w}{\partial p_w}, \tag{70a}$$

$$K_{gg} = \frac{\phi S_g}{\rho_g} \frac{M_g}{RT} + \phi \frac{\partial S_w}{\partial p_w}, \tag{70b}$$

$$K_{wg} = K_{gw} = -\phi \frac{\partial S_w}{\partial p_w}. \tag{70c}$$

Remark 5. Similar to the heat source, the mass source terms are sensitive to variations in pore pressure and temperature. The temperature-dependent K_d and p_e are computed using the updated T^{k+1}. Additionally, to enhance numerical accuracy and stability, pore pressure is implicitly evaluated using $p^{k+1}(= p^k + \Delta t \dot{p}^{k+1})$, as follows,

$$\frac{\dot{m}_w}{\rho_w} = \frac{N_h M_w}{\rho_w} K_d A_s (p_e - p^{k+1}), \tag{71a}$$

$$\frac{\dot{m}_g}{\rho_g} + \frac{\dot{m}_h}{\rho_h} = \left(\frac{M_g}{\rho_g} - \frac{M_h}{\rho_h} \right) K_d A_s (p_e - p^{k+1}). \tag{71b}$$

Then, the mass balance equations are discretized as,

$$\begin{bmatrix} \widetilde{K}_{ww} & \widetilde{K}_{wg} \\ \widetilde{K}_{gw} & \widetilde{K}_{gg} \end{bmatrix} \begin{bmatrix} \dot{p}_{wp}^{k+1} \\ \dot{p}_{gp}^{k+1} \end{bmatrix} = \begin{bmatrix} \widetilde{f}_w \\ \widetilde{f}_g \end{bmatrix}, \tag{72}$$

where

$$\widetilde{K}_{ww} = K_{ww} + \Delta t \frac{N_h M_w}{\rho_w} K_d A_s \chi_w, \tag{73a}$$

$$\widetilde{K}_{wg} = K_{wg} + \Delta t \frac{N_h M_w}{\rho_w} K_d A_s \chi_g, \tag{73b}$$

$$\widetilde{K}_{gg} = K_{gg} + \Delta t \left(\frac{M_g}{\rho_g} - \frac{M_h}{\rho_h} \right) K_d A_s \chi_g, \tag{73c}$$

$$\widetilde{K}_{gw} = K_{gw} + \Delta t \left(\frac{M_g}{\rho_g} - \frac{M_h}{\rho_h} \right) K_d A_s \chi_w, \tag{73d}$$

$$\widetilde{f}_w = \frac{N_h M_w}{\rho_w} K_d A_s (p_e - p^k) + \beta_{ws} \dot{T}_p^{k+1} + S_w \varepsilon_{sp}^{k+1} + \phi_p S_w \left(\dot{\varepsilon}_{wp}^{k+1} - \dot{\varepsilon}_{sp}^{k+1} \right), \tag{73e}$$

$$\widetilde{f}_g = \left(\frac{M_g}{\rho_g} - \frac{M_h}{\rho_h}\right) K_d A_s (p_e - p^k) + \beta_{ghs} \dot{T}_p^{k+1} + \left(S_h + S_g\right) \dot{\varepsilon}_{sp}^{k+1} + \phi_p S_g \left(\dot{\varepsilon}_{gp}^{k+1} - \dot{\varepsilon}_{sp}^{k+1}\right). \tag{73f}$$

3.4. Complete solution procedure

The solution procedure of the proposed THMC-MPM for modeling MHBS is outlined as follows.

(1) Assign initial material point properties, including $\boldsymbol{v}_{sp}^0$, $\boldsymbol{v}_{wp}^0$, $\boldsymbol{v}_{gp}^0$, p_{wp}^0, p_{gp}^0, T_p^0, V_p^0, ρ_{sp}^0, ρ_{hp}^0, ρ_{wp}^0, ρ_{gp}^0, ϕ_p^0, S_{hp}^0, S_{wp}^0, S_{gp}^0, k_{ap}^0, k_{rwp}^0, k_{rgp}^0. Note that initial permeability should be evaluated based on the porosity and saturations.

(2) Initialize background mesh and compute shape functions.

(3) Evaluate source terms based on the current thermodynamic conditions: calculate the kinetic reaction rate R_r based on Eqs. (34)–(37), and then compute the source terms.

(4) Map particle properties, including mass, momentum, heat capacity, and heat, to nodes using Eqs. (57a) and (60a)–(60b). Then, compute the nodal velocities $\boldsymbol{v}_{sI}^k$, $\boldsymbol{v}_{wI}^k$, and $\boldsymbol{v}_{gI}^k$, as well as the temperature T_I^k at the current time step,

$$\boldsymbol{v}_{sI}^k = \left(M_{sh}^k\right)_I^{-1} \sum_p \left(m_{sp}^k + m_{hp}^k\right) \boldsymbol{v}_{sp}^k S_{Ip}, \tag{74a}$$

$$\boldsymbol{v}_{\pi I}^k = \left(M_{\pi}^k\right)_I^{-1} \sum_p m_{\pi p}^k \boldsymbol{v}_{\pi p}^k S_{Ip}, \pi = w, g, \tag{74b}$$

$$T_I^k = \left(C_m^k\right)_I^{-1} \sum_p V_p^k C_{mp}^k S_{Ip}. \tag{74c}$$

(5) Assembly nodal internal and external forces/heats according to Eqs. (57b)–(57f), (60c)–(60e), and (67). Then, calculate the nodal temperature $\dot{T}^{k+1}$ based on Eq. (64) and calculate acceleration $\boldsymbol{a}_{sI}^{k+1}$, $\boldsymbol{a}_{wI}^{k+1}$, and $\boldsymbol{a}_{gI}^{k+1}$ based on Eq. (63). And then, compute the updated nodal temperature T_I^{k+1} and velocities $\boldsymbol{v}_{sI}^{k+1}$, $\boldsymbol{v}_{wI}^{k+1}$, and $\boldsymbol{v}_{gI}^{k+1}$,

$$\mathcal{V}_I^{k+1} = \mathcal{V}_I^k + \dot{\mathcal{V}}_I^{k+1} \Delta t, \quad \mathcal{V} = \boldsymbol{v}_s, \boldsymbol{v}_w, \boldsymbol{v}_g, T, \tag{75}$$

where $\mathcal{V}$ represents different field variables.

(6) Map updated nodal variables to particles and update particle primary variables using the FLIP strategy,

$$\mathcal{V}_p^{k+1} = \mathcal{V}_p^k + \Delta t \sum_I \dot{\mathcal{V}}_I^{k+1} S_{Ip}, \quad \mathcal{V} = \boldsymbol{v}_s, \boldsymbol{v}_w, \boldsymbol{v}_g, T. \tag{76}$$

(7) Update particle strain and stress. The strain rate is calculated by,

$$\dot{\boldsymbol{\varepsilon}}_{\pi p}^{k+1} = \frac{1}{2}\left[\sum_I \boldsymbol{v}_{\pi I}^k \nabla S_{Ip} + \left(\sum_I \boldsymbol{v}_{\pi I}^k \nabla S_{Ip}\right)^T\right], \quad \pi = s, w, g. \tag{77}$$

The particle stress is updated based on an objective stress rate, *e.g.*, Jaumann stress rate, to accommodate large deformation and rotations,

$$\dot{\boldsymbol{\sigma}}_p'^{k+1} = \mathbb{D}_{sh}^e : \dot{\boldsymbol{\varepsilon}}_p^{k+1} + \boldsymbol{\sigma}_p'^k \cdot \dot{\boldsymbol{\omega}}_p^{k+1} - \dot{\boldsymbol{\omega}}_p^{k+1} \cdot \boldsymbol{\sigma}_p'^k + \dot{\mathbb{D}}_{sh}^e (\mathbb{D}_{sh}^e)^{-1} (\boldsymbol{\sigma}_p'^k - \boldsymbol{\sigma}_{p0}'), \tag{78}$$

where $\dot{\boldsymbol{\omega}}_p$ is the rate of the spin tensor, and $\dot{\boldsymbol{\varepsilon}}_{Tp}^{k+1}$ is the particle thermal strain calculated using Eq. (44).

(8) Update porosity and hydrate saturation based on Eqs. (19) and (20),

$$\dot{\phi}_p^{k+1} = \left(1 - \phi_p^{k+1}\right)\left[-\beta_s \dot{T}_p^{k+1} + \dot{\varepsilon}_{sp}^{k+1}\right], \tag{79}$$

$$\dot{S}_{hp}^{k+1} = (\phi_p^{k+1})^{-1}\left(\frac{\dot{m}_h}{\rho_h} + \beta_{sh} \dot{T}_p^{k+1} - S_{hp}^{k+1} \dot{\varepsilon}_{sp}^{k+1}\right), \tag{80}$$

where $\dot{\varepsilon}_{sp}^{k+1} = tr\left(\dot{\boldsymbol{\varepsilon}}_{sp}^{k+1}\right)$.

(9) Update pore water and gas pressures based on Eq. (72).

(10) Update the densities of each phase using Eqs. (10) and (11), compute water and gas saturations using Eqs. (4)–(6), and compute the absolute and relative permeability according to Eqs. (38)–(42).

(11) Update particle displacements $\boldsymbol{u}_p$ and positions $\boldsymbol{x}_p$ by mid-point method,

$$\Delta \boldsymbol{x}_p^{k+1} = \Delta \boldsymbol{u}_p^{k+1} = \boldsymbol{v}_{sp}^k \Delta t + \frac{1}{2} \boldsymbol{a}_{sp}^{k+1} \Delta t^2. \tag{81}$$

(12) If $t < t^{final}$, proceed to the next time step.

The flow chart of the MPM solution algorithm is depicted in Fig. 4.

4. Validation of the proposed THMC-coupled MPM

This section validates the proposed THMC-MPM framework through two benchmark cases. The first case replicates Masuda's sandstone core hydrate dissociation experiment (Masuda, 1999), focusing on the TMC response while neglecting mechanical deformation. The second case solves an extended Terzaghi consolidation problem from the 2nd international code comparison study on MHBS multiphysics (White et al., 2020), providing a rigorous evaluation of the performance for modeling fully coupled THMC processes during hydrate phase transitions.

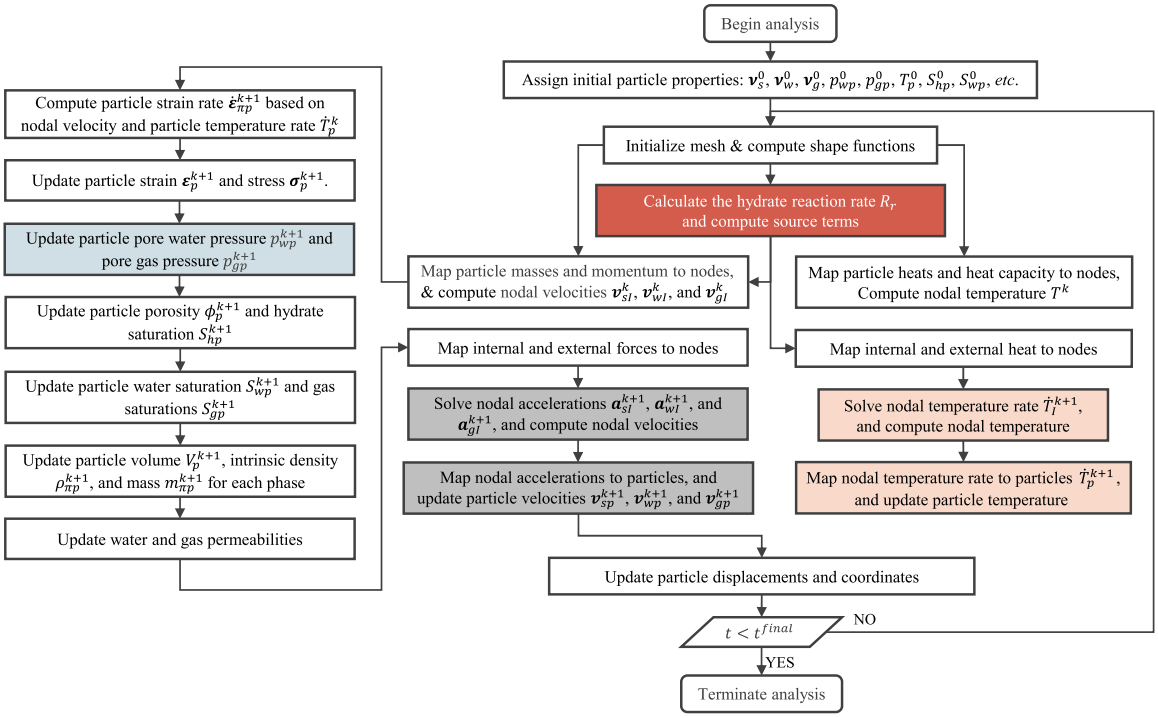

Fig. 4. Solution flow chart for modeling MHBS using MPM.

Table 1
Model dimensions, initial and boundary conditions.

Parameters		Value
Dimensions of the cone	Length of the cone, L: mm	300
	Diameter of the cone, d: mm	50.8
Initial conditions	Initial porosity, ϕ	0.182
	Initial hydrate saturation, S_{h0}	0.501
	Initial water saturation, S_{w0}	0.351
	Initial gas saturation, S_{g0}	0.148
	Initial pore pressure, p_0: MPa	3.75
	Initial temperature, T_0: °C	2.3
Boundary conditions	Outlet boundary pressure, p_a: MPa	2.84
	Air bath temperature, T_a: °C	2.0

4.1. THC validation: Masuda's hydrate dissociation experiment

Masuda's experiment (Masuda, 1999) serves as a foundational benchmark for validating hydrate dissociation models (Nazridoust and Ahmadi, 2007; Liang et al., 2010; Zhao et al., 2012; Ruan et al., 2012; Chen et al., 2016; Hardwick and Mathias, 2018; Ye et al., 2022). The experimental setup, as illustrated in Fig. 5, involved a Berea sandstone core (300 mm in length and 30.2 mm in radius) saturated with methane hydrate, water, and gas, enclosed within a rubber sleeve. Hydrate dissociation was induced by a pressure reduction at the fluid outlet (front boundary), while thermal conditions were maintained via constant-temperature air bath heating. Key experimental measurements included surface temperatures at three locations (T1: 75 mm, T2: 150 mm, and T3: 225 mm from the outlet), far-field pressure, and cumulative methane gas production.

The MPM simulation simplified the problem to axisymmetric geometry, neglecting gravity effects and mechanical deformation by constraining solid velocities to zero. Axisymmetric formulations were derived from plane strain formulations (Sulsky and Schreyer, 1996; Nairn and Guilkey, 2015; Yu et al., 2024c) by recalculating material point volume, surface areas, and gradients in cylindrical coordinates. Despite numerical challenges near $r = 0$, the zero-flux boundary condition at the core center ensured stable simulations with a uniform mesh. The initial and boundary conditions, along with material parameters, are provided in Tables 1 and 2.

Fig. 6 illustrates the spatiotemporal evolution of gas pressure (p_g), temperature (T), hydrate saturation (S_h), and gas saturation (S_g) at five critical time frames. During the initial reaction stage ($t = 10$ min), the reduction in gas pressure propagates from the left outlet boundary, triggering hydrate dissociation and localized cooling due to endothermic reactions. Over time (*e.g.*, at $t = 1$ h), the temperature gradient between the outlet (maintained by the warm air bath) and the inner core (axisymmetric boundary) becomes

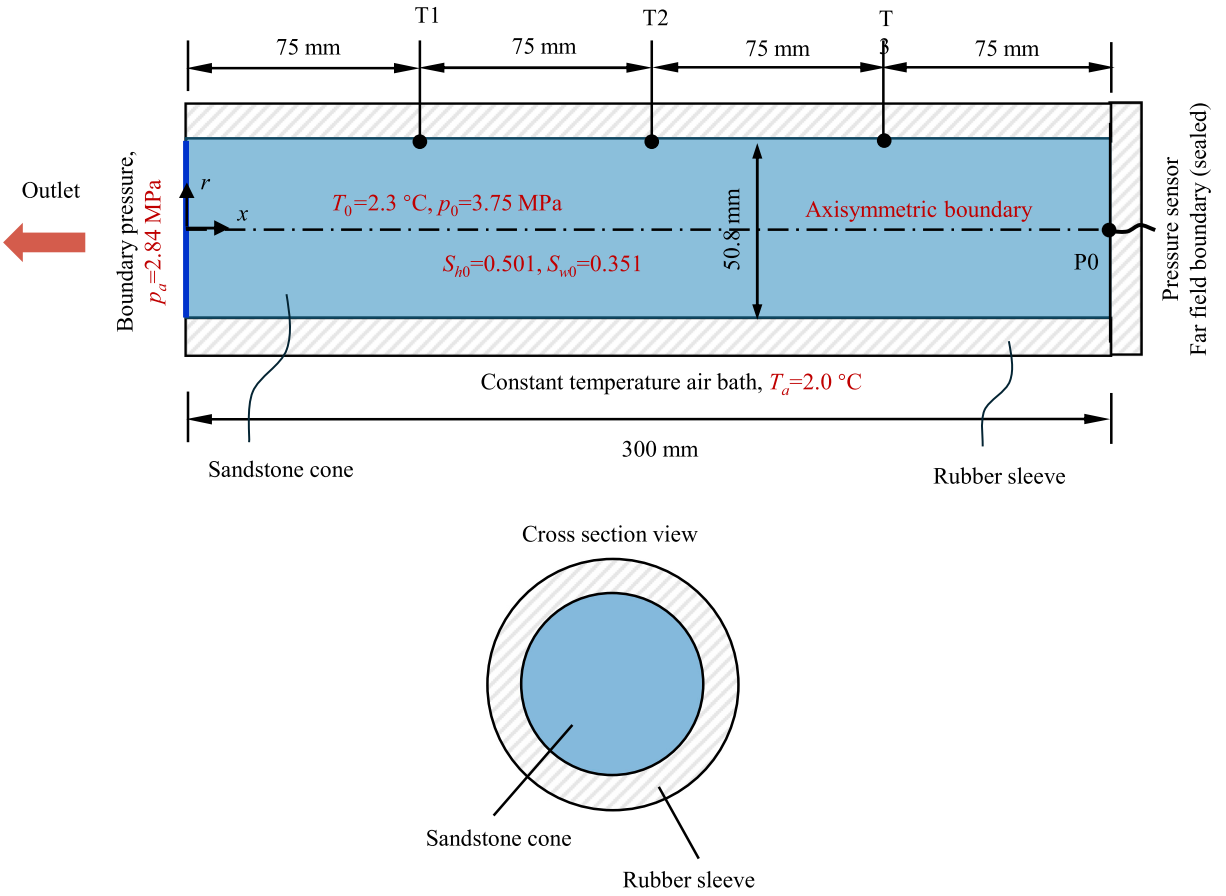

Fig. 5. The model setup for Masuda's sandstone core hydrate dissociation experiment. Three temperature sensors are uniformly positioned at surface points T1, T2, and T3 along the length of the sandstone core. Additionally, a pressure sensor is located at point P0, centered on the sealed end of the core.

Table 2
Material parameters used in MPM simulation for Masuda's benchmark.

Parameters	Solid, s	Hydrate, h	Water, w	Gas, g
Initial density, ρ_π: kg/m^3	2600	900	1000	–
Specific heat capacity, c_π: J/(kg °C)	800	2010	4200	2100
Thermal conductivity, κ_π: W/(m °C)	8.8	0.393	0.556	0.0335
Viscosity, μ_π: Pa s	–	–	1×10^{-3}	7×10^{-6}
Thermal expansivity, β_π: 1/°C	1.5×10^{-5}	1.5×10^{-5}	4×10^{-4}	–
Molar mass, M_π: kg/mol	–	0.124	0.018	0.016
Gas constant, R	–	–	–	8.314
Kinetic hydrate dissociation rate, R_r	K_0 = 36,000 mol/(m^2 Pa s), ΔE = 78,151 J/mol, $A_{geo}=7.5\times10^5$/m, A_1 = 1.15, A_2 = 49.3185, A_3 = 9459			
Effective saturation, S_e	$p_0=1\times10^4$ Pa, m = 0.5, S_{wr} = 0.2, S_{gr} = 0.3			
Heat source, $\Delta H=C_0+C_1T$: J/kg	C_0 = 446,120 J/kg, C_1 = 132.638 J/(kg °C)			
Absolute permeability k_a: m^2	$k_0=9.67\times10^{-14}$ m^2, k_h = 0.01, $S_{hc}=1\times10^{-4}$			
Relative permeability, $k_{r\pi}$	n_w = 0.82, n_g = 2.11			

more pronounced, reflecting the dynamics of heat transfer. By t = 4 h, complete hydrate dissociation leads to the stabilization of p_g and T, while S_g continues to decrease gradually as gas drainage persists.

Fig. 7(a–b) compares the simulated temperature profiles at probes T1 (near the outlet) and T3 (at the far end) with experimental data (Masuda, 1999). The FVM simulation results by Hardwick and Mathias (2018) are also presented for comparison. In their simulation, the capillary pressure is neglected; Godunov's method is adopted to discretize the governing equations; and the relative permeability and the convective heat transfer coefficient are carefully calibrated to reconcile Masuda (1999)'s data set in its entirety. From Fig. 7(a–b), it can be observed that both probes exhibit an initial rapid cooling phase, followed by gradual reheating toward the

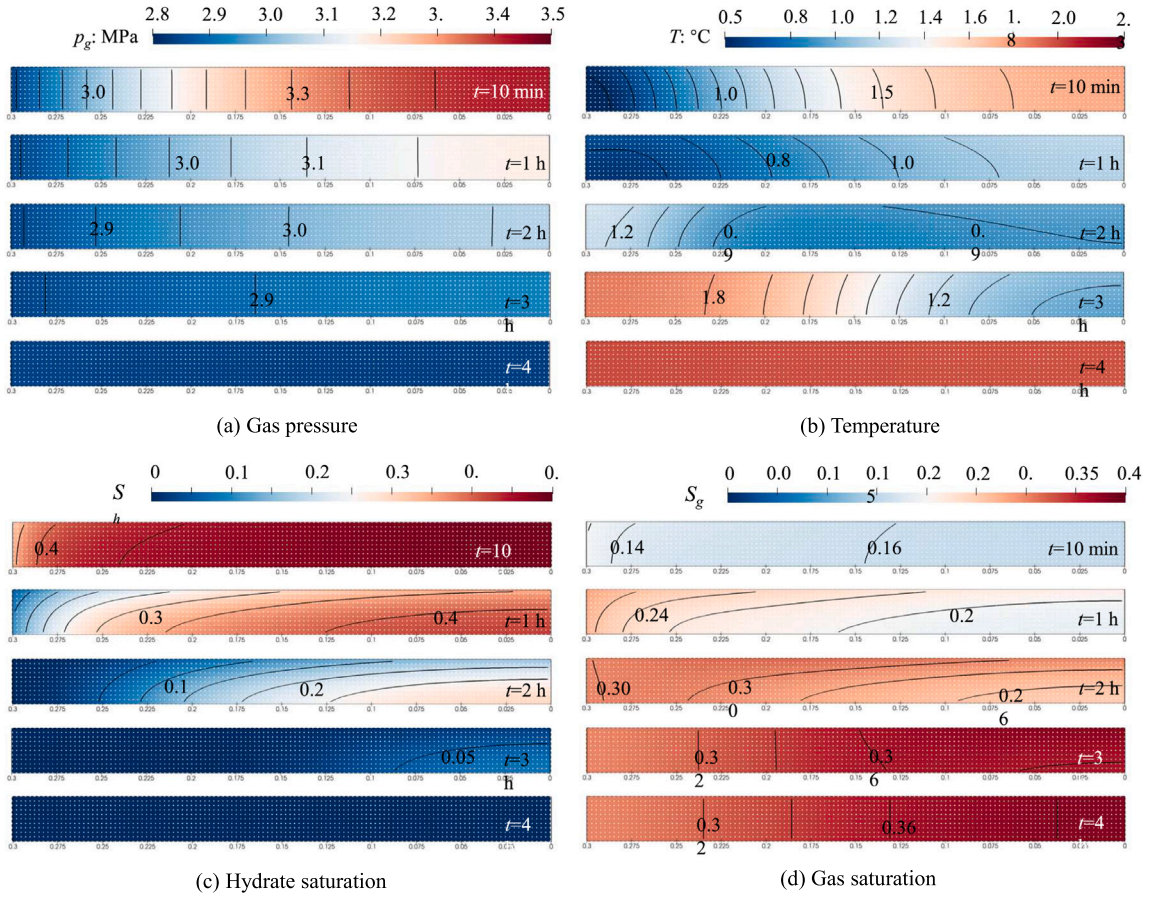

Fig. 6. Contours of (a) gas pressure p_g, (b) temperature T, (c) hydrate saturation S_h, and (d) gas saturation S_g at the time instances of 10 min, 1 h, 2 h, 3 h, and 4 h.

ambient temperature (2.0 °C). The delayed thermal response at T3 is attributed to its greater distance from the hydrate dissociation front. The MPM simulation results closely align with the experimental measurements and are consistent with the FVM trends, validating the accuracy of the THC coupling in the proposed framework. Fig. 7(c–d) further validates the model by comparing far-end gas pressure and cumulative methane production. The gas volume (converted to standard conditions: 101.4 kPa, 15.56 °C, and standard methane gas density $\rho_{g,std} = 0.6789\,\mathrm{kg/m^3}$) accounts for both outlet production and retained pore gas. The observed nonlinear pressure decline reflects permeability variations associated with hydrate dissociation. Minor deviations from the FVM results are likely due to the omission of gas-water phase pressure differences in Hardwick and Mathias (2018)'s FVM formulation. Overall, the MPM framework quantitatively and qualitatively reproduces key hydrate dissociation dynamics, demonstrating its robustness and efficacy in capturing coupled THC processes.

4.2. THMC validation: Extended Terzaghi problem

The BP2 benchmark from the international MHBS code comparison study (White et al., 2020) is utilized to validate the fully coupled THMC capabilities of the proposed MPM framework. This benchmark extends the Terzaghi 1D consolidation problem by incorporating methane hydrate kinetics to evaluate the bidirectional interactions among hydrate phase transitions, fluid flow, and mechanical deformation. The problem setup consists of a horizontally confined soil column ($L = 1$ m) with no gravitational effects, as depicted in Fig. 8(a). The initial conditions include: $S_{w0} = 0.6$, $S_{g0} = 0.4$, and $S_{h0} = 0$, and $\phi = 0.15$. The boundary conditions include (1) full fixation at the left end, (2) prescribed surcharge and free drainage at the right end, and (3) impermeable walls with roller supports on lateral boundaries. The column is thermally insulated, and mechanical loading follows a ramped compressive stress profile as shown in Fig. 8(b): linearly increasing at 0.01 MPa/s for 1000 s, then decreasing at the same rate over the next 1000 s. Unlike the traditional Terzaghi consolidation problem, this problem introduces non-isothermal effects arising from hydrate phase transitions (formation/dissociation). The material properties assume a linear elastic stress–strain relationship, as summarized in Table 3. The computational domain is discretized into uniform 50 quadrilateral cells with four material points per cell. Two cases are analyzed:

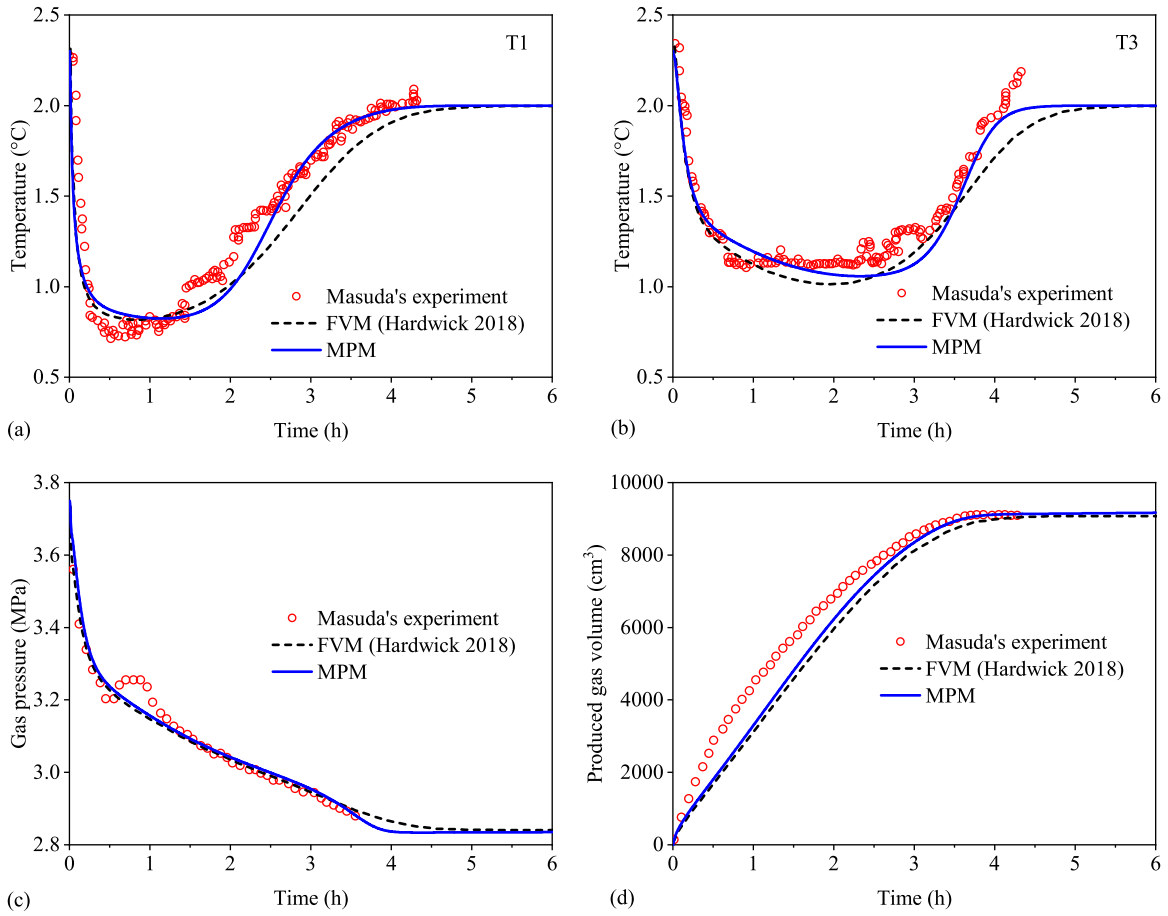

Fig. 7. Evolution of temperature at probe (a) T1 and (b) T3; (c) gas pressure at far-end point P0; and (d) gas volume, including the gas released from the outlet and the gas retained within the pore space of the core sandstone, at standard condition (101.4 kPa and 15.56 °C).

Table 3
Material parameters used in MPM simulation for extended Terzaghi's benchmark.

Parameters	Solid, s	Hydrate, h	Water, w	Gas, g
Initial density, ρ_π: kg/m^3	2600	900	1000	–
Specific heat capacity, c_π: J/(kg °C)	800	2010	4200	2100
Thermal conductivity, κ_π: W/(m °C)	3	0.5	0.5	0.044
Viscosity, μ_π: Pa s	–	–	1×10^{-3}	7×10^{-6}
Thermal expansivity, β_π: 1/°C	0	0	0	–
Molar mass, M_π: kg/mol	–	0.124	0.018	0.016
Gas constant, R	–	–	–	8.314
Kinetic hydrate dissociation rate, R_r	$K_d = 2.5\times10^{-10}$ mol/(m^2 Pa s), $A_{geo} = 1\times10^6$/m, $A_1 = 1$, $A_2 = 38.98$, $A_3 = 8533.8$			
Effective saturation, S_e	$p_0 = 5\times10^4$ Pa, $m = 0.3$, $S_{wr} = 0.2$, $S_{gr} = 0.4$			
Heat source, $\Delta H = C_0 + C_1 T$: J/kg	$C_0 = 473{,}632$ J/kg, $C_1 = 140.117$ J/(kg K)			
Absolute permeability k_a: m^2	$k_0 = 1.53\times10^{-15}$ m^2, $m = 3$			
Relative permeability, $k_{r\pi}$	$n_w = 4$, $n_g = 2$			
Elastic parameters, E, ν	$E_0 = 9\times10^7$ Pa, $E_h = 2\times10^9$ Pa, $a_h = 1$, $b_h = 1$			

- Case 1: Hydrate kinetics are disabled ($K_d = 0$), isolating poroelastic effects; and
- Case 2: Hydrate kinetics are active ($K_d = 2.5\times10^{-10}$ mol/(m^2 Pa s)), enabling full THMC coupling.

This comparative analysis isolates the role of hydrate phase transitions in consolidation dynamics, providing a rigorous validation of the framework's ability to resolve complex multiphysics interactions.

For Case 1 (hydrate kinetics disabled), the problem reduces to a modified Terzaghi consolidation problem incorporating gas compressibility and weak thermal coupling. Fig. 9 presents a comparison of the simulated pore pressure at $x = 0.6$ m and surface

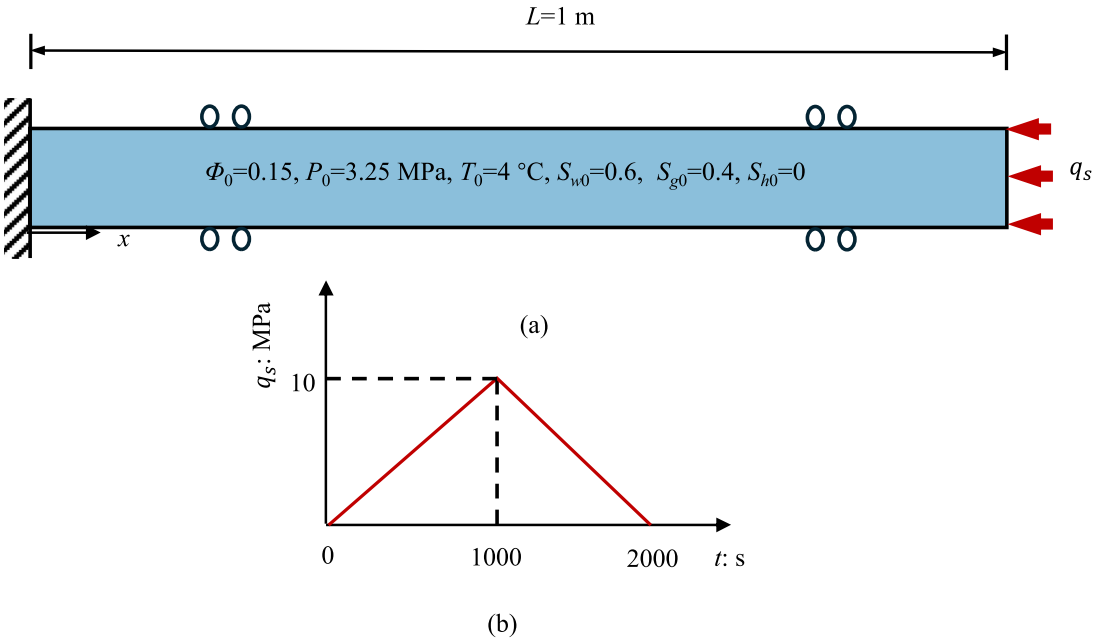

Fig. 8. (a) Geometry, initial and boundary conditions of the extended Terzaghi consolidation problem, and (b) the loading function.

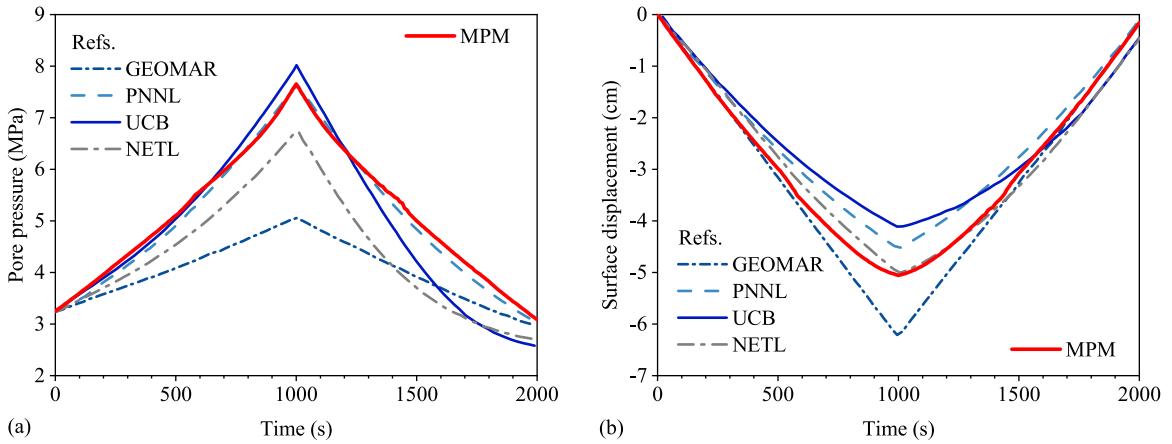

Fig. 9. Case 1 (hydrate kinetics disabled): evolution of (a) pore pressure at $x = 0.6$ m and (b) surface displacement (positive = rightward).

displacement with reference results from participating codes in White et al. (2020). Key observations include: (1) pore pressure rises from 3.25 MPa to approximately 8 MPa during the loading stage (0–1000 s), and subsequently decreases to its initial value during the unloading stage (1000–2000 s); (2) surface displacement shows consolidation (compression) during loading, followed by rebound during unloading; and (3) all codes, except GEOMAR, demonstrate nonlinear evolution of pressure and displacement, which can be attributed to capillary suction effects. Slight variations in peak values are observed across the different codes, likely due to differences in constitutive models and parameter assumptions. Nevertheless, the MPM results align qualitatively with the established trends, confirming the efficacy of its poroelastic coupling implementation.

In Case 2 (hydrate kinetics enabled), hydrate formation and dissociation are driven by the buildup of excess pore pressure during loading. When the pore pressure (p) exceeds the hydrate equilibrium pressure (p_e, equaling 3.6 MPa at 4.0 °C), hydrate formation is initiated. Conversely, when $p < p_e$, hydrate dissociation occurs. Fig. 10 shows the evolution of pore pressure, hydrate saturation, temperature at $x = 0.6$ m, and surface displacement. The following dynamic behaviors are observed. (1) During the loading stage ($t = 0$–1000 s): when $p < p_e$ (approximately $t < 100$ s), the trends in pore pressure and displacement closely resemble those in Case 1; no hydrate formation occurs ($S_h = 0$), and the temperature remains constant at 4 °C; when $p > p_e$ ($t > 100$ s), hydrate formation is initiated; this process dampen the rate of pore pressure increase as gas and water are consumed to form hydrate; simultaneously, exothermic reactions associated with hydrate formation cause a localized rise in temperature. (2) During

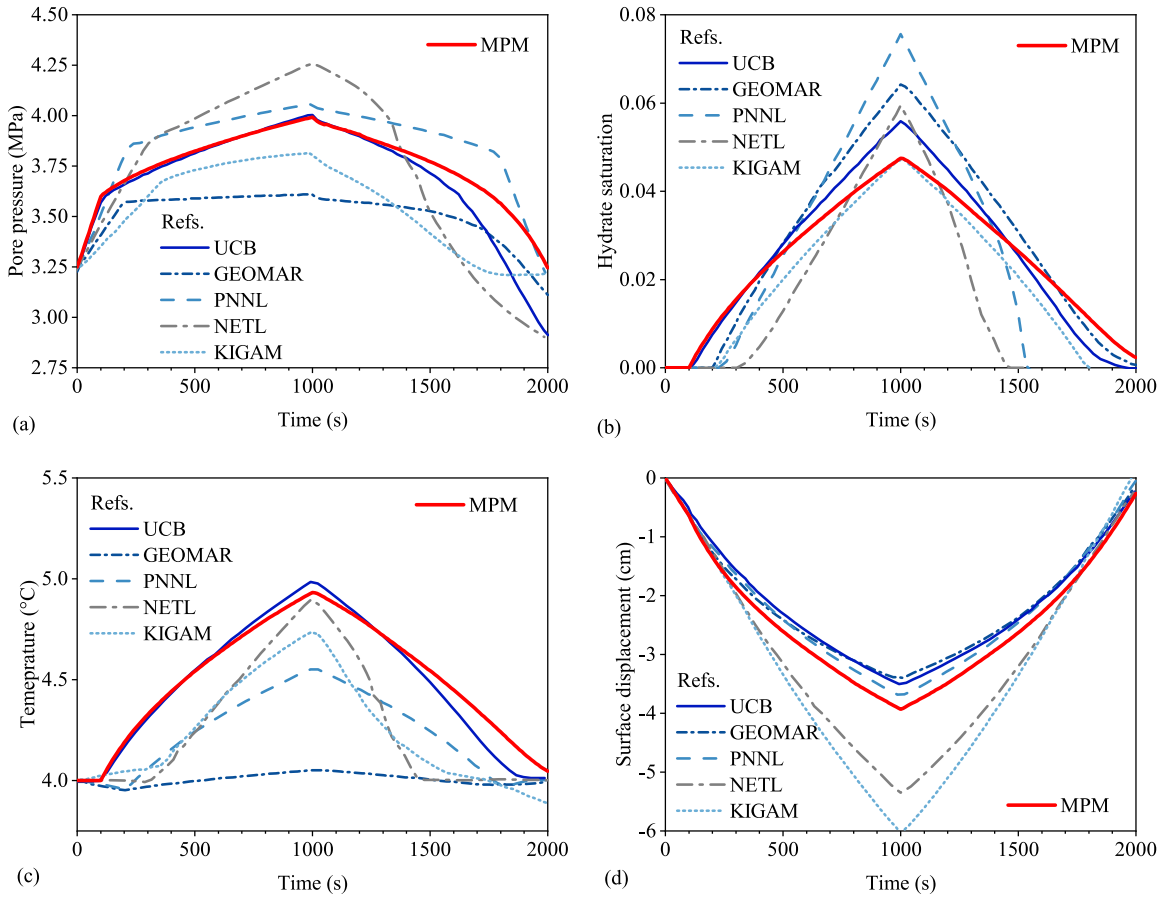

Fig. 10. Case 2 (hydrate kinetics enabled): evolution of (a) pore pressure, (c) hydrate saturation, (d) temperature at $x = 0.6$ m, and (b) surface displacement.

the Unloading stage (t = 1000–2000 s): dissipation of excess pore pressure triggers hydrate dissociation; as a result, temperature and displacement recover gradually to their initial states. It is worth noting that hydrate formation enhances the stiffness of the soil matrix, resulting in reduced peak displacement during loading compared to Case 1.

Fig. 11 illustrates minimal spatial variation in pore pressure, temperature, and hydrate saturation during loading (*e.g.*, t = 500 and 1000 s), underscoring the strong interdependence among these coupled fields. Quantitative comparisons in Fig. 10 reveal similar trends and magnitudes between the predictions of the coupled MPM framework and the reference codes. Notably, the MPM results exhibit particularly good agreement with the predictions from the UCB model. This is potentially attributed to the use of the same hydrate kinetic reaction model as employed in the UCB study, whereas other reference codes adopt alternative kinetic models, as evidenced by differences in the initiation time of hydrate dissociation. These findings confirm that the developed MPM framework effectively resolves the complex coupling of hydrate phase transition, fluid flow, heat transfer, and mechanical deformation. Minor deviations observed between the MPM and other predictions are likely due to inherent differences in the constitutive models and numerical schemes employed by each code.

5. Modeling coupled phase transition and large deformation in MHBS

This section presents two numerical examples to investigate the bidirectional coupling between hydrate dissociation and large deformation in MHBS. The first example simulates the biaxial compression test on MHBS columns, aiming to demonstrate how shear deformation initiates hydrate dissociation and affects the subsequent THMC responses. The second example simulates progressive failures in hydrate-bearing slopes, aiming to explore how the hydrate dissociation process triggers slope instability and influences the landslide dynamics.

5.1. Biaxial compression test on MHBS specimen

The biaxial compression test serves as a widely adopted numerical example for investigating localized responses in granular materials (Sun, 2015; Na and Sun, 2017; Liang and Zhao, 2019; Zhao et al., 2020). In this study, the test is applied to an MHBS

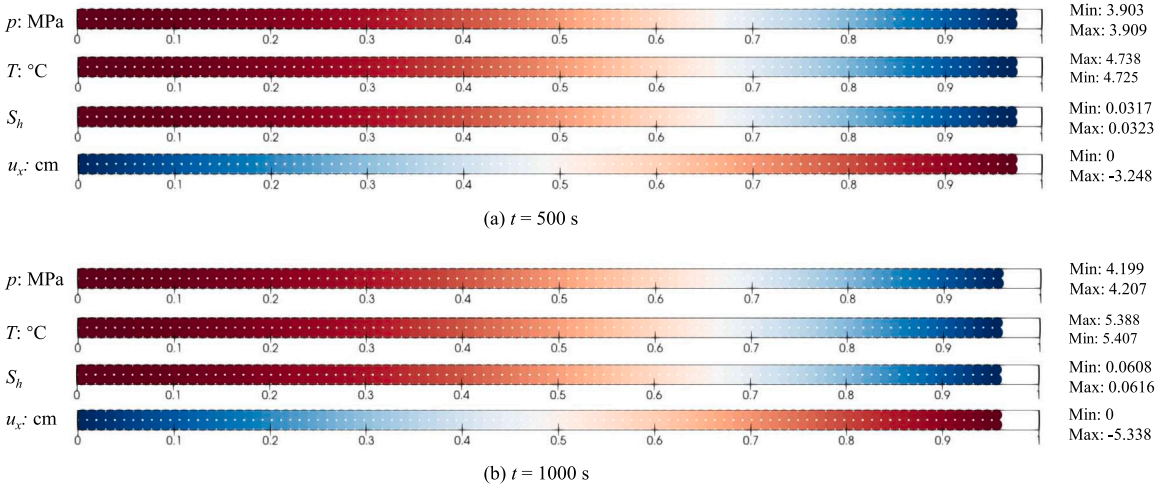

Fig. 11. Case 2: contour results for pore pressure (p), temperature (T), hydrate saturation (S_h), and axial displacement (u_x) at the time instances of (a) 500 s and (b) 1000 s.

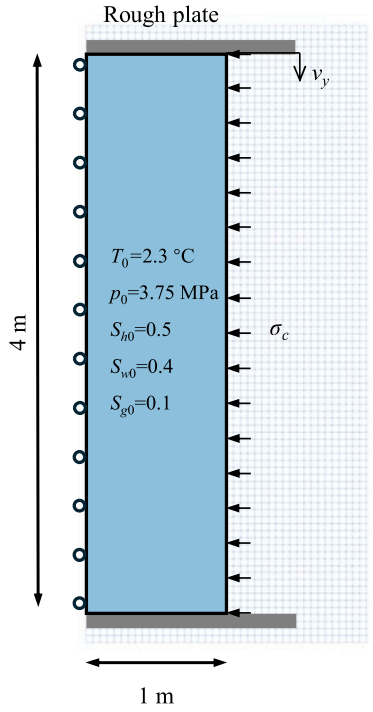

Fig. 12. Model setup for the biaxial compression test on an MHBS column.

sample with dimensions of 4 m × 2 m. Rough, rigid plates are attached to the top and bottom boundaries, with their movement constrained in the x-direction. The top plate is subjected to a rapid downward loading at a constant velocity of $v_y = 0.1$ m/s, while the bottom plate remains fixed. To minimize stress oscillations during loading, the velocity is linearly ramped from zero to the prescribed magnitude within the first 0.1 s (Liang and Zhao, 2019). Due to geometric symmetry, only the right half of the domain is modeled. The left symmetric boundary is impermeable, adiabatic, and fixed in the horizontal direction. The model setup, along with the initial conditions, is illustrated in Fig. 12.

The material parameters follows Masuda's example in Section 4.1, with the following modifications: Young's modulus E = 600 MPa, Poisson's ratio $\nu = 0.33$, intrinsic permeability $k_0 = 1 \times 10^{-14}$ m^2, kinetic reaction rate $K_0 = 3.6 \times 10^5$ mol/(m^2 Pa s), and strength parameters c_{max} = 1000 kPa, $c_{min} = c_{res}$ = 100 kPa, φ_{max} = 45°, φ_{res} = 30°, ψ_{max} = 15°, ψ_{min} = 5°, and $\eta_s = \eta_h = 5$. The elastic and strength parameters utilized are chosen from experimental data on hydrate samples documented in the literature (Soga

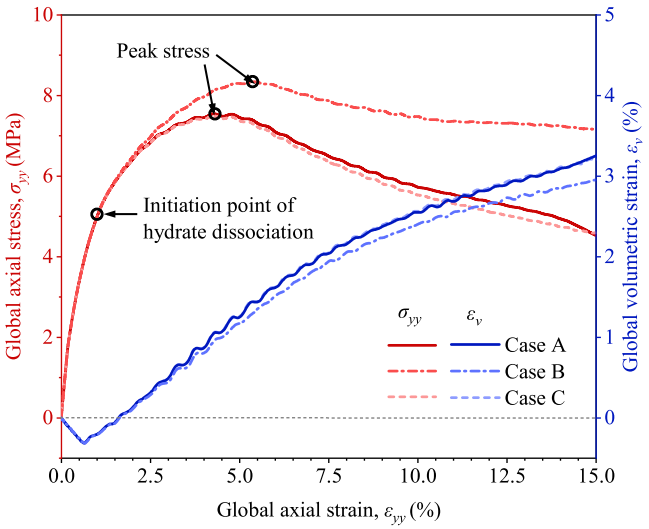

Fig. 13. Global stress–strain relationships from biaxial compression tests on MHBS samples.

et al., 2006; Waite et al., 2009). The computational domain is discretized into quadrilateral cells of 0.05 m size, with four material points in each cell. The time step size is set as 5×10^{-5} s. The simulation is terminated when the global axial strain (ε_{yy}) reaches 15%. Three cases are analyzed:

- Case A: Hydrate dissociation enabled;
- Case B: Hydrate dissociation disabled ($K_0 = 0$);
- Case C: Hydrate dissociation enabled, and plastic heat generation included.

In both Case A and Case B, plastic heat generation is neglected by setting $\theta = 0$. In Case C, the plastic work is assumed to be perfectly converted into heat by setting $\theta = 1$. The mesh sensitivity test indicates that, while a finer mesh may result in thinner shear bands, the mesh currently adopted produces results comparable to those obtained with a finer mesh. Further details regarding the mesh sensitivity test can be found in Appendix B.

Fig. 13 illustrates the global stress–strain relationships for the three cases. The global axial stress σ_{yy} equals the normal reaction force acting on the top plate normalized by the contact area. The global volumetric strain is calculated as the total volume change of all material points divided by the initial volume of the column. We first take Case A as an example for discussion. In this case, σ_{yy} initially increases at a diminishing rate until reaching a peak stress at an axial strain of approximately $\varepsilon_{yy} \approx 5\%$, after which it gradually declines, indicating a softening behavior. The global volumetric strain shows an overall dilative response, with a minor contraction observed during the initial phase. These stress–strain characteristics align with the typical mechanical behavior of high-saturation MHBS samples as documented in the literature (Soga et al., 2006; Waite et al., 2009).

5.1.1. Shear dilation-induced hydrate dissociation

Fig. 14 shows the distribution of deviatoric strain ε_d, volumetric strain ε_v, and porosity ϕ at the final loading stage ($\varepsilon_{yy} = 15\%$). Notable strain localizations characterized by two intersecting shear bands (corresponding to the right segment of a cross-shaped shear band in a full-domain simulation) can be observed in the deviatoric strain contour. Within the shear band, significant volume expansion occurs due to shear dilation, resulting in increased porosity. Under undrained conditions, this volumetric dilation tendency can lead to a rapid buildup of negative excess pore pressure, which may subsequently trigger hydrate dissociation. These phenomena are successfully captured in our simulation and corroborated in laboratory triaxial tests by Yan et al. (2023).

Additionally, we observe that the inclination angle of the shear band with respect to the horizontal direction is approximately 51°. This value is lower than the Coulomb's angle ($\theta_C = 45° + \varphi/2 = 60° \sim 67.5°$), close to the Roscoe's angle ($\theta_R = 45° + \psi/2 = 47.5° \sim 52.5°$), and slightly lower than the Arthur's angle ($\theta_A = 45° + (\varphi + \psi)/4 = 53.75° \sim 60.0°$). Many experimental and theoretical studies suggest that the shear band angles falling within the range between θ_C and θ_R are all reasonable. Readers may refer to Appendix C for more discussion.

Fig. 15 further shows the distribution of excess pore pressure $p = (\chi_w p_w + \chi_g p_g)$ and hydrate saturation S_h for both Cases A and B at $\varepsilon_{yy} = 15\%$. Additionally, Fig. 16 further plots the local responses of deviatoric stress q, volumetric strain ε_v, excess pore pressure, and hydrate saturation at point M - a point located at the center of the upper wing of the shear band. The contour of excess pore pressure reveals a significant pressure drop within the shear band, and concurrently, the hydration saturation contour shows a noticeable reduction in S_h, likely due to hydrate dissociation. Interestingly, in Case B – where hydrate dissociation is not considered – a reduction in S_h is still observed within the shear band. This phenomenon occurs because hydrate saturation evolves

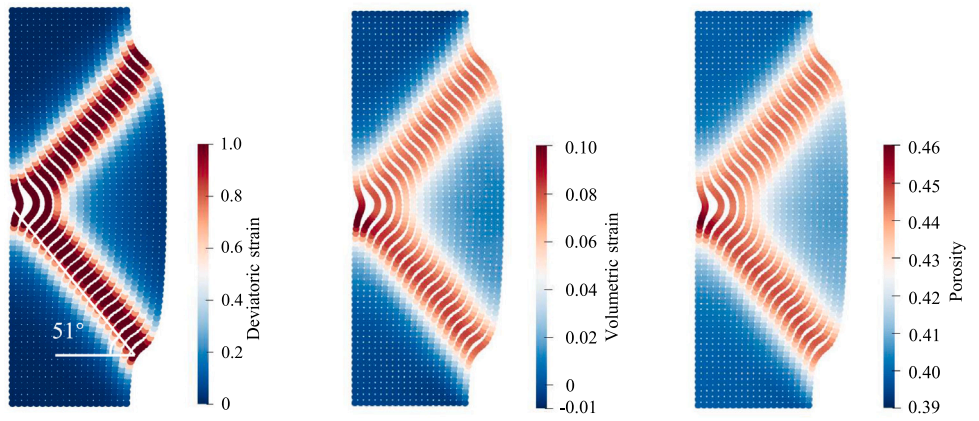

Fig. 14. Simulation results for Case A: distributions of deviatoric strain ϵ_d, volumetric strain ϵ_v, and porosity ϕ at a global axial strain of 15%.

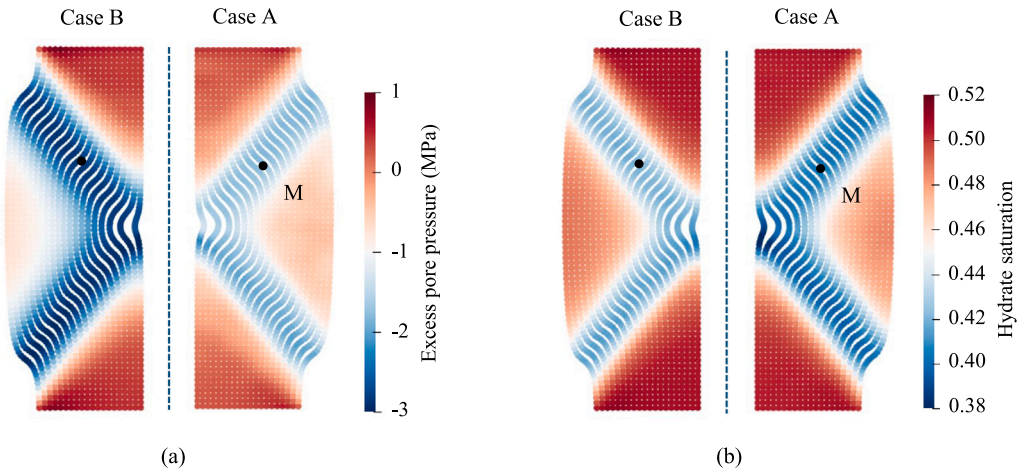

Fig. 15. Comparison of simulation results for Case A and Case B: contours of (a) excess pore pressure and (b) hydrate saturation at $\epsilon_{yy} = 15\%$.

not only through hydrate phase changes but also with variations in porosity ϕ, as indicated by Eq. (20). Since Case B excludes hydrate phase changes, the observed decrease in S_h is entirely attributed to changes in porosity. In contrast, Case A demonstrates a much lower S_h than Case B, indicating the additional effect of hydrate dissociation on S_h reduction. To better quantify the extent of hydrate dissociation, the percentage of hydrate mass change, denoted as δm_h, is utilized. It is defined as the hydrate mass change Δm_h divided by the initial hydrate mass m_{h0} at each material point. As shown in Fig. 16(d), S_h at point M in Case B decreases gradually, yet δm_h remains zero, confirming the absence of hydrate dissociation. In contrast, Case A exhibits a clear reduction in δm_h, indicating active hydrate dissociation.

A detailed comparison of the local responses at point M between Case A and Case B reveals that: (1) Case A exhibits a lower peak stress and a more pronounced reduction in post-peak stress compared to Case B, underscoring the additional softening effect caused by hydrate dissociation; (2) the magnitude of negative excess pore pressure in Case A is lower than that in Case B, suggesting that gas and water production during dissociation mitigates the pressure drop. The global stress–strain behavior depicted in Fig. 13 further corroborates observation (1). These findings emphasize that shear dilation in the MHBS system induces hydrate dissociation, which in turn causes mechanical degradation and affects other THMC responses.

It is worth noting that the stress and pressure fields presented in Fig. 16 exhibit slight temporal oscillations. These oscillations can be attributed to dynamic effects resulting from the rapid loading process. Additionally, while the adopted uGIMP shape function mitigates cross-cell noise to some extent, this issue may still persist when particles frequently cross cell boundaries during the biaxial compression. Nonetheless, the amplitudes of these oscillations remain within a controllable and acceptable range.

5.1.2. Shear heating-induced hydrate dissociation

Large shear deformation results in plastic heat generation, a process known as shear heating, which can lead to temperature rise within the shear band region (Kelemen and Hirth, 2007). Rapid shear can cause a sudden increase in temperature, which may prompt hydrate dissociation. Fig. 17 compares the distributions of temperature and percentage of hydrate mass change (δm_h) between Case

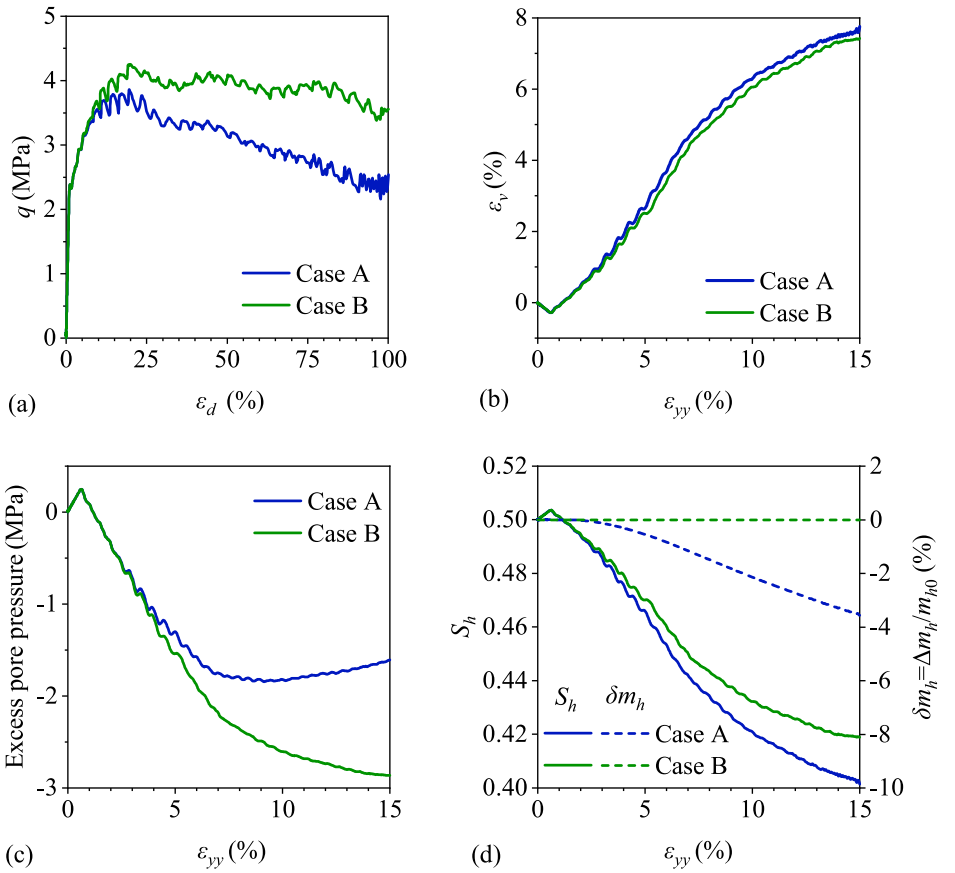

Fig. 16. Comparison of simulation results for Case A and Case B: evolution of (a) deviatoric stress q, (b) volumetric strain ε_v, (c) excess pore pressure $p(= \chi_w p_w + \chi_g p_g)$, and (d) hydrate saturation S_h and percentage of hydrate mass change $\delta m_h (= \Delta m_h / m_{h0})$ at point M.

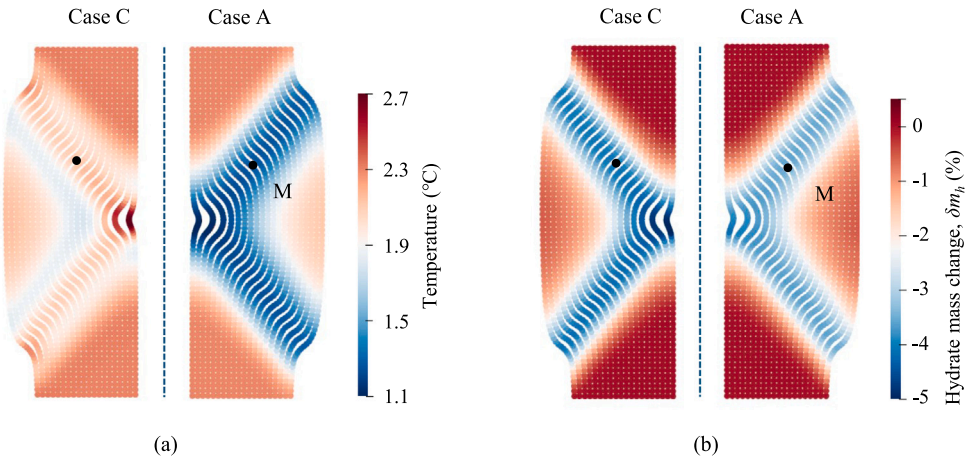

Fig. 17. Comparison of simulation results for Case A and Case C: contours of (a) temperature and (b) percentage of hydrate mass change (δm_h) at $\varepsilon_{yy} = 15\%$.

A and Case C at the final loading stage. Additionally, Fig. 18 presents the local responses at point M for both cases, including shear stress, excess pore pressure, δm_h, and temperature.

Fig. 17(a) shows that, in Case A, where plastic heat generation is neglected, the temperature within the shear band decreases due to the endothermic process of hydrate dissociation. Conversely, when it is included in Case C, the contour result reveals a higher

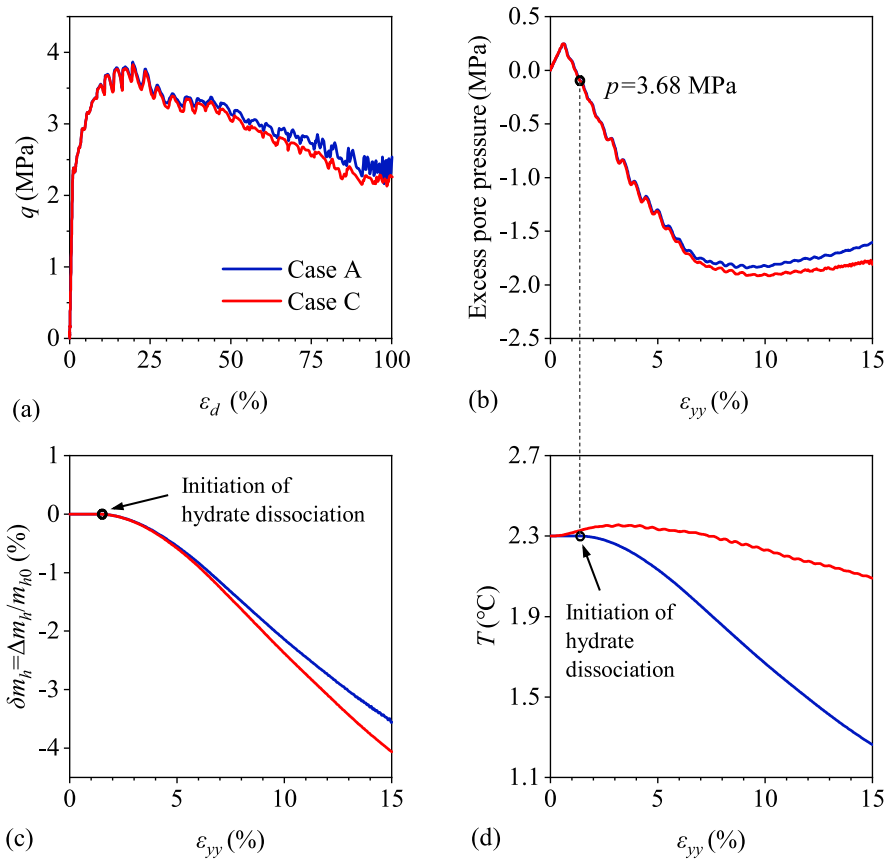

Fig. 18. Comparison of simulation results for Case A and Case C: evolution of (a) deviatoric stress q, (b) excess pore pressure p, (c) percentage of hydrate mass change δm_h, and (d) temperature at point M.

temperature in regions with large shear strain compared to those with relatively low shear strain. Fig. 18(d) further illustrates that at point M in Case C, the temperature rises first before decreasing, with overall values much higher than those observed in Case A. Moreover, Figs. 17(b) and 18(c) indicate that shear heating accelerates the hydrate dissociation process. Consequently, the excess pore pressure in Case C exhibits a slower recovery rate from its minimum value, as shown in Fig. 18(b), and a faster rate of post-peak stress softening, as shown in Fig. 18(a). These findings emphasize the crucial role of shear-induced plastic heat in promoting hydrate dissociation and influencing the subsequent hydraulic and mechanical responses.

5.2. Submarine landslides triggered by hydrate dissociation

Submarine landslides near continental shelves are widely reported to be closely related to hydrate dissociation (Hampton et al., 1996; Elger et al., 2018; Gales et al., 2023; Zhang et al., 2021; Jyothsna and Satyavani, 2024; Wan et al., 2016). Hydrate dissociation can be initiated by both natural and anthropogenic factors. Pressure reductions, resulting from sea level fluctuations such as tidal variations or glacial-interglacial cycles, as well as artificial depressurization, can destabilize hydrate-bearing sediments (Hampton et al., 1996; Gatter et al., 2021). Similarly, temperature increases due to submarine geothermal flow or oceanic warming can also alter hydrate stability conditions, leading to dissociation (Reagan and Moridis, 2007). These processes weaken hydrate-cemented sediments, reducing their shear strength and creating weak layers prone to instability, potentially resulting in submarine landslides (Waite et al., 2009; Gatter et al., 2021).

In this section, we employ the coupled THMC MPM to simulate submarine landslides triggered by hydrate dissociation, focusing on the triggering mechanisms and the THMC responses within the system. Unlike previous approaches that impose artificially defined weakened zones (Buss et al., 2019), the presented model naturally simulates the weakening process induced by hydrate dissociation, offering a more physically realistic representation of triggering mechanisms.

We first simulate a small-scale hydrate-bearing slope (Section 5.2.1) to demonstrate the effectiveness of the proposed method in modeling dissociation-triggered submarine landslides. This is followed by two large-scale slope analyses (Sections 5.2.2 and 5.2.3) to investigate retrogressive failure patterns in submarine landslides. Additionally, we conduct comparative analyses to assess the impact of shear heating on landslide dynamics. In this example, the effect of hydrate saturation on soil stiffness is neglected. For

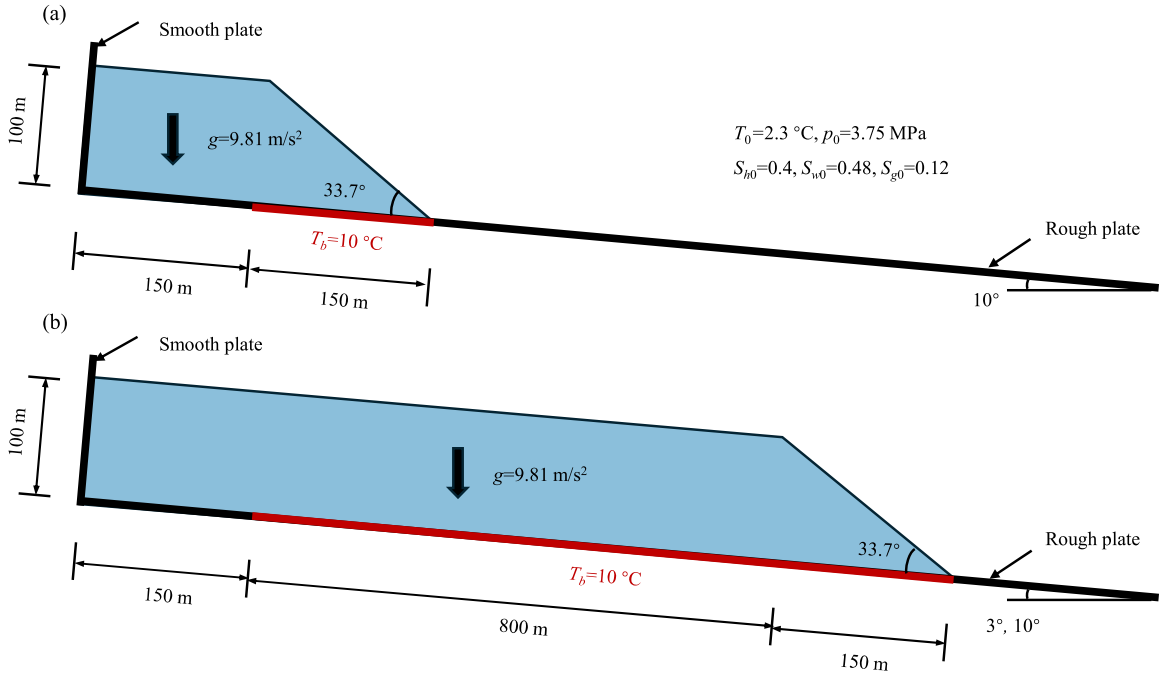

Fig. 19. Model setup for (a) the small-scale test, designed to simulate a single slide failure, and (b) the large-scale tests, aimed at examining retrogressive landslide failures.

simplicity, a section of the bottom of the slope was heated to initiate hydrate dissociation in all cases. It is important to note that the realistic thermal and pressure boundary conditions in natural scenarios are more complex, while the specified temperature boundary condition in this example is an idealized representation.

5.2.1. Scenario A: a small-scale benchmarking test

For the small-scale test, we consider a trapezoid hydrate-bearing slope with a height of 100 m, top and bottom lengths of 150 m and 300 m, respectively, and a slope front angle of approximately 33.7°, as illustrated in Fig. 19(a). To replicate typical submarine geological geometries with slope angles frequently ranging from 0° to 15° (Hampton et al., 1996), the entire soil body is globally inclined by 10°. The initial conditions are specified as follows: $T_0 = 2.3$ °C, $p_0 = 3.75$ MPa, $S_{h0} = 0.4$, $S_{w0} = 0.48$, $S_{g0} = 0.12$, and $\phi_0 = 0.4$. Boundary conditions include a fully fixed, impermeable base, a normally fixed left side, and a free slope-void interface. The material parameters are consistent with those used in Masuda's cone hydrate dissociation example, with additional specifications: Young's modulus $E = 200$ MPa, Poisson's ratio $\nu = 0.33$, intrinsic permeability $k_0 = 1 \times 10^{-14}$ m^2, and kinetic reaction rate $K_0 = 3.6 \times 10^4$ mol/(m^2 Pa s). The strength parameters are given as follows: $c_{\max} = 500$ kPa, $c_{\min} = 100$ kPa, $\varphi_{\max} = 35°$, $\varphi_{\min} = 25°$, $\psi_{\max} = 10°$, $\psi_{\min} = 5°$, and $\eta_s = \eta_h = 5$. The gravitational acceleration is set to $g = 9.81$ m/s^2. To minimize stress oscillations, gravity is linearly increased to the targeted value over the first 10 s. Hydrate dissociation is initiated by applying a constant temperature of 10 °C along the slope base within the range of 150–300 m. The simulation employs uniform quadrilateral cells (4 m × 4 m) for the background mesh, four material points per cell, and a time step size of $\Delta t = 5 \times 10^{-2}$ s.

Global and local responses. Fig. 20 shows the contours of temperature, hydrate saturation, deviatoric strain, volumetric strain, and excess pore pressure at the initiation stage of slope slide ($t = 25$ s) and the final simulation state ($t = 200$ s). At $t = 25$ s, basal heating of the slope triggers hydrate dissociation, leading to soil softening. Under gravitational loading, significant plastic strain accumulates at the slope base, resulting in the formation of a weakened layer and ultimately inducing a V-shaped shear band that spans from the slope base to the ground surface. The V-shaped shear band divides the slope into three distinct sections: the left trapezoid portion remains largely intact, while the upper wedge and the lower-right triangular part slide downward and rightward along the shear band. By $t = 200$ s, the landslide has largely ceased. Within the V-shaped shear band, volumetric dilation, negative excess pore pressure, reduced hydrate saturation, and temperature variations are observed. These phenomena are consistent with those observed in the biaxial compression tests.

To further analyze the initiation of the landslide and the evolution of each physical field in the shear band, we examine two specific points: point A, located at the slope base (150–180 m range), and point B, situated in the middle of the left wing of the V-shaped shear band. Fig. 21 plots the evolution of several key variables at the two points, including temperature, volumetric strain, deviatoric strain, shear stress, excess pore pressure, hydrate saturation, and the rate of hydrate mass change (δm_h). At point A, the temperature rises immediately to approximately 6 °C (Fig. 21(a)), initiating rapid hydrate dissociation (Fig. 21(f)). This leads to a gradual accumulation of shear strain (Fig. 21(b)). However, the gas and water produced from dissociation cause a sharp increase

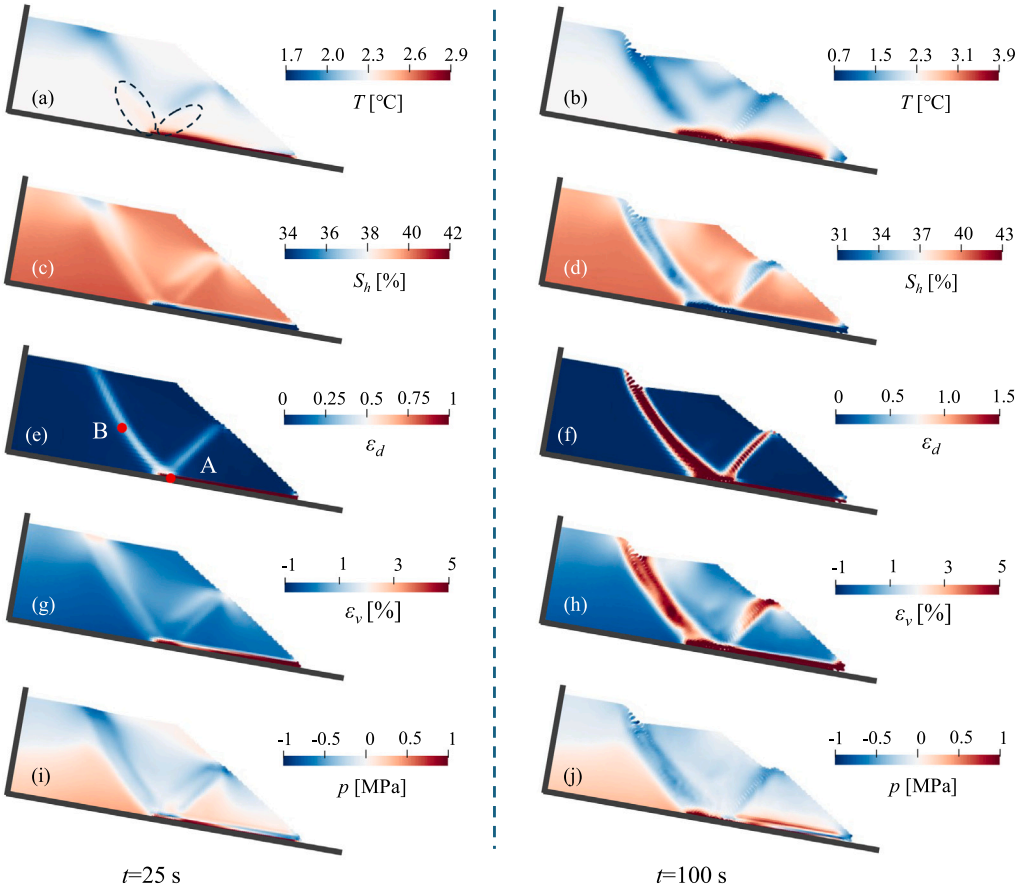

Fig. 20. Contours of key physical fields at the time instances of 25 s and 250 s: (a–b) temperature T, (c–d) hydrate saturation S_h, (e–f) deviatoric strain ε_d, (g–h) volumetric strain ε_v, and (i–j) excess pore pressure p.

in pore water pressure (Fig. 21(e)) and decrease in mean effective stress (Fig. 21(d)), accompanied by an increase in volumetric strain (Fig. 21(c)). At around t = 20 s, the shear strain at point A begins to increase rapidly, corresponding to the formation of the V-shaped shear band, while changes in shear stress and pore water pressure become moderate. Meanwhile, at point B, shear strain and volumetric strain begin to increase, followed by a decrease in shear stress, indicative of softening (Fig. 21(d)). As a result, the pore pressure begins to decrease, and hydrate dissociation is initiated within the shear band. Before the temperature decrease caused by hydrate dissociation, there is a slight increase in temperature at point B caused by shear heating, which can be indicated from the temperature rise in the marked zone by dotted lines in Fig. 20(a). Additionally, at t = 200 s, the physical quantities at both points still exhibit some slight changes, indicating that hydrate dissociation and slope sliding are still ongoing.

Evolution of kinetic energy. Fig. 22 illustrates the evolution of kinetic energy of the slope, E_k, during the slide process. The kinetic energy reflects the dynamic characteristics of the mass movement of the slope, which is calculated as the sum of phase-specific contributions from the mass and velocity of solid, water, and gas phases, expressed as,

$$E_k = \sum_{p=0}^{N_p} E_{kp} = \frac{1}{2} \sum_{p=0}^{N_p} \left((m_{sp} + m_{hp}) \|\boldsymbol{v}_{sp}\|^2 + m_{wp} \|\boldsymbol{v}_{wp}\|^2 + m_{gp} \|\boldsymbol{v}_{gp}\|^2 \right), \tag{82}$$

where N_p is the total number of material points. The contribution of particle rotation to kinetic energy is neglected.

At approximately t = 13 s, the kinetic energy E_k increases sharply and reaches a significant peak at around t = 25 s. At this point, the V-shaped sliding surface has formed, triggering the rapid development of the landslide. By approximately 32 s, E_k decreases to nearly zero, indicating that the sliding has nearly ceased. Shortly thereafter, E_k rises sharply again, reaching a second peak at t = 38 s, followed by another drop to near zero. Subsequently, E_k rises once more, attaining a third peak at 50 s. After this phase, the sliding largely ceases, but by t = 100 s, the fourth noticeable peak in E_k occurs. The displacement fields at each peak, as presented in Fig. 22, show apparent variations in magnitude. However, no distinct new shear bands are observed. This pattern of kinetic energy evolution differs significantly from typical simulation results of common gravity-induced landslides. In gravity-driven landslides, a single slope slide or sliding surface generally yields one peak in kinetic energy. In contrast, retrogressive landslides often exhibit multiple E_k

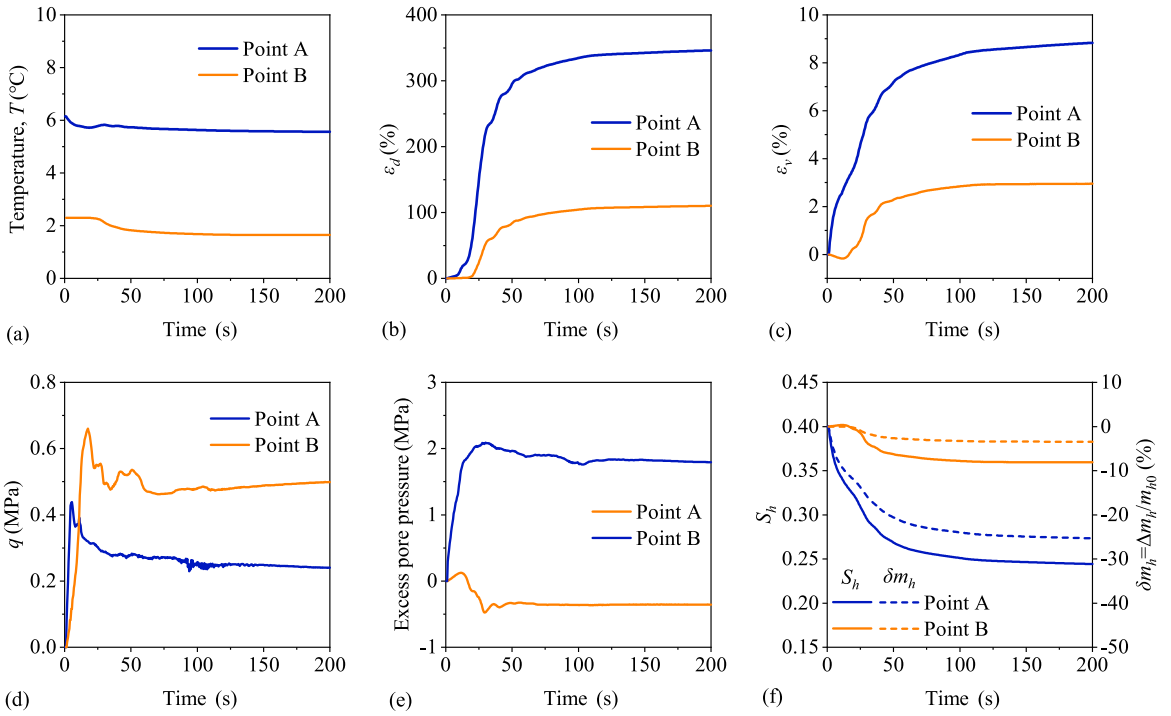

Fig. 21. Local responses of key properties at points A and B: (a) temperature T, (b) deviatoric strain ε_d, (c) volumetric strain ε_v, (d) deviatoric stress q, (e) excess pore pressure p, and (f) hydrate saturation S_h and percentage of hydrate mass change δm_h.

peaks, each corresponding to the formation of a new sliding surface, as demonstrated in prior simulations (Sang et al., 2024; Yu et al., 2024a). In this case, however, the sliding surface is formed only once, yet multiple E_k peaks are observed. This behavior is likely attributed to the continuous dissociation of hydrate, which progressively softens the soil mass. The sustained softening leads to continuous creeping and sudden accelerations of the slope mass. These findings suggest that hydrate dissociation-triggered landslides may exhibit prolonged instability and reactivation over time.

5.2.2. Scenario B: retrogressive landslides in a steep high-strength sediment slope

The submarine landslides are often in retrogressive modes, which means a landslide event is composed of the progressive formation of several slide surfaces (Buss et al., 2019; Dey et al., 2016). To assess retrogressive failure dynamics related to hydrate dissociation, we further simulate a 1100-m-long slope, with a base angle of 10°, as illustrated in Fig. 19(b). The slope is subject to a basal heating ranging from 150 m to 1100 m. The same material properties as the small-scale case are adopted.

Fig. 23 shows the contours of deviatoric strain at different landslide stages. Due to hydrate dissociation, strain accumulation at the slope's base quickly extends to the uppermost part of the heated region by t = 15 s. Merely 3 s later, multiple intersecting V-shaped shear bands emerge in the middle and lower sections of the slope. Notably, the soil masses both upstream and downstream of the shear bands remain largely intact. Simultaneously, strain accumulation occurs at the end of the heated region near the slope crest, with signs of extension toward the slope surface.

Over the next 30 s, the V-shaped shear bands rapidly propagate both upstream and downstream. This leads to the formation of a retrogressive slump complex upstream and lateral spreading failure downstream. Simultaneously, the V-shaped shear band near the slope crest fully develops, forming a pull-apart graben. The slope mass between the graben and the retrogressive slump complex remains largely intact, exhibiting a translational sliding motion. The retrogressive slump complex, lateral spread, translational slide, and pull-apart graben collectively represent typical failure patterns of retrogressive landslides.

By t = 72 s, another secondary shear band emerges within the graben. At t = 250 s, the landslide appears to have ceased progression; however, new plastic zones are observed in the soil downstream of the graben, suggesting that the landslide process might still be ongoing at a slower pace.

Fig. 24 illustrates the evolution of kinetic energy during the landslide process. Similar to the small-scale landslide, a prominent peak is observed, along with several secondary peaks. The first and second secondary peaks occur at t = 45 s and t = 72 s, respectively, corresponding to the formation of the graben at the slope crest and the development of a sub-shear band within the graben. However, the third and fourth secondary peaks cannot be directly associated with the emergence of shear bands. Instead, they are likely caused by the sudden acceleration of slope mass movement due to the continued dissociation of hydrates.

In the simulation discussed, we considered plastic heat generation by setting θ = 0.5. As a comparison, we also simulated the case without considering plastic heat (*i.e.*, θ = 0). Fig. 25 compares the results of both cases at t = 250 s. It is evident that, without

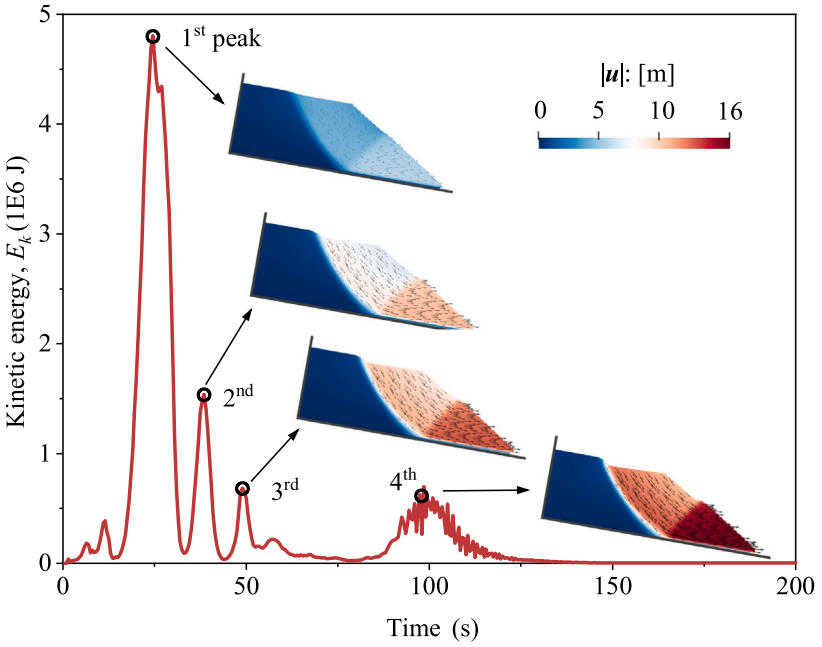

Fig. 22. Evolution of kinetic energy (E_k) for the small-scale slope. The contour figures show the magnitude of displacement at each peak.

considering shear heating, the landslide travels a shorter distance and has a less significant lateral spread. Additionally, the sub-shear band in the graben is not fully developed, resulting in less subsidence. The plastic zone downstream of the graben is also less pronounced, and the displacement of the translational sliding block is apparently smaller. This occurs because heating leads to additional dissociation of hydrates, accelerating the softening of the slope. To clearly demonstrate this, we compared the percentage of overall hydrate mass change within the slope for both cases, as presented in Fig. 26. It shows that, during the landslide's rapid development stage, *i.e.*, between $t = 13$ and 35 s, hydrates dissociate quickly, and the dissociation rate for $\theta = 0.5$ case is noticeably higher than the $\theta = 0$ case. Their gap continues to widen after the major landslide period. These observations suggest that neglecting the effect of shear heating might underestimate the extent of hydrate dissociation and the landslide scale.

5.2.3. Scenario C: retrogressive landslides in a gentle low-strength sediment slope

When hydrates are present in sensitive clay sediments, their dissociation can lead to more significant softening of the sediments, which can trigger more severe retrogressive landslides even if the slope angle is gentle (Laberg and Camerlenghi, 2008; Mountjoy et al., 2014). Building on Case B, we reduce the slope base angle to 3 degrees while keeping other dimensions unchanged. Additionally, we lower the strength parameters to: $c_{max} = 250$ kPa, $c_{min} = 50$ kPa, $\varphi_{max} = 25°$, $\varphi_{min} = 5°$, and reduced the initial hydrate saturation S_{h0} to 0.25 with $S_{w0} = 0.6$ and $S_{g0} = 0.15$. All other parameters remain the same. We simulated both cases with and without considering plastic heat generation. For the former case, we set $\theta = 0.5$.

Fig. 27 shows the changes in shear strain, illustrating the entire progression of the retrogressive landslide. At $t = 17$ s, the first shear band forms near the front of the slope. By $t = 30$ s, the second and third V-shaped shear bands appear simultaneously at the top and middle of the slope, respectively, creating two grabens. At $t = 41$ s, additional sub-shear bands develop within the grabens. Between $t = 56$ and 60 s, the fourth and fifth V-shaped shear bands form almost at the same time. By $t = 77$ s, the final shear band appears downstream of the slope, and by $t = 250$ s, the landslide has largely come to a halt, with a runout distance of 600 m. The shear failure patterns exhibit spatial variability across the slope, which can be explained as follows. The basal softening due to hydrate dissociation causes the downstream portion of the slope to move rapidly toward the free side, while the upstream portion remains laterally constrained. This differential movement results in the formation of tensile grabens in the central part of the slope, which, in turn, leads to the development of conjugate shear bands exhibiting a characteristic "V" shape (*i.e.*, the 2nd, 3rd, 4th, and 5th shear bands). In contrast, near the slope toe, the absence of lateral constraint on the right side promotes shear failure predominantly in the left-inclined direction (*i.e.*, the 1st and 6th shear bands). The formation of multiple grabens and horsts, as marked in Fig. 27, is a characteristic of such kind of retrogressive landslide. Furthermore, the inclination angles of the shear bands with respect to the horizontal direction range from 47° to 51°, closely aligning with the Roscoe angle ($\theta_R = 47.5°$~$50°$) and the Arthur angle ($\theta_A = 47.5°$~$53.75°$). The slight deviations at different locations can be attributed to the progressive softening of the material within the shear bands and the rotation of the principal stress.

Fig. 28(a) shows the changes in kinetic energy (E_k) during the landslide. It exhibits a very high single peak, even higher than the peak observed in the steeper slope in Section 5.2.2. We observe some rate changes in the curve, with notable inflection points likely related to the progressive failure in the retrogressive landslide. To analyze this further, we calculated the derivative

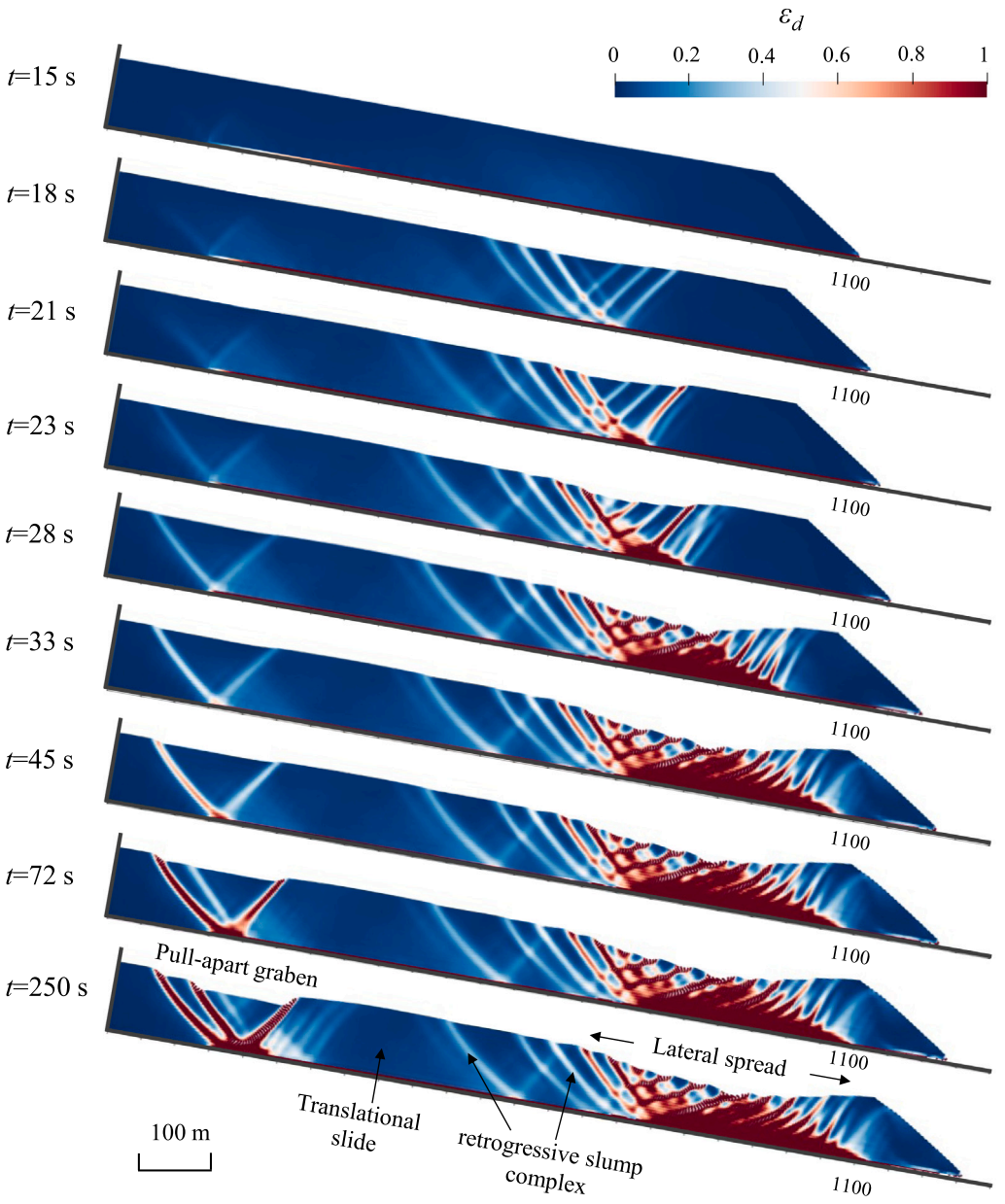

Fig. 23. Contours of deviatoric strain (ε_d) at different time instances for the large-scale slope simulation. The plastic heat generation is included in this test.

of kinetic energy in time: dE_k/dt, namely, the changing rate of kinetic energy (physically representing the power of the slope mass movement), denoted by P_k, as shown in Fig. 28(b). A positive P_k indicates increasing kinetic energy, while a negative P_k indicates the opposite. Changes in P_k reflect the rate at which kinetic energy accumulates and dissipates, with periods of rapid increase or decrease corresponding to swift landslide development.

To delve deeper, we take the second derivative of kinetic energy in time: $dP_k/dt = d^2E_k/dt^2$, denoted by R_k, as depicted in Fig. 28(c). R_k clearly shows several peaks and troughs. If comparing with Fig. 27, it is easy to find that each peak in R_k corresponds to the formation of a (or a set of) shear band, while each trough indicates the end of one slope slide and the beginning of a new shear band's development.

Based on this, we can divide the curve of R_k into five distinct stages: (I) from t = 12 to 22 s, corresponding to the first slope failure, with the shear band fully developed at t = 17 s; (II) from t = 22 to 50 s, covering the second and third twin slope failures, with a peak at t = 30 s, and additional sub-peaks at t = 35, 41, and 45 s related to sub-shear band formations within the grabens; (III) from t = 50 to 66 s, representing the fourth and fifth twin slope failures, with peaks at t = 56 and 60 s corresponding to the

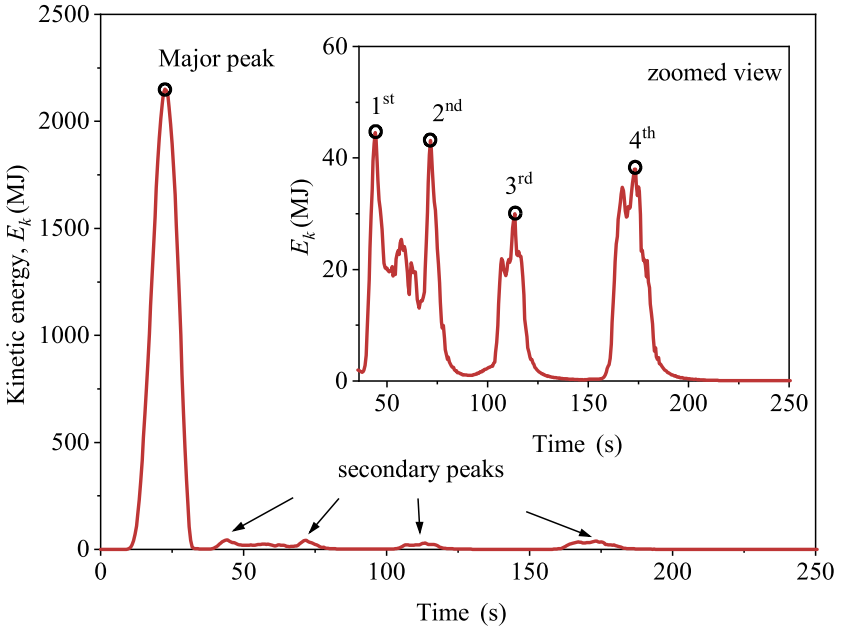

Fig. 24. Evolution of kinetic energy (E_k) for the large-scale slope.

formation of two V-shaped shear bands; (IV) from $t = 66$ to 81 s, associated with the sixth shear band, peaking at $t = 77$ s; (V) the final stage where no new shear bands form, marking the landslide's transition into a creeping stage before halting. Thus, by examining the second derivative of kinetic energy over time, we can effectively segment each stage of retrogressive slope failure and clearly observe the dynamic process of acceleration and deceleration in each stage.

Fig. 29 shows the development of shear bands in the case with plastic heat generation considered. Compared to the case with $\theta = 0$, the key differences are: (1) during the second progressive failure stage, three V-shaped shear bands form simultaneously ($t = 30$ s); (2) also with four main landslide phases, this case ultimately brings about seven major shear bands, while the number for $\theta = 0$ case is six; (3) By the end of the landslide, the slope is more fragmented by the shear bands, and the final slope masses runout distance is greater; and (4) the kinetic energy displays a higher peak and a slower attenuation rate. The progressive development of each landslide, along with the sign of shear band formation, can also be identified from the evolution of R_k (Fig. 30). Compared to the $\theta = 0$ case, the main discrepancies in R_k emerge after $t = 41$ s, characterized by a delayed decreasing rate and a delayed appearance of the trough, indicating the long and enhanced impact of the second-stage triplet shear bands. These observations further emphasize the significant effect of shear heating on the hydrate dissociation-related landslide dynamics.

For illustrative purposes, we also present simulation results of other primary fields at $t = 100$ s, as depicted in Fig. 31. It is easy to find the difference between the $\theta = 0$ and $\theta = 0.5$ cases in the temperature field and other fields within shear bands. As the underlying mechanisms driving these results have been thoroughly analyzed in earlier sections, we will not discuss them in detail here. Collectively, these cases demonstrate that the proposed framework is capable of effectively simulating the bidirectional coupling of hydrate phase transitions and large deformations, along with other critical THMC responses.

6. Conclusions and outlooks

This study presents a thermo-hydro-mechanical–chemical (THMC) coupled material point method (MPM) framework for modeling coupled hydrate phase transition and large deformation in methane hydrate-bearing sediments (MHBS), with particular emphasis on hydrate dissociation-triggered landslides. The mathematical model for MHBS is developed using mixture theory within a single-point multi-phase MPM framework. First, a six-field governing equation is formulated to comprehensively capture dynamic large-deformation characteristics. To close the system, constitutive relationships are introduced, including equations of state for each phase, soil–water retention curves, absolute/relative permeability models, the Kim–Bishnoi hydrate reaction kinetics model, and a skeleton deformation model. Specifically, a hydrate saturation-dependent strain-softening Mohr–Coulomb model is implemented to characterize mechanical strength reduction induced by hydrate dissociation and large strain accumulation. A hybrid explicit–implicit sequential MPM solution scheme is proposed, where drag force terms are treated implicitly to relax permeability-induced time step constraints. Additionally, source terms in mass and energy balance equations are implicitly estimated through a first-order Taylor expansion of primary variables.

The framework is validated through two benchmark problems: Masuda's sandstone core hydrate dissociation experiment and an extended Terzaghi consolidation problem. Numerical results demonstrate the method's capability to accurately reproduce key

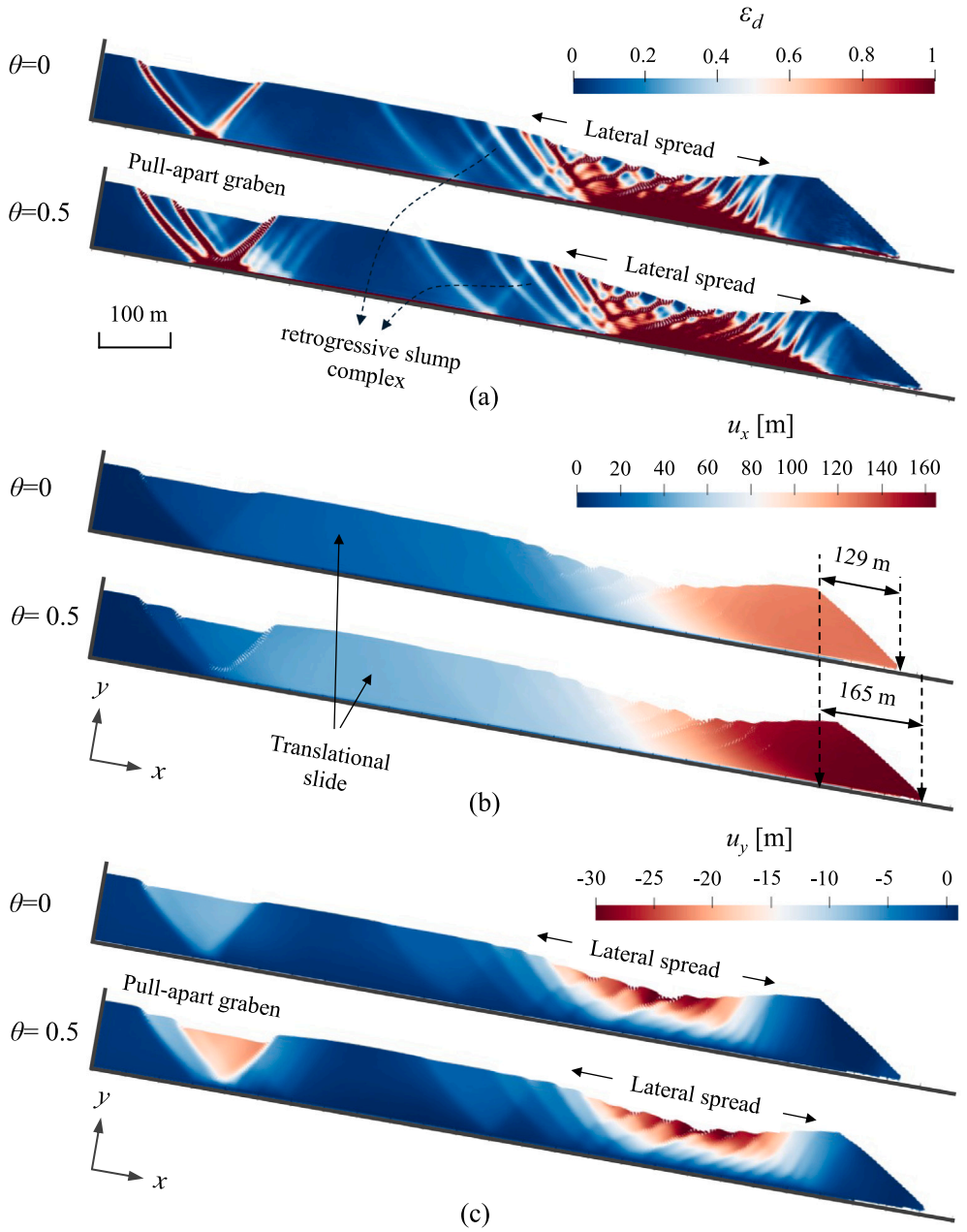

Fig. 25. Effects of shear heating on (a) deviatoric strain (ϵ_d), (b) radial displacement (u_x), and (c) normal displacement (u_y). The contours show the simulation results at $t = 250$ s. Here, $\theta = 0$ represents the case where plastic heat generation is neglected, while $\theta = 0.5$ represents the case where it is considered. The radial displacement refers to the component of the displacement field parallel to the basal plane, whereas the normal displacement refers to the component perpendicular to the basal plane.

THMC responses during both hydrate dissociation and formation processes. Subsequently, the method is applied to simulate the biaxial compression test on hydrate specimens. The simulation results indicate that: (a) shear-induced dilation generates negative pore water pressure, leading to hydrate dissociation; (b) hydrate dissociation further softens the sediments in shear bands, reducing the shear resistance of the specimen; (c) additionally, plastic heat generation due to rapid, large shear deformation accelerates hydrate dissociation and further softening of the sediments. This example demonstrates the proposed method's ability to simulate the bidirectional couplings of large deformations and hydrate dissociation.

Finally, the proposed method is applied to simulate submarine landslides triggered by hydrate dissociation, including a small-scale benchmark test and two large-scale retrogressive landslide tests. We demonstrate that: (a) basal softening and pore pressure

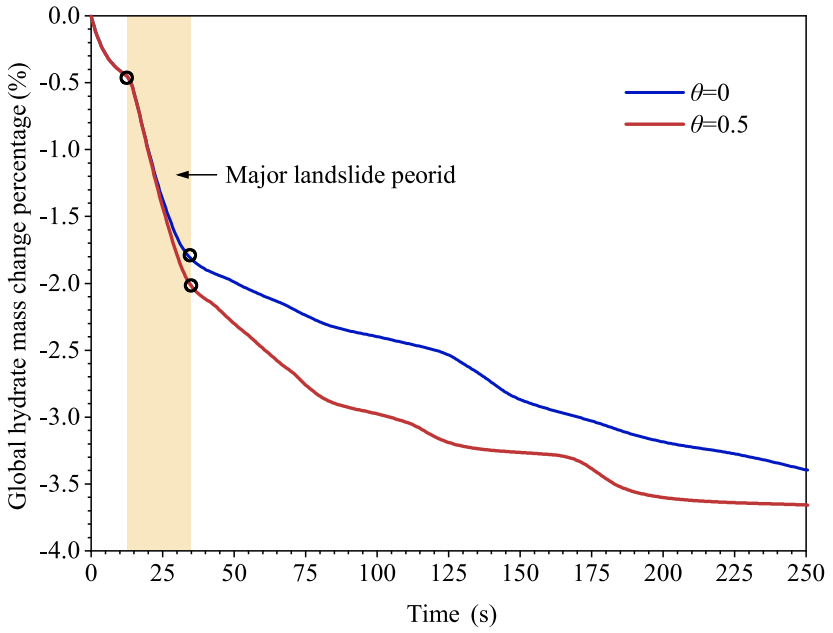

Fig. 26. The percentage of global hydrate mass change within the sediment slope during the progressive landslide: a comparison between the cases considering plastic heat generation ($\theta = 0.5$) and neglecting plastic heat generation ($\theta = 0$).

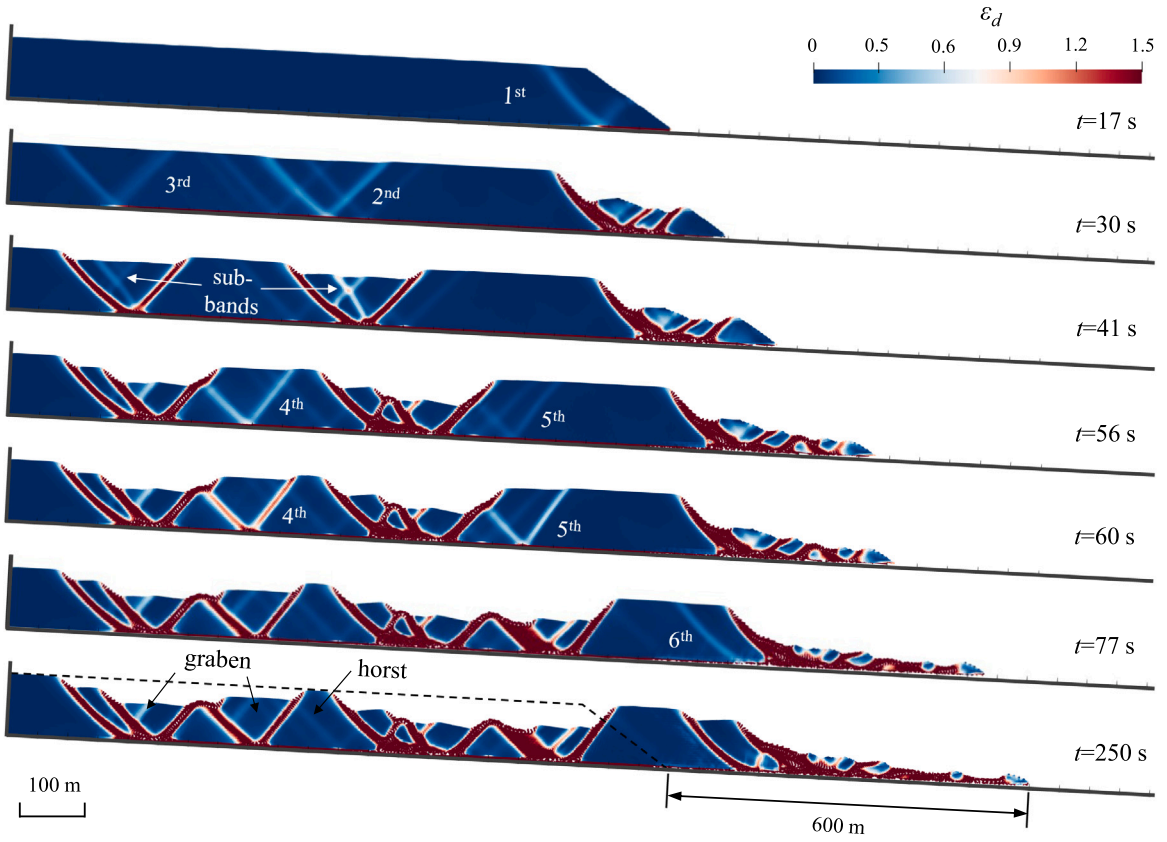

Fig. 27. Contours of deviatoric strain (ε_d) at different time instances for the gentle low-strength slope. The plastic heat generation is not included in this test.

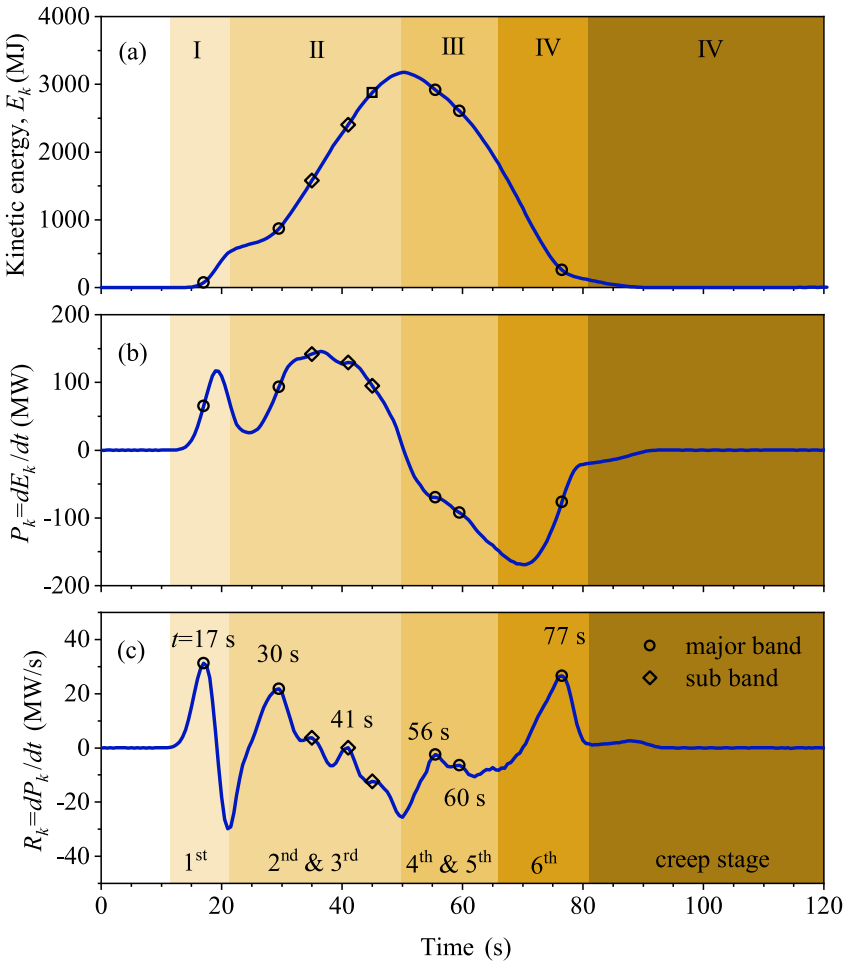

Fig. 28. Evolution of kinetic energy properties for Case B with $\theta = 0$: (a) kinetic energy E_k, (b) first-order derivative of Kinetic energy: $P_k = dE_k/dt$, and (c) second-order derivative of kinetic energy: $R_k = dP_k/dt = d^2E_k/dt^2$.

increases due to hydrate dissociation collectively drive the landslide; (b) ongoing hydrate dissociation can cause sustained creep and reactivation of the landslide after major slope failure events; (c) the progressive formation of retrogressive landslides is closely related to the evolution of slope kinetic energies; (e) plastic heat generation intensifies landslide progression so that its effects should be appropriately considered in the simulation. The proposed method can effectively simulate different retrogressive failure modes. However, different failure patterns are dependent on multiple factors, including strength characteristics of MHBS (related to hydrate saturation, host sediment constituents, and its consolidation history), slope geometries, and environmental conditions. An accurate prediction should be based on careful control of model setups and parameter inputs.

In summary, these tests emphasize the importance of employing fully coupled multiphysical tools to analyze geological failures and hazards related to hydrate dissociation, as even minor changes or the omission of certain factors can significantly impact predictive outcomes. Despite the advancement of the proposed method, we should acknowledge that it does not yet account for several other important factors, such as the critical state behavior of MHBS, the effect of sand erosion, and the interaction of landslide mass movements with surrounding ocean waters, among others. Future research endeavors could be placed on: (a) advanced constitutive modeling, for example, using discrete element method (DEM) for multiscale analysis (Liang et al., 2023; Yu et al., 2024c; Xie et al., 2025); (b) integration of sand production models to address particulate migration during dissociation; (c) development of fully implicit THMC-MPM schemes for long-term simulations; and (d) coupling with fluid solvers (*e.g.*, double-point multiphase MPM) to simulate landslide-generated wave propagation and tsunami dynamics.

CRediT authorship contribution statement

Jidu Yu: Writing – original draft, Visualization, Validation, Software, Methodology, Investigation, Formal analysis, Data curation, Conceptualization. **Jidong Zhao:** Writing – review & editing, Supervision, Resources, Project administration, Methodology,

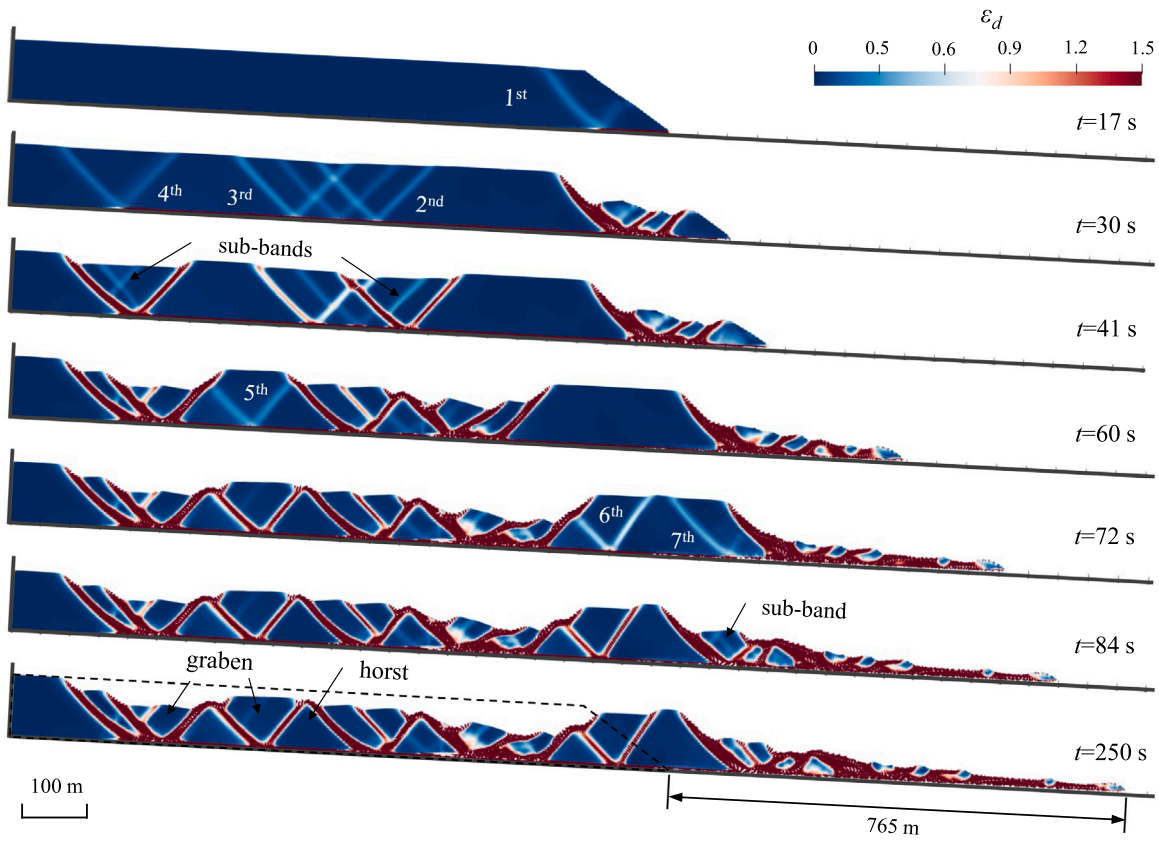

Fig. 29. Contours of deviatoric strain (ε_d) at different time instances for the gentle low-strength slope. The plastic heat generation is included with $\theta = 0.5$.

Investigation, Funding acquisition, Formal analysis, Conceptualization. **Kenichi Soga:** Writing – review & editing, Supervision, Investigation, Formal analysis. **Shiwei Zhao:** Writing – review & editing, Investigation, Methodology, Conceptualization. **Weijian Liang:** Writing – review & editing, Software, Methodology, Formal analysis.

Declaration of competing interest

The authors declare that they have no known competing financial interests or personal relationships that could have appeared to influence the work reported in this paper.

Acknowledgments

The first, second, and fourth authors acknowledge the financial support by the Research Grants Council of Hong Kong (GRF #16212724 and #16206322, RIF #R6008-24, and TRS #T22-607/24N and #T22-606/23R). The authors sincerely thank the reviewers for their constructive feedback and valuable suggestions, which have greatly contributed to enhancing the quality of this manuscript.

Appendix A. Effective stress update

We adopt the return-mapping method to update the effective stress, which consists of an elastic predictor step and a plastic corrector step. In the elastic predictor step, a trial stress is first calculated based on the elastic assumption,

$$\boldsymbol{\sigma}'^{k+1}_{\text{trial}} = \boldsymbol{\sigma}'^{k} + \mathbb{D}^e_{sh} : \Delta\boldsymbol{\varepsilon} + (\Delta\mathbb{D}^e_{sh})(\mathbb{D}^e_{sh})^{-1}(\boldsymbol{\sigma}'^{k} - \boldsymbol{\sigma}'_0). \tag{A.1}$$

Here, the superscripts $k+1$ and k represent the next and the current time step, respectively.

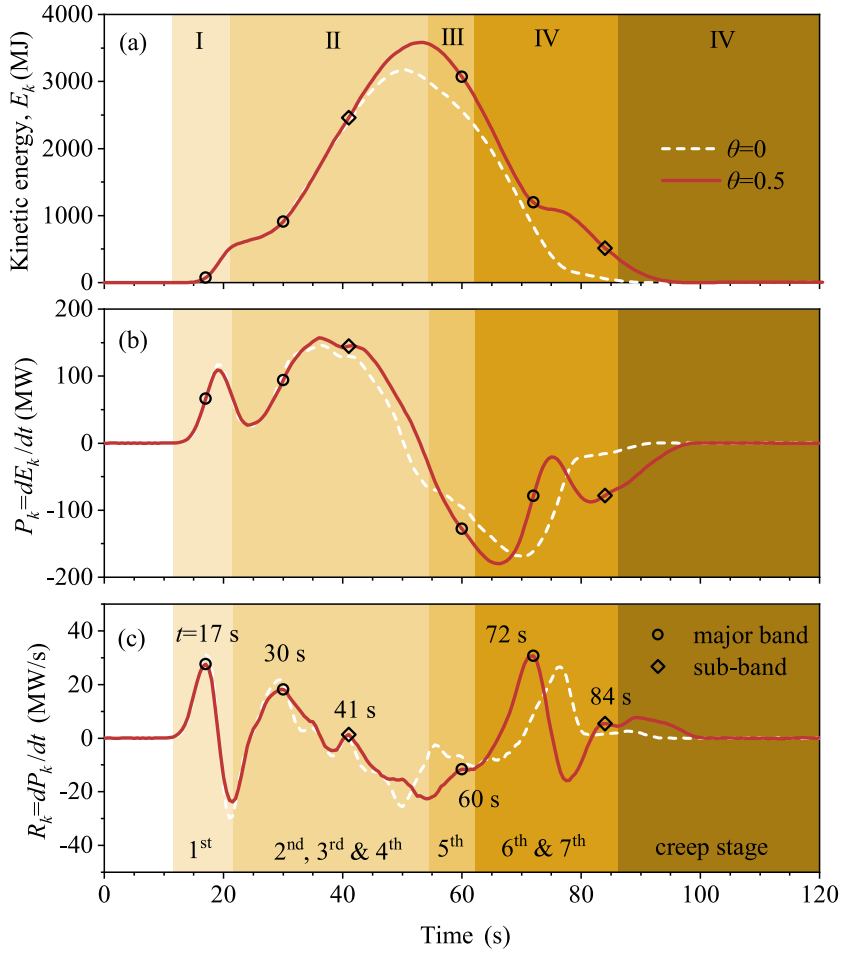

Fig. 30. Evolution of kinetic energy properties for Case B with $\theta = 0.5$: (a) kinetic energy E_k, (b) first-order time derivative of Kinetic energy: $P_k = dE_k/dt$, and (c) second-order time derivative of kinetic energy: $R_k = dP_k/dt = d^2E_k/dt^2$.

If the trial stress does not satisfy the yield criterion $F(\boldsymbol{\sigma}') \geq 0$, the plastic corrector is required to return the trial stress back to the yield surface to ensure $F(\boldsymbol{\sigma}') = 0$,

$$\boldsymbol{\sigma}'^{k+1} = \boldsymbol{\sigma}'^{k+1}_{\text{trial}} - \Delta\boldsymbol{\sigma}'_p, \tag{A.2}$$

where $\Delta\boldsymbol{\sigma}'_p$ is the plastic corrected stress, calculated by,

$$\Delta\boldsymbol{\sigma}'_p = \Delta\lambda\mathbb{D}^e_{sh} : \frac{\partial P}{\partial\boldsymbol{\sigma}'}, \tag{A.3}$$

where $\Delta\lambda$ is the plastic multiplier and P is the potential function.

The trial stress is iteratively adjusted to return back to the yield surface. During each iteration in the plastic corrector,

$$\boldsymbol{\sigma}'^{(n+1)} - \boldsymbol{\sigma}'^{(n)} = -\delta\boldsymbol{\sigma}'^{(n)}_p = -\delta\lambda^{(n)}\mathbb{D}^e_{sh} : \frac{\partial P}{\partial\boldsymbol{\sigma}'^{(n)}}, \tag{A.4}$$

where n is the iteration number. At each iteration, the yield function at the corrected stress state can be linearized as follows (Feng et al., 2024),

$$\begin{aligned} F\left(\boldsymbol{\sigma}'^{(n+1)}, \varepsilon_d^{p(n+1)}, S_h\right) \approx F\left(\boldsymbol{\sigma}'^{(n)}, \varepsilon_d^{p(n)}, S_h\right) + \frac{\partial F}{\partial\boldsymbol{\sigma}'^{(n)}} : \left(\boldsymbol{\sigma}'^{(n+1)} - \boldsymbol{\sigma}'^{(n)}\right) + \\ \frac{\partial F}{\partial\varepsilon_d^p}\left(\varepsilon_d^{p(n+1)} - \varepsilon_d^{p(n)}\right) + \frac{\partial F}{\partial S_h}\left(S_h - S_h\right). \end{aligned} \tag{A.5}$$

Since the hydrate saturation is calculated based on Eq. (80) and no iteration is required for its solution, the hydrate saturation remains constant in the plastic corrector step.

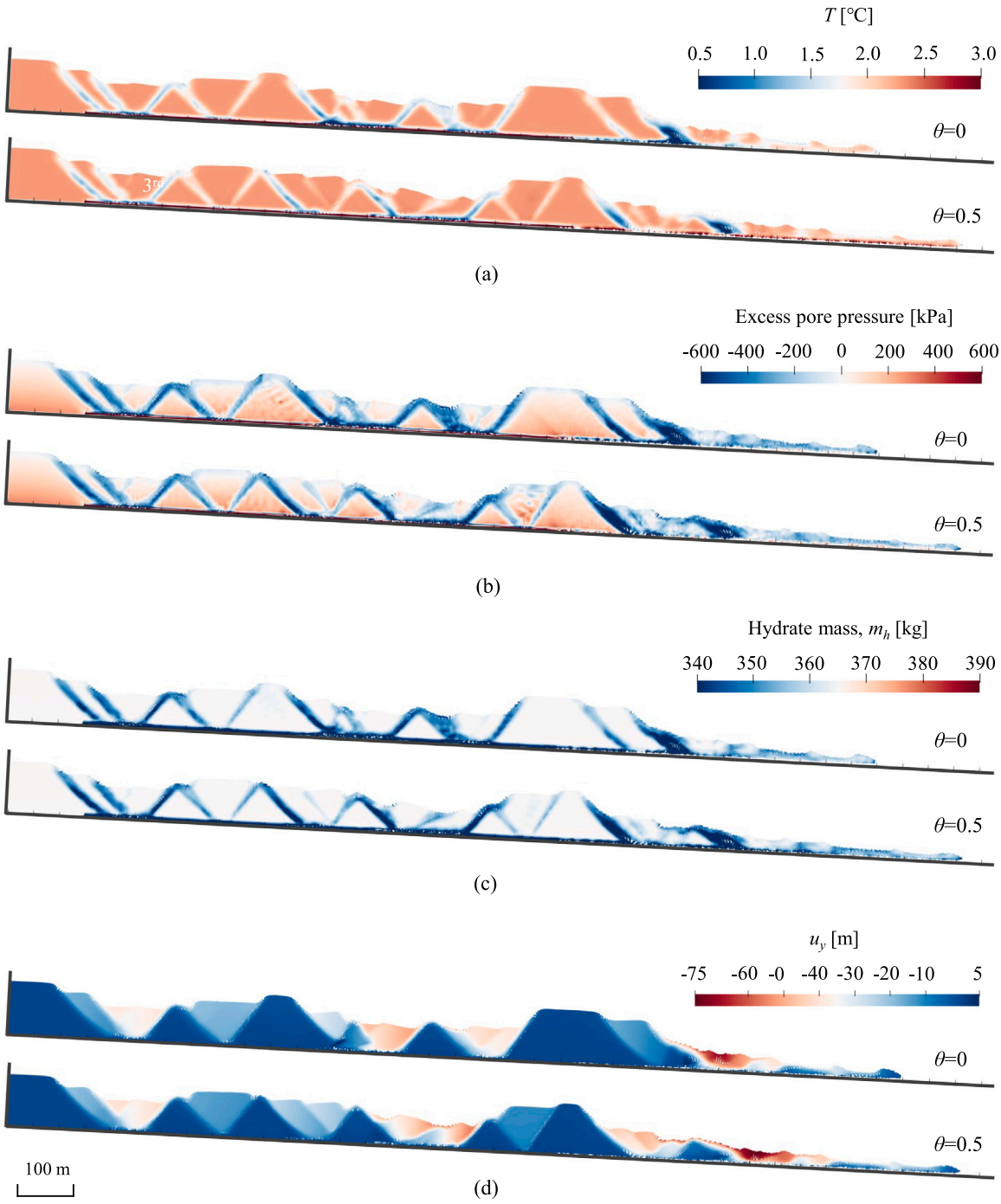

Fig. 31. Simulation results of (a) temperature, (b) excess pore pressure, (c) hydrate mass, and (d) normal displacement to the base plane at $t = 100$ s.

To fulfill the yield condition for the corrected stress state, *i.e.*, $F\left(\boldsymbol{\sigma}'^{(n+1)}, \varepsilon_d^{p(n+1)}, S_h\right) = 0$, and with Eq. (A.4), Eq. (A.5) can be rewritten as,

$$f\left(\boldsymbol{\sigma}'^{(n)}, \varepsilon_d^{p(n)}, S_h\right) - \delta\lambda^{(n)}\left(\frac{\partial F}{\partial \boldsymbol{\sigma}'^{(n)}}\right)^T : \mathbb{D}_{sh}^e : \frac{\partial P}{\partial \boldsymbol{\sigma}'^{(n)}} + \frac{\partial F}{\partial \varepsilon_d^p}\delta\varepsilon_d^{p(n)} = 0. \tag{A.6}$$

Then, the plastic multiplier for the iteration can be obtained as follows,

$$\delta\lambda^{(n)} = \frac{F^{(n)}}{\left(\frac{\partial F}{\partial \boldsymbol{\sigma}'^{(n)}}\right)^T : \mathbb{D}_{sh}^e : \frac{\partial P}{\partial \boldsymbol{\sigma}'^{(n)}} + \left(\frac{\partial F}{\partial \varepsilon_d^p}\right)\sqrt{\frac{2}{3}\frac{\partial P}{\partial \boldsymbol{\sigma}'^{(n)}} : \frac{\partial P}{\partial \boldsymbol{\sigma}'^{(n)}}}}. \tag{A.7}$$

A detailed solution procedure for the effective stress updating is given in algorithm 1.

Algorithm 1 Effective Stress Update Algorithm

Input: $\Delta\boldsymbol{\varepsilon}$, $\Delta\boldsymbol{\omega}$, S_h, $\boldsymbol{\varepsilon}_p^k$, ε_d^{pk}, $\boldsymbol{\sigma}'^k$.

Step 1: Variables initialization
$n = 0$, $\boldsymbol{\sigma}'^{(0)} = \boldsymbol{\sigma}'^k$, $\boldsymbol{\varepsilon}_p^{(0)} = \boldsymbol{\varepsilon}_p^k$, $\varepsilon_d^{p(0)} = \varepsilon_d^{pk}$.

Step 2: Elastic predictor
$\mathbb{D}_{sh}^{e(0)} = \mathbb{D}_{sh}^e(S_h)$, $\Delta\mathbb{D}_{sh}^{e(0)} = \mathbb{D}_{sh}^{e(0)} - \mathbb{D}_{sh}^{e(k)}$.
$\boldsymbol{\sigma}'^{(1)} = \boldsymbol{\sigma}'^{(0)} + \mathbb{D}_{sh}^{e(0)} : \Delta\boldsymbol{\varepsilon} + \boldsymbol{\sigma}'^{(0)} \cdot \Delta\boldsymbol{\omega} - \Delta\boldsymbol{\omega} \cdot \boldsymbol{\sigma}'^{(0)} + (\Delta\mathbb{D}_{sh}^{e(0)})(\mathbb{D}_{sh}^{e(0)})^{-1}(\boldsymbol{\sigma}'^{(0)} - \boldsymbol{\sigma}'_0)$.
$\boldsymbol{\varepsilon}_p^{(1)} = \boldsymbol{\varepsilon}_p^{(0)}$, $\varepsilon_d^{p(1)} = \varepsilon_d^{p(0)}$, $n = n + 1$.
if $f(\boldsymbol{\sigma}'^{(1)}, \varepsilon_d^{p(1)}, S_h) \le 0$ **then**
    Elastic state; Go to **Output**.
else
    Go to **Step 3** (Plastic corrector).
end if

Step 3: Plastic corrector
while $f(\boldsymbol{\sigma}'^{(n)}, \varepsilon_d^{p(n)}, S_h) > \varepsilon_{\text{tol}}$ **and** $n < n_{\max}$ **do**
    Compute plastic multiplier according to Eq. (A.7)
    Compute sub-increments in the iteration:

$$\delta\boldsymbol{\sigma}_p'^{(n)} = \delta\lambda^{(n)}\mathbb{D}_{sh}^{e(0)} : \frac{\partial P}{\partial \boldsymbol{\sigma}'^{(n)}}, \quad \delta\boldsymbol{\varepsilon}_p^{(n)} = (\mathbb{D}_{sh}^{e(0)})^{-1} : \delta\boldsymbol{\sigma}_p'^{(n)}, \quad \delta\varepsilon_d^{p(n)} = \sqrt{\frac{2}{3}\delta\boldsymbol{e}_p^{(n)} : \delta\boldsymbol{e}_p^{(n)}}.$$

    Update stress, plastic strain, and internal variables:

$$\boldsymbol{\sigma}'^{(n+1)} = \boldsymbol{\sigma}'^{(n)} - \delta\boldsymbol{\sigma}_p'^{(n)}, \quad \boldsymbol{\varepsilon}_p^{(n+1)} = \boldsymbol{\varepsilon}_p^{(n)} + \delta\boldsymbol{\varepsilon}_p^{(n)}, \quad \varepsilon_d^{p(n+1)} = \varepsilon_d^{p(n)} + \delta\varepsilon_d^{p(n)}.$$

    $n = n + 1$
end while

Output: $\boldsymbol{\sigma}'^{k+1} = \boldsymbol{\sigma}'^{(n)}$, $\boldsymbol{\varepsilon}_p^{k+1} = \boldsymbol{\varepsilon}_p^{(n)}$, $\varepsilon_d^{p(k+1)} = \varepsilon_d^{p(n)}$.

Appendix B. Mesh sensitivity analysis

We conducted mesh sensitivity analyses for both the biaxial test and landslide simulation to investigate the influence of mesh size (h_e) and the number of particles per cell (ppc) on the simulation results.

For the biaxial test, we considered three different mesh sizes: $h_e = 0.1$ m, 0.067 m, and 0.05 m, with 4 particles per cell ($ppc = 4$) used for each mesh. Additionally, for the $h_e = 0.067$ m case, we also tested a configuration with $ppc = 9$. The deviatoric strain profiles for these four test cases are presented in Fig. B.32. The results show that, for the same ppc, finer meshes result in narrower shear band widths. Increasing the ppc leads to a broader plastic region. However, in general, the shear band shape and inclination angle remain consistent across cases with varying mesh sizes and ppc. Fig. B.33 further compares the evolution of axial stress and global volumetric strain with respect to axial strain. The stress–strain curves, including the peak stress, are largely consistent across all four test cases, with only minor differences observed in the post-peak softening phase. These small discrepancies are likely attributed to the influence of shear band width on hydrate dissociation within the shear band, which affects the degree of softening in the post-failure stage. Based on these observations, we have selected the $h_e = 0.1$ m, $ppc = 4$ mesh for subsequent simulations, as it provides a reasonable balance between computational efficiency and result accuracy.

For the small-scale landslide case, mesh sensitivity was analyzed using $h_e = 4$ m, 3 m, 2 m, with $ppc = 4$ by default. Additionally, for the $h_e = 3$ m mesh, a higher resolution of $ppc = 9$ was tested. The results, as illustrated in Fig. B.34, showed that finer meshes resulted in narrower shear band widths, while higher ppc values led to the development of secondary shear bands. However, the

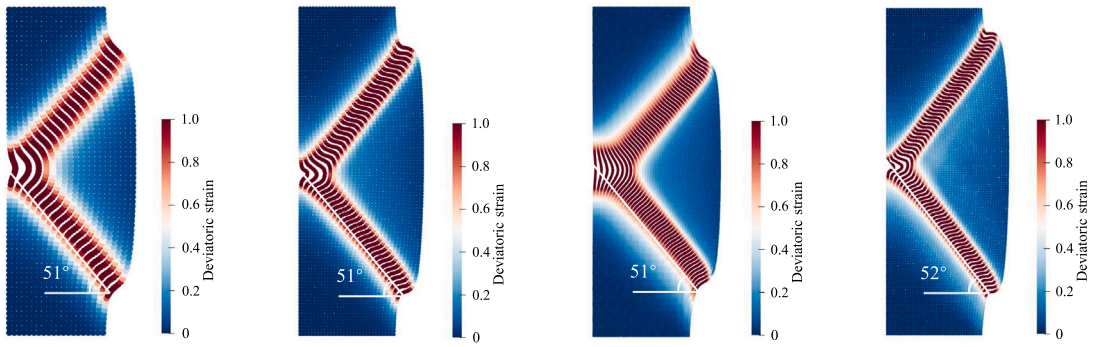

(a) h_e=0.1 m, *ppc*=4 (b) h_e=0.067 m, *ppc*=4 (c) h_e=0.067 m, *ppc*=9 (d) h_e=0.05 m, *ppc*=4

Fig. B.32. Mesh sensitivity analysis for the biaxial compression test: distribution of deviatoric strain at ϵ_{yy} = 15%.

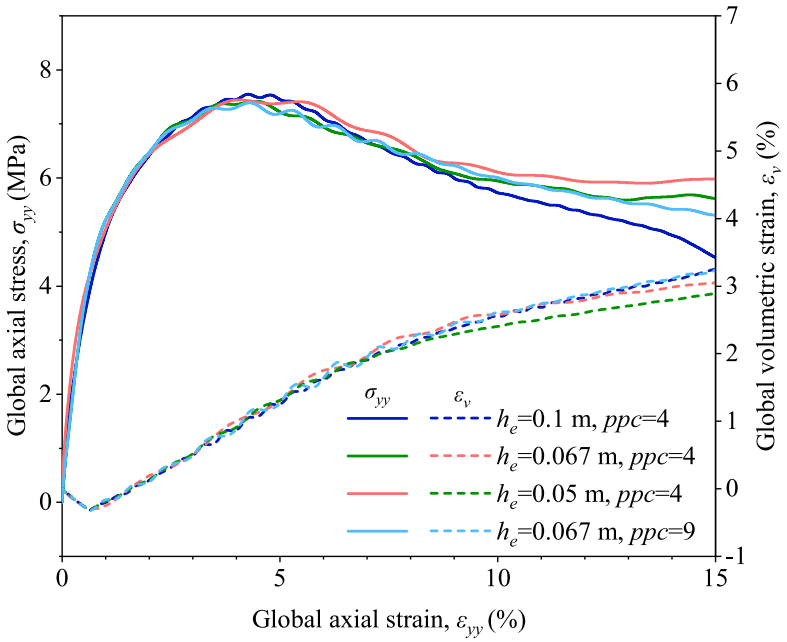

Fig. B.33. Mesh sensitivity analysis for the biaxial compression test: global stress–strain responses with different mesh size h_e and *ppc*.

overall location of the primary shear band remains consistent. For the large-scale landslide case, we tested Scenario A using h_e m and 3 m. The slope failure patterns, as shown in B.35, are generally consistent, but minor differences in the specific locations of the shear bands were observed. Overall, the simulation results demonstrate that mesh size has a greater influence on the results compared to the number of particles per cell. A mesh size of h_e = 4 m was found to provide reasonably accurate results.

Nevertheless, it should be noted that the MPM simulation of shear banding exhibits mesh dependency challenges, particularly for retrogressive landslides with multiple shear bands. Future studies could address this issue by incorporating non-local approaches, which are demonstrated to be capable of mitigating mesh dependency in shear band width and location (Acosta et al., 2024; Haeri and Skonieczny, 2022; Burghardt et al., 2012; de Vaucorbeil et al., 2022). Despite these limitations, the current simulation results do not affect the main conclusions of this study.

Appendix C. Shear band orientation

Experimental evidence and theoretical analyses indicate that the shear band orientation θ falls normally to the bounds by two angles as follows (Vardoulakis, 1980; Vermeer, 1990; Oda and Kazama, 1998; Gao and Zhao, 2013),

$$\theta_R \le \theta \le \theta_C, \tag{C.1}$$

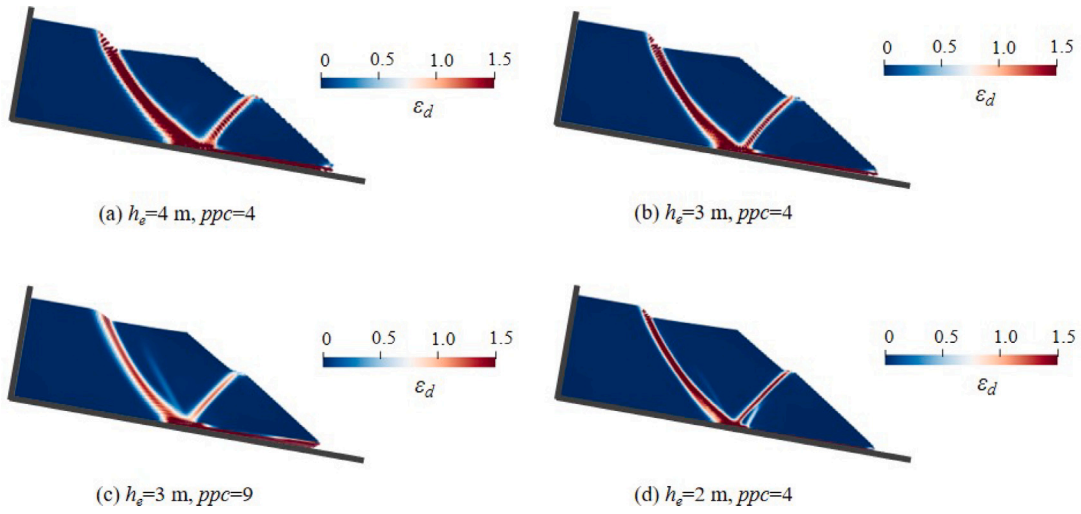

Fig. B.34. Mesh sensitivity analysis for the small-scale landslide test: distribution of deviatoric strain at t = 100 s.

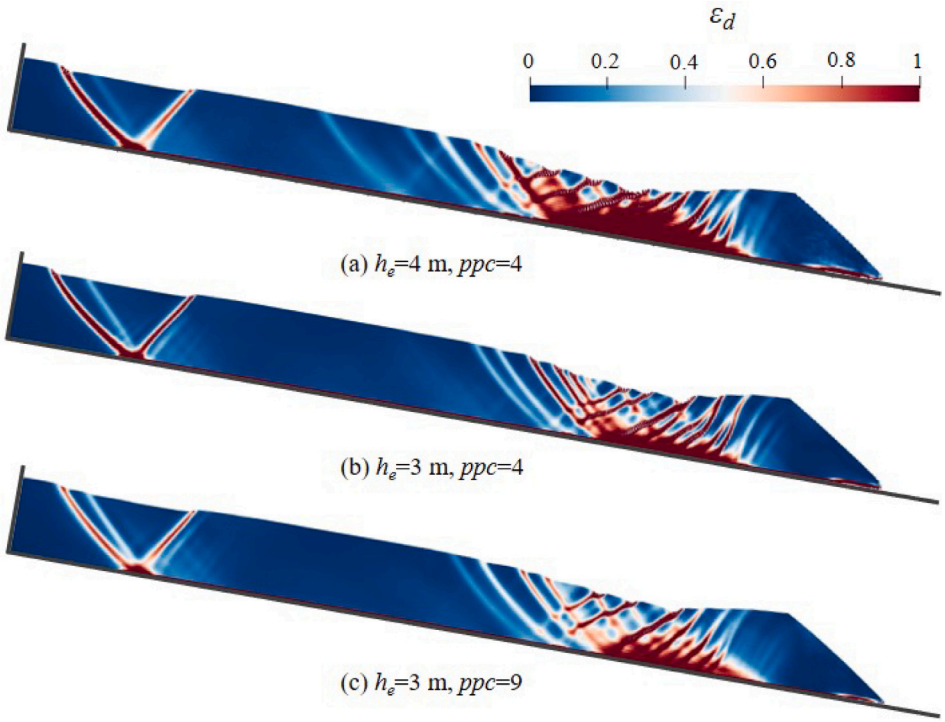

Fig. B.35. Mesh sensitivity analysis for the large-scale landslide test ($\theta = 0$): distribution of deviatoric strain at t = 250 s.

where the lower bound $\theta_R = 45° + \psi/2$ is the Roscoe angle and the upper bound $\theta_C = 45° + \varphi/2$ is the Coulomb angle, and ψ and φ are the dilation angle and friction angle, respectively. For the plane strain compression tests considered here, the physical significance of Roscoe's angle (Roscoe, 1970) is that the shear band develops in the direction where the tensile strain increment is zero, allowing for stable deformation without stress discontinuity or abrupt softening (Vermeer, 1990). Coulomb's angle essentially indicates that the shear band develops along the plane on which the maximum internal friction is mobilized, or where the material reaches its shear strength limit. Based on experimental observations, Arthur et al. (1977) proposed that the shear band orientation $\theta_A = 45° + (\varphi + \psi)/4$, which is between the Roscoe angle and Coulomb angle (denoted as Arthur angle). This relation was later derived by Vardoulakis (1980) based on the bifurcation theory.

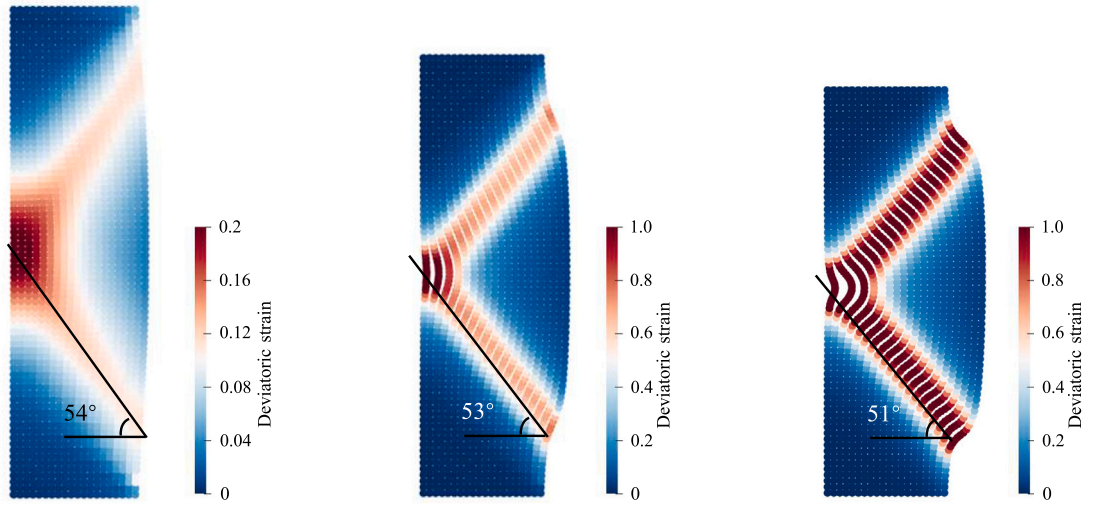

Fig. C.36. Deviatoric strain and approximate shear band orientation at different axial strains.

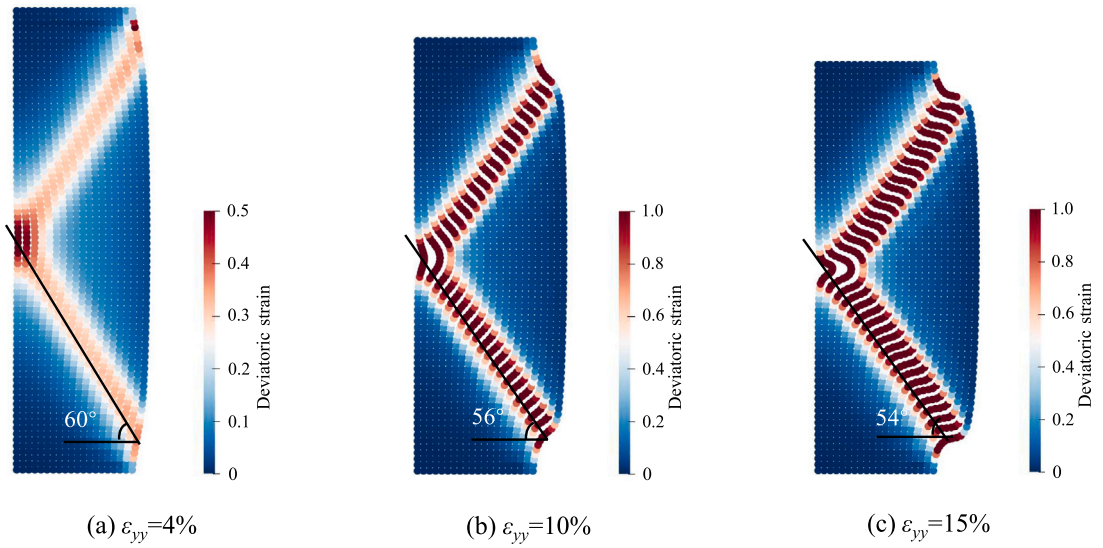

Fig. C.37. Deviatoric strain and approximate shear band orientation at different axial strains given that $\psi = \varphi$.

In the biaxial compression test presented in Section 5.1.1, we set $\varphi_{max} = 45°$, $\varphi_{res} = 30°$, $\psi_{max} = 15°$, $\psi_{min} = 5°$. Correspondingly, the three angles are calculated as follows,

$$\theta_C = 45° + \varphi/2 = 60°\sim67.5°, \tag{C.2}$$

$$\theta_R = 45° + \psi/2 = 47.5°\sim52.5°, \tag{C.3}$$

$$\theta_A = 45° + (\varphi + \psi)/4 = 53.75°\sim60.0°, \tag{C.4}$$

in which the upper limit for each angle represents the peak strength state, and the bottom limit represents the residual strength state.

Fig. C.36 shows the shear band inclination angle for the considered case at different loading states. With the increase in the axial strain, the shear band angle becomes slightly lower. This can be attributed to the strength softening at large strain. The compression of the specimen may also lead to the rotation of the shear band. The inclination angle is approximately 51°~54°, rather close to the upper limit of θ_R and the bottom limit of θ_A. Theoretically, if setting $\psi = \varphi$, we have $\theta_C = \theta_R = \theta_A$ and the shear band angle should fall in this range. To confirm this, we consider a virtual case by setting $\psi_{max} = \varphi_{max} = 45°$, $\psi_{min} = \varphi_{res} = 30°$ (in reality, the dilatancy of MHBS cannot be so large). As can be observed from Fig. C.37, the shear band orientation is approximately 60° at

relatively small strain, equaling the bottom limit of the theoretical value. At large strain, the angle becomes a bit lower, which is potentially attributed to the boundary effect and the rotation of the shear band at large strain. Overall, our simulation can obtain reasonable shear band orientation at given parameters, indicating the reliability of the results.

Data availability

Data will be made available on request.

References

Acosta, J.L.G., Mánica, M.A., Vardon, P.J., Hicks, M.A., Gens, A., 2024. A nonlocal material point method for the simulation of large deformation problems in brittle soils. Comput. Geotech. 172, 106424.

Alvarado, M., Pinyol, N.M., Alonso, E.E., 2019. Landslide motion assessment including rate effects and thermal interactions: Revisiting the Canelles landslide. Can. Geotech. J. 56 (9), 1338–1350. http://dx.doi.org/10.1139/cgj-2018-0779.

Archer, D., 2007. Methane hydrate stability and anthropogenic climate change. Biogeosciences 4 (4), 521–544. http://dx.doi.org/10.5194/bg-4-521-2007.

Arthur, J., Dunstan, T., Al-Ani, Q., Assadi, A., 1977. Plastic deformation and failure in granular media. Géotechnique 27 (1), 53–74.

Bandara, S., Soga, K., 2015. Coupling of soil deformation and pore fluid flow using material point method. Comput. Geotech. 63, 199–214. http://dx.doi.org/10.1016/j.compgeo.2014.09.009.

Bardenhagen, S.G., Kober, E.M., 2004. The generalized interpolation material point method. Comput. Model. Eng. Sci. 5 (6), 477–496.

Baumgarten, A.S., Moreno, J., Kuwik, B., Ghosh, S., Hurley, R., Ramesh, K., 2024. A predictive model for fluid-saturated, brittle granular materials during high-velocity impact events. J. Mech. Phys. Solids 187, 105644.

Boswell, R., Collett, T.S., 2011. Current perspectives on gas hydrate resources. Energy Environ. Sci. 4 (4), 1206–1215. http://dx.doi.org/10.1039/C0EE00203H.

Brooks, R.H., 1965. Hydraulic Properties of Porous Media, Colorado State University.

Burghardt, J., Brannon, R., Guilkey, J., 2012. A nonlocal plasticity formulation for the material point method. Comput. Methods Appl. Mech. Engrg. 225, 55–64.

Buss, C., Friedli, B., Puzrin, A.M., 2019. Kinematic energy balance approach to submarine landslide evolution. Can. Geotech. J. 56 (9), 1351–1365.

Cardoso, S.S.S., Cartwright, J.H.E., 2016. Increased methane emissions from deep osmotic and buoyant convection beneath submarine seeps as climate warms. Nat. Commun. 7 (1), 13266. http://dx.doi.org/10.1038/ncomms13266.

Ceccato, F., Beuth, L., Vermeer, P.A., Simonini, P., 2016. Two-phase material point method applied to the study of cone penetration. Comput. Geotech. 80, 440–452. http://dx.doi.org/10.1016/j.compgeo.2016.03.003.

Chandra, B., Hashimoto, R., Kamrin, K., Soga, K., 2024. Mixed material point method formulation, stabilization, and validation for a unified analysis of free-surface and seepage flow. arXiv:2402.11719.

Chen, P.Y., Chantharayukhonthorn, M., Yue, Y., Grinspun, E., Kamrin, K., 2021. Hybrid discrete-continuum modeling of shear localization in granular media. J. Mech. Phys. Solids 153, 104404.

Chen, L., Yamada, H., Kanda, Y., Lacaille, G., Shoji, E., Okajima, J., Komiya, A., Maruyama, S., 2016. Numerical analysis of core-scale methane hydrate dissociation dynamics and multiphase flow in porous media. Chem. Eng. Sci. 153, 221–235. http://dx.doi.org/10.1016/j.ces.2016.07.035.

Chen, Z.-P., Zhang, X., Sze, K.Y., Kan, L., Qiu, X.-M., 2018. V-p material point method for weakly compressible problems. Comput. & Fluids 176, 170–181. http://dx.doi.org/10.1016/j.compfluid.2018.09.005.

Chong, Z.R., Yang, S.H.B., Babu, P., Linga, P., Li, X.-S., 2016. Review of natural gas hydrates as an energy resource: Prospects and challenges. Appl. Energy 162, 1633–1652. http://dx.doi.org/10.1016/j.apenergy.2014.12.061.

Clarke, M., Bishnoi, P.R., 2000. Determination of the intrinsic rate of ethane gas hydrate decomposition. Chem. Eng. Sci. 55 (21), 4869–4883. http://dx.doi.org/10.1016/S0009-2509(00)00137-8.

Clarke, M., Bishnoi, P.R., 2001a. Determination of the activation energy and intrinsic rate constant of methane gas hydrate decomposition. Can. J. Chem. Eng. 79 (1), 143–147. http://dx.doi.org/10.1002/cjce.5450790122.

Clarke, M.A., Bishnoi, P.R., 2001b. Measuring and modelling the rate of decomposition of gas hydrates formed from mixtures of methane and ethane. Chem. Eng. Sci. 56 (16), 4715–4724. http://dx.doi.org/10.1016/S0009-2509(01)00135-X.

Corey, A., 1954. The interrelation between gas and oil relative permeabilities. Prod. Mon. 38–41.

Davies, R.J., Yang, J., Ireland, M.T., Berndt, C., Maqueda, M.Á.M., Huuse, M., 2024. Long-distance migration and venting of methane from the base of the hydrate stability zone. Nat. Geosci. 17 (1), 32–37. http://dx.doi.org/10.1038/s41561-023-01333-w.

de Vaucorbeil, A., Nguyen, V.P., Mandal, T.K., 2022. Mesh objective simulations of large strain ductile fracture: A new nonlocal Johnson-Cook damage formulation for the total Lagrangian material point method. Comput. Methods Appl. Mech. Engrg. 389, 114388.

Demirbas, A., 2010. Methane hydrates as potential energy resource: Part 1 – Importance, resource and recovery facilities. Energy Convers. Manage. 51 (7), 1547–1561. http://dx.doi.org/10.1016/j.enconman.2010.02.013.

Dey, R., Hawlader, B.C., Phillips, R., Soga, K., 2016. Numerical modelling of submarine landslides with sensitive clay layers. Géotechnique 66 (6), 454–468. http://dx.doi.org/10.1680/jgeot.15.P.111.

Dunatunga, S., Kamrin, K., 2017. Continuum modeling of projectile impact and penetration in dry granular media. J. Mech. Phys. Solids 100, 45–60.

Elger, J., Berndt, C., Rüpke, L., Krastel, S., Gross, F., Geissler, W.H., 2018. Submarine slope failures due to pipe structure formation. Nat. Commun. 9 (1), 715.

Feng, R., Fourtakas, G., Rogers, B.D., Lombardi, D., 2024. A general smoothed particle hydrodynamics (SPH) formulation for coupled liquid flow and solid deformation in porous media. Comput. Methods Appl. Mech. Engrg. 419, 116581.

Feng, K., Wang, G., Huang, D., Jin, F., 2021. Material point method for large-deformation modeling of coseismic landslide and liquefaction-induced dam failure. Soil Dyn. Earthq. Eng. 150, 106907. http://dx.doi.org/10.1016/j.soildyn.2021.106907.

Fredlund, D.G., Xing, A., 1994. Equations for the soil-water characteristic curve. Can. Geotech. J. 31 (4), 521–532.

Galavi, V., Beuth, L., Coelho, B.Z., Tehrani, F.S., Hölscher, P., Van Tol, F., 2017. Numerical simulation of pile installation in saturated sand using material point method. Procedia Eng. 175, 72–79. http://dx.doi.org/10.1016/j.proeng.2017.01.027.

Gales, J.A., McKay, R.M., De Santis, L., Rebesco, M., Laberg, J.S., Shevenell, A.E., Harwood, D., Leckie, R.M., Kulhanek, D.K., King, M., et al., 2023. Climate-controlled submarine landslides on the Antarctic continental margin. Nat. Commun. 14 (1), 2714.

Gallipoli, D., Gens, A., Sharma, R., Vaunat, J., 2003. An elasto-plastic model for unsaturated soil incorporating the effects of suction and degree of saturation on mechanical behaviour. Géotechnique 53 (1), 123–135.

Gao, Z., Zhao, J., 2013. Strain localization and fabric evolution in sand. Int. J. Solids Struct. 50 (22–23), 3634–3648.

Gatter, R., Clare, M.A., Kuhlmann, J., Huhn, K., 2021. Characterisation of weak layers, physical controls on their global distribution and their role in submarine landslide formation. Earth-Sci. Rev. 223, 103845. http://dx.doi.org/10.1016/j.earscirev.2021.103845.

Gaume, J., Gast, T., Teran, J., van Herwijnen, A., Jiang, C., 2018. Dynamic anticrack propagation in snow. Nat. Commun. 9 (1), 3047. http://dx.doi.org/10.1038/s41467-018-05181-w.

Haeri, A., Skonieczny, K., 2022. Three-dimensionsal granular flow continuum modeling via material point method with hyperelastic nonlocal granular fluidity. Comput. Methods Appl. Mech. Engrg. 394, 114904.
Hampton, M.A., Lee, H.J., Locat, J., 1996. Submarine landslides. Rev. Geophys. 34 (1), 33–59.
Hardwick, J.S., Mathias, S.A., 2018. Masuda's sandstone core hydrate dissociation experiment revisited. Chem. Eng. Sci. 175, 98–109. http://dx.doi.org/10.1016/j.ces.2017.09.003.
Hu, Y., Fang, Y., Ge, Z., Qu, Z., Zhu, Y., Pradhana, A., Jiang, C., 2018. A moving least squares material point method with displacement discontinuity and two-way rigid body coupling. ACM Trans. Graph. 37 (4), 150:1–150:14. http://dx.doi.org/10.1145/3197517.3201293.
Hyodo, M., Yoneda, J., Yoshimoto, N., Nakata, Y., 2013. Mechanical and dissociation properties of methane hydrate-bearing sand in deep seabed. Soils Found. 53 (2), 299–314. http://dx.doi.org/10.1016/j.sandf.2013.02.010.
Jiang, M., Zhu, F., Liu, F., Utili, S., 2014. A bond contact model for methane hydrate-bearing sediments with interparticle cementation. Int. J. Numer. Anal. Methods Geomech. 38 (17), 1823–1854.
Jommi, C., 2000. Remarks on the constitutive modelling of unsaturated soils. In: Experimental Evidence and Theoretical Approaches in Unsaturated Soils. CRC Press, pp. 147–162.
Ju, X., Liu, F., Fu, P., White, M.D., Settgast, R.R., Morris, J.P., 2020. Gas production from hot water circulation through hydraulic fractures in methane hydrate-bearing sediments: THC-coupled simulation of production mechanisms. Energy Fuels 34 (4), 4448–4465. http://dx.doi.org/10.1021/acs.energyfuels.0c00241.
Jyothsna, P., Satyavani, N., 2024. Submarine slope failures due to gas hydrate dissociation and degassing along the edge of gas hydrate stability zone in the Krishna Godavari basin. Nat. Hazards 120 (1), 321–338. http://dx.doi.org/10.1007/s11069-023-06213-5.
Ke, W., Svartaas, T.M., Chen, D., 2019. A review of gas hydrate nucleation theories and growth models. J. Nat. Gas Sci. Eng. 61, 169–196.
Kelemen, P.B., Hirth, G., 2007. A periodic shear-heating mechanism for intermediate-depth earthquakes in the mantle. Nat. 446 (7137), 787–790.
Ketzer, M., Praeg, D., Rodrigues, L.F., Augustin, A., Pivel, M.A.G., Rahmati-Abkenar, M., Miller, D.J., Viana, A.R., Cupertino, J.A., 2020. Gas hydrate dissociation linked to contemporary ocean warming in the southern hemisphere. Nat. Commun. 11 (1), 3788. http://dx.doi.org/10.1038/s41467-020-17289-z.
Kim, H.C., Bishnoi, P.R., Heidemann, R.A., Rizvi, S.S.H., 1987. Kinetics of methane hydrate decomposition. Chem. Eng. Sci. 42 (7), 1645–1653. http://dx.doi.org/10.1016/0009-2509(87)80169-0.
Kimoto, S., Oka, F., Fushita, T., Fujiwaki, M., 2007. A chemo-thermo-mechanically coupled numerical simulation of the subsurface ground deformations due to methane hydrate dissociation. Comput. Geotech. 34 (4), 216–228. http://dx.doi.org/10.1016/j.compgeo.2007.02.006.
Klar, A., Soga, K., Ng, M., 2010. Coupled deformation–flow analysis for methane hydrate extraction. Géotechnique 60 (10), 765–776. http://dx.doi.org/10.1680/geot.9.P.079-3799.
Klar, A., Uchida, S., Soga, K., Yamamoto, K., 2013. Explicitly coupled thermal flow mechanical formulation for gas-hydrate sediments. Spe J. 18 (02), 196–206.
Konno, Y., Masuda, Y., Hariguchi, Y., Kurihara, M., Ouchi, H., 2010. Key factors for depressurization-induced gas production from oceanic methane hydrates. Energy Fuels 24 (3), 1736–1744. http://dx.doi.org/10.1021/ef901115h.
Laberg, J., Camerlenghi, A., 2008. The significance of contourites for submarine slope stability. Dev. Sedimentol. 60, 537–556.
Lei, X., He, S., Abed, A., Chen, X., Yang, Z., Wu, Y., 2021. A generalized interpolation material point method for modelling coupled thermo-hydro-mechanical problems. Comput. Methods Appl. Mech. Engrg. 386, 114080. http://dx.doi.org/10.1016/j.cma.2021.114080.
Lei, X., He, S., Chen, X., Wong, H., Wu, L., Liu, E., 2020. A generalized interpolation material point method for modelling coupled seepage-erosion-deformation process within unsaturated soils. Adv. Water Resour. 141, 103578. http://dx.doi.org/10.1016/j.advwatres.2020.103578.
Lei, X., He, S., Chen, X., Yang, Z., Dong, Y., Wang, L., 2024. MPM simulation of frictional heating–Induced hypermobility of landslides. Landslides http://dx.doi.org/10.1007/s10346-024-02269-x.
Lei, H., Xu, T., Jin, G., 2015. TOUGH2Biot – A simulator for coupled thermal–hydrodynamic–mechanical processes in subsurface flow systems: Application to CO2 geological storage and geothermal development. Comput. Geosci. 77, 8–19. http://dx.doi.org/10.1016/j.cageo.2015.01.003.
Lewis, R.W., Schrefler, B.A., 1998. The Finite Element Method in the Static and Dynamic Deformation and Consolidation of Porous Media, John Wiley & Sons.
Li, H., Lai, Y., Wang, L., Yang, X., Jiang, N., Li, L., Wang, C., Yang, B., 2019. Review of the state of the art: Interactions between a buried pipeline and frozen soil. Cold Reg. Sci. & Technol. 157, 171–186. http://dx.doi.org/10.1016/j.coldregions.2018.10.014.
Li, X., Zhao, J., Soga, K., 2021. A new physically based impact model for debris flow. Géotechnique 71 (8), 674–685. http://dx.doi.org/10.1680/jgeot.18.P.365.
Lian, Y., Bui, H.H., Nguyen, G.D., Haque, A., 2023. An effective and stabilised (U-pl) SPH framework for large deformation and failure analysis of saturated porous media. Comput. Methods Appl. Mech. Engrg. 408, 115967. http://dx.doi.org/10.1016/j.cma.2023.115967.
Liang, H., Song, Y., Chen, Y., 2010. Numerical simulation for laboratory-scale methane hydrate dissociation by depressurization. Energy Convers. Manage. 51 (10), 1883–1890. http://dx.doi.org/10.1016/j.enconman.2010.02.018.
Liang, W., Zhao, J., 2019. Multiscale modeling of large deformation in geomechanics. Int. J. Numer. Anal. Methods Geomech. 43 (5), 1080–1114. http://dx.doi.org/10.1002/nag.2921.
Liang, W., Zhao, J., Wu, H., Soga, K., 2023. Multiscale, multiphysics modeling of saturated granular materials in large deformation. Comput. Methods Appl. Mech. Engrg. 405, 115871. http://dx.doi.org/10.1016/j.cma.2022.115871.
Mahabadi, N., Zheng, X., Jang, J., 2016. The effect of hydrate saturation on water retention curves in hydrate-bearing sediments. Geophys. Res. Lett. 43 (9), 4279–4287.
Makogon, I.F.I.F., 1997. Hydrates of natural gas. (No Title).
Makogon, Y.F., 2010. Natural gas hydrates – A promising source of energy. J. Nat. Gas Sci. Eng. 2 (1), 49–59. http://dx.doi.org/10.1016/j.jngse.2009.12.004.
Mast, C.M., Arduino, P., Mackenzie-Helnwein, P., Miller, G.R., 2015. Simulating granular column collapse using the material point method. Acta Geotech. 10 (1), 101–116. http://dx.doi.org/10.1007/s11440-014-0309-0.
Masuda, Y., 1999. Modeling and experimental studies on dissociation of methane gas hydrates in berea sandstone cores. In: Proceedings of the Third International Gas Hydrate Conference.
Menetrey, P., Willam, K.J., 1995. Triaxial failure criterion for concrete and its generalization. Struct. J. 92 (3), 311–318. http://dx.doi.org/10.14359/1132.
Mestdagh, T., Poort, J., De Batist, M., 2017. The sensitivity of gas hydrate reservoirs to climate change: Perspectives from a new combined model for permafrost-related and marine settings. Earth-Sci. Rev. 169, 104–131. http://dx.doi.org/10.1016/j.earscirev.2017.04.013.
Moridis, G.J., 2003. Numerical studies of gas production from methane hydrates. SPE J. 8 (04), 359–370. http://dx.doi.org/10.2118/87330-PA.
Mountjoy, J.J., Pecher, I., Henrys, S., Crutchley, G., Barnes, P.M., Plaza-Faverola, A., 2014. Shallow methane hydrate system controls ongoing, downslope sediment transport in a low-velocity active submarine landslide complex, H ikurangi M argin, N ew Z ealand. Geochem. Geophys. Geosystems 15 (11), 4137–4156.
Na, S., Sun, W., 2017. Computational thermo-hydro-mechanics for multiphase freezing and thawing porous media in the finite deformation range. Comput. Methods Appl. Mech. Engrg. 318, 667–700. http://dx.doi.org/10.1016/j.cma.2017.01.028.
Nairn, J.A., Guilkey, J.E., 2015. Axisymmetric form of the generalized interpolation material point method. Internat. J. Numer. Methods Engrg. 101 (2), 127–147. http://dx.doi.org/10.1002/nme.4792.
Nazridoust, K., Ahmadi, G., 2007. Computational modeling of methane hydrate dissociation in a sandstone core. Chem. Eng. Sci. 62 (22), 6155–6177. http://dx.doi.org/10.1016/j.ces.2007.06.038.
Oda, M., Kazama, H., 1998. Microstructure of shear bands and its relation to the mechanisms of dilatancy and failure of dense granular soils. Geotechnique 48 (4), 465–481.

Oka, F., Kodaka, T., Kimoto, S., Kim, Y.S., Yamasaki, N., 2006. A multi-phase coupled FE analysis using an elasto-viscoplastic model for unsaturated soil. In: Geomechanics II: Testing, Modeling, and Simulation. pp. 124–131.

Pinyol, N.M., Alvarado, M., Alonso, E.E., Zabala, F., 2018. Thermal effects in landslide mobility. Géotechnique 68 (6), 528–545. http://dx.doi.org/10.1680/jgeot.17.P.054.

Puzrin, A.M., Germanovich, L., Kim, S., 2004. Catastrophic failure of submerged slopes in normally consolidated sediments. Géotechnique 54 (10), 631–643.

Queiruga, A.F., Moridis, G.J., Reagan, M.T., 2019. Simulation of gas production from multilayered hydrate-bearing media with fully coupled flow, thermal, chemical and geomechanical processes using TOUGH+Millstone. Part 2: Geomechanical formulation and numerical coupling. Transp. Porous Media 128 (1), 221–241. http://dx.doi.org/10.1007/s11242-019-01242-w.

Reagan, M.T., Moridis, G.J., 2007. Oceanic gas hydrate instability and dissociation under climate change scenarios. Geophys. Res. Lett. 34 (22), http://dx.doi.org/10.1029/2007GL031671.

Rosakis, P., Rosakis, A., Ravichandran, G., Hodowany, J., 2000. A thermodynamic internal variable model for the partition of plastic work into heat and stored energy in metals. J. Mech. Phys. Solids 48 (3), 581–607.

Roscoe, K.H., 1970. The influence of strains in soil mechanics. Geotechnique 20 (2), 129–170.

Ruan, X., Song, Y., Liang, H., Yang, M., Dou, B., 2012. Numerical simulation of the gas production behavior of hydrate dissociation by depressurization in hydrate-bearing porous medium. Energy Fuels 26 (3), 1681–1694. http://dx.doi.org/10.1021/ef201299p.

Ruppel, C.D., Kessler, J.D., 2017. The interaction of climate change and methane hydrates. Rev. Geophys. 55 (1), 126–168. http://dx.doi.org/10.1002/2016RG000534.

Sang, Q.-y., Xiong, Y.-l., Zheng, R.-y., Bao, X.-h., Ye, G.-l., Zhang, F., 2024. An implicit coupled MPM formulation for static and dynamic simulation of saturated soils based on a hybrid method. Comput. Mech. 1–28.

Santamarina, J.C., Ruppel, C., 2010. The impact of hydrate saturation on the mechanical, electrical, and thermal properties of hydrate-bearing sand, silts, and clay. In: Geophysical Characterization of Gas Hydrates. Society of Exploration Geophysicists, pp. 373–384.

Siron, M., Trottet, B., Gaume, J., 2023. A theoretical framework for dynamic anticrack and supershear propagation in snow slab avalanches. J. Mech. Phys. Solids 181, 105428.

Sloan, S.W., 1987. Substepping schemes for the numerical integration of elastoplastic stress-strain relations. Internat. J. Numer. Methods Engrg. 24 (5), 893–911. http://dx.doi.org/10.1002/nme.1620240505.

Sloan, Jr., E.D., Koh, C.A., 2007. Clathrate Hydrates of Natural Gases, CRC Press.

Soga, K., Alonso, E., Yerro, A., Kumar, K., Bandara, S., 2016. Trends in large-deformation analysis of landslide mass movements with particular emphasis on the material point method. Géotechnique 66 (3), 248–273. http://dx.doi.org/10.1680/jgeot.15.LM.005.

Soga, K., Lee, S., Ng, M., Klar, A., 2006. Characterisation and engineering properties of methane hydrate soils. Characterisation Eng. Prop. Nat. Soils 4, 2591–2642.

Sridhara, P., Anderson, B.J., Garapati, N., Seol, Y., Myshakin, E.M., 2018. Novel technological approach to enhance methane recovery from class 2 hydrate deposits by employing CO2 injection. Energy Fuels 32 (3), 2949–2961. http://dx.doi.org/10.1021/acs.energyfuels.7b03441.

Stomakhin, A., Schroeder, C., Chai, L., Teran, J., Selle, A., 2013. A material point method for snow simulation. ACM Trans. Graph. 32 (4), 1. http://dx.doi.org/10.1145/2461912.2461948.

Stomakhin, A., Schroeder, C., Jiang, C., Chai, L., Teran, J., Selle, A., 2014. Augmented MPM for phase-change and varied materials. ACM Trans. Graph. 33, 1–11.

Sulsky, D., Chen, Z., Schreyer, H.L., 1994. A particle method for history-dependent materials. Comput. Methods Appl. Mech. Engrg. 118 (1), 179–196. http://dx.doi.org/10.1016/0045-7825(94)90112-0.

Sulsky, D., Schreyer, H.L., 1996. Axisymmetric form of the material point method with applications to upsetting and Taylor impact problems. Comput. Methods Appl. Mech. Engrg. 139 (1–4), 409–429. http://dx.doi.org/10.1016/S0045-7825(96)01091-2.

Sulsky, D., Zhou, S.-J., Schreyer, H.L., 1995. Application of a particle-in-cell method to solid mechanics. Comput. Phys. Comm. 87 (1–2), 236–252.

Sultan, N., Cochonat, P., Foucher, J.P., Mienert, J., 2004. Effect of gas hydrates melting on seafloor slope instability. Mar. Geol. 213 (1), 379–401. http://dx.doi.org/10.1016/j.margeo.2004.10.015.

Sun, W., 2015. A stabilized finite element formulation for monolithic thermo-hydro-mechanical simulations at finite strain. Internat. J. Numer. Methods Engrg. 103 (11), 798–839. http://dx.doi.org/10.1002/nme.4910.

Sun, X., Luo, H., Soga, K., 2018. A coupled thermal–hydraulic–mechanical–chemical (THMC) model for methane hydrate bearing sediments using COMSOL Multiphysics. J. Zhejiang Univ.-Sci. A 19 (8), 600–623. http://dx.doi.org/10.1631/jzus.A1700464.

Sun, X., Mohanty, K.K., 2006. Kinetic simulation of methane hydrate formation and dissociation in porous media. Chem. Eng. Sci. 61 (11), 3476–3495. http://dx.doi.org/10.1016/j.ces.2005.12.017.

Sun, H., Xiong, F., Wu, Z., Ji, J., Fan, L., 2022. An extended numerical manifold method for two-phase seepage–stress coupling process modelling in fractured porous medium. Comput. Methods Appl. Mech. Engrg. 391, 114514. http://dx.doi.org/10.1016/j.cma.2021.114514.

Taylor, G.I., Quinney, H., 1931. The plastic distortion of metals. Philos. Trans. R. Soc. Lond. Ser. A, Contain. Pap. A Math. Or Phys. Character 230 (681–693), 323–362.

Uchida, S., Soga, K., Yamamoto, K., 2012. Critical state soil constitutive model for methane hydrate soil. J. Geophys. Res.: Solid Earth 117 (B3).

Van Genuchten, M.T., 1980. A closed-form equation for predicting the hydraulic conductivity of unsaturated soils. Soil Sci. Am. J. 44 (5), 892–898. http://dx.doi.org/10.2136/sssaj1980.03615995004400050002x.

Vardoulakis, I., 1980. Shear band inclination and shear modulus of sand in biaxial tests. Int. J. Numer. Anal. Methods Geomech. 4 (2), 103–119.

Vermeer, P., 1990. The orientation of shear bands in biaxial tests. Géotechnique 40 (2), 223–236.

Veveakis, E., Vardoulakis, I., Di Toro, G., 2007. Thermoporomechanics of creeping landslides: The 1963 Vaiont slide, northern Italy. J. Geophys. Res.: Earth Surf. 112 (F3).

Waite, W.F., Santamarina, J.C., Cortes, D.D., Dugan, B., Espinoza, D.N., Germaine, J., Jang, J., Jung, J.W., Kneafsey, T.J., Shin, H., Soga, K., Winters, W.J., Yun, T.-S., 2009. Physical properties of hydrate-bearing sediments. Rev. Geophys. 47 (4), http://dx.doi.org/10.1029/2008RG000279.

Wan, L., Yu, X., Steve, T., Li, S., Kuang, Z., Sha, Z., Liang, J., He, Y., 2016. Submarine landslides, relationship with BSRs in the Dongsha area of South China sea. Pet. Res. 1 (1), 59–69.

Wang, H., Chen, Y., Zhou, B., Xue, S., 2021. Investigation of the effect of cementing ratio on the mechanical properties and strain location of hydrate-bearing sediments by using DEM. J. Nat. Gas Sci. Eng. 94, 104123.

White, M.D., Kneafsey, T.J., Seol, Y., Waite, W.F., Uchida, S., Lin, J.S., Myshakin, E.M., Gai, X., Gupta, S., Reagan, M.T., Queiruga, A.F., Kimoto, S., Baker, R.C., Boswell, R., Ciferno, J., Collett, T., Choi, J., Dai, S., De La Fuente, M., Fu, P., Fujii, T., Intihar, C.G., Jang, J., Ju, X., Kang, J., Kim, J.H., Kim, J.T., Kim, S.J., Koh, C., Konno, Y., Kumagai, K., Lee, J.Y., Lee, W.S., Lei, L., Liu, F., Luo, H., Moridis, G.J., Morris, J., Nole, M., Otsuki, S., Sanchez, M., Shang, S., Shin, C., Shin, H.S., Soga, K., Sun, X., Suzuki, S., Tenma, N., Xu, T., Yamamoto, K., Yoneda, J., Yonkofski, C.M., Yoon, H.C., You, K., Yuan, Y., Zerpa, L., Zyrianova, M., 2020. An international code comparison study on coupled thermal, hydrologic and geomechanical processes of natural gas hydrate-bearing sediments. Mar. Pet. Geol. 120, 104566. http://dx.doi.org/10.1016/j.marpetgeo.2020.104566.

Wu, P., Li, Y., Liu, W., Sun, X., Kong, X., Song, Y., 2020. Cementation failure behavior of consolidated gas hydrate-bearing sand. J. Geophys. Res.: Solid Earth 125 (1), e2019JB018623.

Wu, X.-H., Zhang, Q., Feng, W.-Q., Yin, Z.-Y., Fang, H., 2025. Enhanced THM coupling for anisotropic geomaterials and smoothed-FEM simulation. Int. J. Mech. Sci. 290, 110087.

Xie, Y., Qu, T., Yang, J., Wang, S., Zhao, J., 2025. Multiscale insights into tunneling-induced ground responses in coarse-grained soils. Comput. Geotech. 185, 107319.

Xu, W., Germanovich, L.N., 2006. Excess pore pressure resulting from methane hydrate dissociation in marine sediments: A theoretical approach. J. Geophys. Res.: Solid Earth 111 (B1), http://dx.doi.org/10.1029/2004JB003600.

Yan, R., Yu, H., Yang, D., Tang, H., Zhang, Q., 2023. Shear strength and pore pressure characteristics of methane hydrate-bearing soil under undrained condition. Int. J. Hydrog. Energy 48 (33), 12240–12256.

Yang, H., Sinha, S.K., Feng, Y., McCallen, D.B., Jeremić, B., 2018. Energy dissipation analysis of elastic–plastic materials. Comput. Methods Appl. Mech. Engrg. 331, 309–326. http://dx.doi.org/10.1016/j.cma.2017.11.009.

Ye, Z., Wang, L., Zhu, B., Shao, H., Xu, W., Chen, Y., 2022. A thermo-hydro-chemo-mechanical coupled model for natural gas hydrate-bearing sediments considering gravity effect. J. Nat. Gas Sci. Eng. 108, 104823. http://dx.doi.org/10.1016/j.jngse.2022.104823.

Yerro, A., Alonso, E., Pinyol, N., 2015. The material point method for unsaturated soils. Géotechnique 65 (3), 201–217. http://dx.doi.org/10.1680/geot.14.P.163.

Yin, Z., Linga, P., 2019. Methane hydrates: A future clean energy resource. Chin. J. Chem. Eng. 27 (9), 2026–2036. http://dx.doi.org/10.1016/j.cjche.2019.01.005.

Yu, J., Weijian, L., Zhao, J., 2024a. Enhancing dynamic modeling of porous media with compressible fluid: A THM material point method with improved fractional step formulation. Comput. Methods Appl. Mech. Engrg. 444, http://dx.doi.org/10.1016/j.cma.2025.118100.

Yu, T., Zhao, J., 2021. Semi-coupled resolved CFD–DEM simulation of powder-based selective laser melting for additive manufacturing. Comput. Methods Appl. Mech. Engrg. 377, 113707. http://dx.doi.org/10.1016/j.cma.2021.113707.

Yu, J., Zhao, J., Liang, W., Zhao, S., 2024b. Multiscale modeling of coupled thermo-hydro-mechanical behavior in ice-bonded granular media subject to freeze-thaw cycles. Comput. Geotech. 171, 106349. http://dx.doi.org/10.1016/j.compgeo.2024.106349.

Yu, J., Zhao, J., Liang, W., Zhao, S., 2024c. A semi-implicit material point method for coupled thermo-hydro-mechanical simulation of saturated porous media in large deformation. Comput. Methods Appl. Mech. Engrg. 418, 116462. http://dx.doi.org/10.1016/j.cma.2023.116462.

Yu, J., Zhao, J., Zhao, S., Liang, W., 2024d. Multiphysics simulation of freezing and thawing granular media using material point method. IOP Conf. Ser.: Earth Environ. Sci. 1330 (1), 012035. http://dx.doi.org/10.1088/1755-1315/1330/1/012035.

Yu, J., Zhao, J., Zhao, S., Liang, W., 2024e. Thermo-hydro-mechanical coupled material point method for modeling freezing and thawing of porous media. Int. J. Numer. Anal. Methods Geomech. 48 (13), 3308–3349. http://dx.doi.org/10.1002/nag.3794.

Zhan, Z.Q., Zhou, C., Liu, C.Q., Du, J.T., 2024. MPM formulations for the coupled thermo-hydro-mechanical behaviour of saturated and unsaturated soils. Comput. Geotech. 170, 106313. http://dx.doi.org/10.1016/j.compgeo.2024.106313.

Zhang, G., Liu, E., Zhang, G., Chen, Y., 2021. Study thermo-hydro-mechanical coupling behaviors of saturated frozen soil based on granular solid hydrodynamics theory. Arch. Appl. Mech. 91 (9), 3921–3936. http://dx.doi.org/10.1007/s00419-021-01987-1.

Zhang, L., Wu, B., Li, Q., Hao, Q., Zhang, H., Nie, Y., 2024. A fully coupled thermal–hydro–mechanical–chemical model for simulating gas hydrate dissociation. Appl. Math. Model. 129, 88–111.

Zhao, J., Fan, Z., Dong, H., Yang, Z., Song, Y., 2016. Influence of reservoir permeability on methane hydrate dissociation by depressurization. Int. J. Heat Mass Transfer 103, 265–276. http://dx.doi.org/10.1016/j.ijheatmasstransfer.2016.05.111.

Zhao, J.-F., Ye, C.-C., Song, Y.-C., Liu, W.-G., Cheng, C.-X., Liu, Y., Zhang, Y., Wang, D.-Y., Ruan, X.-k., 2012. Numerical simulation and analysis of water phase effect on methane hydrate dissociation by depressurization. Ind. Eng. Chem. Res. 51 (7), 3108–3118. http://dx.doi.org/10.1021/ie202035n.

Zhao, J., Zhang, P., Yang, X., Qi, J., 2020. On the uniaxial compression strength of frozen gravelly soils. Cold Reg. Sci. & Technol. 171, 102965. http://dx.doi.org/10.1016/j.coldregions.2019.102965.

Zheng, B., Li, T., Qi, H., Gao, L., Liu, X., Yuan, L., 2023. Multiphysics meshless method for mesoscopic concrete cracking under frost action. Constr. Build. Mater. 397, 132209. http://dx.doi.org/10.1016/j.conbuildmat.2023.132209.